5.0 CIRCULATION AND SEDIMENT TRANSPORT DYNAMICS

This section analyzes the physical regime of the Alabama continental shelf and discusses circulation, wave, and sediment transport processes to evaluate the potential environmental impact of offshore sand mining. Current and wave processes provide physical mechanisms for moving sediment throughout the Alabama coastal zone. The following discussion documents the physical mechanisms potentially impacted by sand mining within specific offshore locations.

5.1 CURRENTS AND CIRCULATION

Circulation patterns observed at specific areas within the study region were evaluated within the context of potential offshore sand mining operations. The following discussion uses long-term current measurements obtained during previous studies in the region, as well as current meter data collected during field surveys for this program, to describe circulation at the study site. Long-term observations were analyzed to provide an understanding of temporal variations of inner shelf circulation (time scales of hours to months), while field survey data sets provided detail regarding to spatial variability within specific borrow sites. Combined, the analyses presented in this section describe circulation characteristics within the study region, including major forcing influences, time scales of variability, and the magnitude of resulting currents. The results from this section were used to provide estimates of sediment transport potential at potential offshore borrow sites.

5.1.1 Historical Data Analysis

Long-term observations of currents, previously collected by various investigators on the Alabama/Florida inner-continental shelf, were obtained and analyzed for this study. These data were used to estimate the major forcing influences throughout the region and to determine the seasonal variability of the flow regime. The goal of the analyses was to develop an understanding of current patterns throughout the study region, and to use this information to determine how sediment transport at potential sand resource sites may be affected by the flow regime on the inner shelf.

Two current meter data sources were used for evaluating seasonal and annual variations in flow throughout the study area. These data represent current observations at specific mooring locations along the Alabama inner shelf (Table 5-1). Supporting data, such as observations of atmospheric winds, were included in the analysis as well. Unfortunately, observations of density stratification on the shelf or freshwater discharge from Mobile Bay, two important parameters identified from previous investigations which influence circulation in the region, were unavailable for this analysis.

Continental Shelf Associates (CSA), Inc., of Jupiter, FL, provided current meter observations at Sand Resource Area 4, specifically near Shell Oil Platform #132, during the time period September 28, 1987 to October 24, 1988 (Hart et al., 1989). The mooring was deployed west of the main ship channel and due east of the dredged material disposal mound. Observations represent a year-long record of near-bottom currents (approximately 1.6 m above the seafloor in approximately 12-m water depth). These data were used to develop an understanding of the most-frequent flow characteristics near Sand Resource Area 4.

The second data set resulted from an Environmental Protection Agency (EPA) study offshore of Gulf Shores, AL (Dinnell, 1997). A series of five moorings were deployed in areas within Sand Resource Areas 1 and 2 (Figure 5-1). Data were collected between late March 1986 and late March 1987. Data coverage at any single mooring site was sporadic during this time. A nearshore site, named Gulf Shores Current Meter Mooring 1 (GSCM1), had observations collected in approximately 5-m water depth with a single meter located approximately at mid-depth (GSCM1M) within Sand Resource Area 1. These data were almost complete for the period April 1986 to March 1987. A

second location (GSCM4) is within Sand Resource Area 2 in approximately 10-m water depth and yielded observations at near-bottom (GSCM4B) and near-surface depths (GSCM4S). Data were collected at both depths during the period early May 1986 to mid-November 1986. These three data sets formed the basis for developing an understanding of flow field characteristics for Sand Resource Areas 1, 2, and 3.

| Table 5-1. Current meter data sets collected in the study area.			
Data Set Name	Location	Water depth (sensor depth)	Dates
Shell Block 132	Resource Area 4 30° 09.6N 88° 4.8W	12.0 m (10.6 m)	28-Sep-87 to 24-Oct-88
GSCM1M	Resource Area 1 30° 13.8N 87° 41.1W	5.0 m (2.5 m)	29-Mar-86 to 04-Mar-87
GSCM4B	Resource Area 2 30° 11.3N 87° 44.4W	10.0 m (2.0 m)	11-May-86 to 25-Nov-86
GSCM4S	Resource Area 2 30° 11.3N 87° 44.4W	10.0 m (8.0 m)	24-Apr-86 to 23-Nov-86
Sources: Continental Shelf Associates (Hart et al., 1989); Dinnell, 1997			
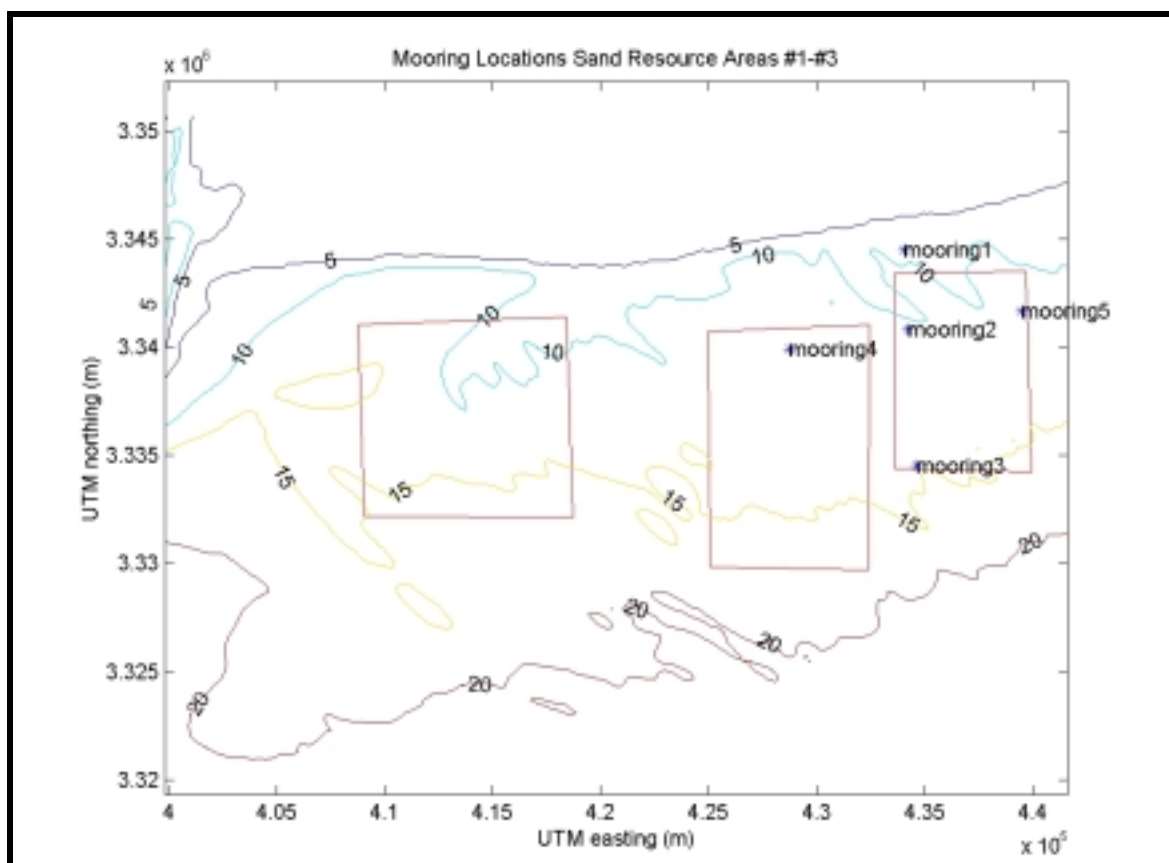
Figure 5-1. Map of sand resource areas east of Mobile Bay; Sand Resource Area 1 (far east) and Sand Resource Area 3 (far west). The five Gulf Shores mooring locations are shown as asterisks (*). Contours are labeled in m.

5.1.1.1 Decomposition of Total Currents

Currents observed at each mooring site during the deployments represent the cumulative effects of many physical processes active in this region; processes which have a variety of time scales and amplitudes. These processes occur simultaneously; hence, the current observed at any one time can be considered a superposition of all individual processes. This section describes the numerical procedures used to separate the observed currents into individual subsets, each with specific time scales of variability. This procedure allows analysis of each process to determine their relative importance to total circulation in the region.

Separation of the total signal into specific process components was performed using various numerical analysis techniques, such as tidal harmonic decomposition, as well as the application of a series of low-, band-, and high-pass filters. The results of the analyses represent subsets of individual time series. Each time subset represents a specific physical process, such as:

- high-frequency currents (less than approximately 33-hour periodicity)
- tidal currents (diurnal, semi-diurnal, fortnightly)
- wind-driven currents (1 to 15 day frequency band)
- low frequency or seasonal currents (greater than 15 day periodicity).

The first step in the separation analysis is to remove tidal currents from the raw data using harmonic analysis. Harmonic analysis calculates the amplitude and phase of 23 individual tidal constituents using a least-squares fit of the constituent sinusoid to the raw data signal. The tidal constituents removed included K1, M2, M4, M6, S2, N2, O1, S4, S6, M8, MK3, MN4, MS4, 2N2, OO1, M1, J1, Q1, 2Q1, L2, 2SM2, Mf, and MSF. A majority of these constituents represent high frequency tides, or tides having periods less than approximately 28 hours (diurnal tides). The exception is the MSf and Mf tides, which vary on an approximate 14.7-day and 13.6-day period, respectively.

The result of this analysis is a separation of the total observed currents into two time series; one is predicted tides, based on a reconstruction of individual tidal components, and the second is non-tidal or residual currents. The residual current was generated by subtracting (point by point) the reconstructed tidal series from the original signal.

The residual signal became the basis for subsequent analyses. The first step in processing was to remove the remaining high frequency energy. This was accomplished by applying a PL33 low-pass filter over the residual signal. The PL33 is a standard oceanographic filter which uses 1/(33 hours) as the cutoff frequency, and is used primarily to remove tidal energy (or all signal energy with periodicity less than 33 hours) from oceanographic time series. Some energy leakage can occur near the cutoff frequency using this filtering method; however, this effect is minimal since the significant diurnal (and higher frequency) tides had been removed prior to this step. The low-passed time series was termed the subtidal signal.

The subtidal signal was subtracted from the previous residual signal, resulting in a high frequency time series containing all non-tidal currents having periods less than approximately 33 hours. This high-frequency signal (typically referred to as noise) contained significant energy, which can be due to several sources, including actual flow field turbulence, wave-induced flow, as well as possible data contamination due to mooring motions. The high frequency signal was saved as a separate time series for later analysis and comparison.

The subtidal signal was then reduced further into distinct frequency bands. The first frequency band was defined as processes with time scales of 1-15 days.   It was assumed to include wind-driven flows, as well as other processes of similar time scales. Buoyancy-driven flow may be included in this frequency band. This wind-driven band was expected to yield significant energy.

The signal was derived by high-pass filtering the subtidal signal with a 15-day cutoff, and was termed the wind-driven signal.

The second time band defined processes with periodicity greater than 15 days. It was termed the seasonal band, although processes with higher frequencies than seasonal (e.g., 15 to 30 days) are inherently included in this band. This series was derived by subtracting the wind-driven signal from the subtidal signal.

Each time series was extracted in sequential manner from the raw signal to a set of individual process-specific signals, each representing the dominant current occurring at specific time scales. This separation procedure was repeated for every data set.

An example of this analysis with the resulting time series signals is shown in Figure 5-2. Figure 5-2 depicts the time series decomposition of the east component of near-bottom velocity measured at Shell Block 132 (eastern side of Mobile Bay entrance channel) from 1987 to 1988. The top plot is the original signal sampled every 15 minutes. Small data gaps associated with instrument turnarounds had been filled prior to numerical separation using cubic spline interpolation. The subsequent time series represent tidal, high-frequency, wind-driven, and low-frequency (or seasonal) components, respectively. Visually, the high-frequency and wind-driven signals appear to have the most signal variability.

Separating these processes from the whole illustrated the relative contribution of each to the total observed circulation at a selected sand resource site. The signal variance of each resulting time series represents its energy level. Comparing the variance of each process to the total signal variance yields a representation of how much energy the process contributed to the whole. Results are depicted as histograms in Figures 5-3 through 5-6. The original (raw) signal variance was included to show what percentage each individual process contributed to the total signal energy.

Figure 5-3 shows the signal variance for the Shell Block 132 data, collected in an area located to the west of Main Pass at Mobile Bay. The bars to the left of the figure show the total energy of east (light blue) and north (dark purple) velocity components. Total current energy in the east-west direction appears to be equivalent to the north-south current energy. This distribution of energy is consistent with the orientation of local bathymetric contours at the site, and they are aligned along an approximate SE-NW axis. Consistent with results shown in Figure 5-2, the variance of the high-frequency and wind-driven signals contain a majority of the total signal energy. Wind-driven processes dominate the east-west currents with over half (52%) of the total signal energy. North-south flow appears equally distributed between high-frequency and wind-driven processes. Tides and low-frequency processes have little contribution to the overall signal at this location. The tidal signal shows a more dominant north-south component than east-west component of flow. The entrance to Mobile Bay is to the north of the mooring location; hence, a north-south bias of these near-bottom tidal currents would be expected.

Comparing the variance histograms at different locations also illustrates how individual processes vary spatially throughout the region. Figures 5-4 through 5-6 represent the variance histograms for locations to the east of Mobile Bay, near Sand Resource Areas 1 and 2. In these areas, the east-west current is approximately parallel to the shoreline and bathymetric contours, with the north-south component parallel to the cross-shore direction. Mooring 1M is relatively close to shore in shallow water (see Figure 5-1), whereas Mooring 4S and 4B are located in slightly deeper water on the northern fringe of Sand Resource Area 2. Data from 4S represent near-surface observations, whereas data from 4B represent near-bottom flow.

Histogram plots show that the total alongshore component of currents have significantly higher energy than the total cross-shore component, and that energy dissipates close to the seafloor and shoreline boundaries. Alongshore current energy is approximately 40% greater at Mooring 4S location, in deeper-water, than at Mooring 1M, which was located closer to shore.
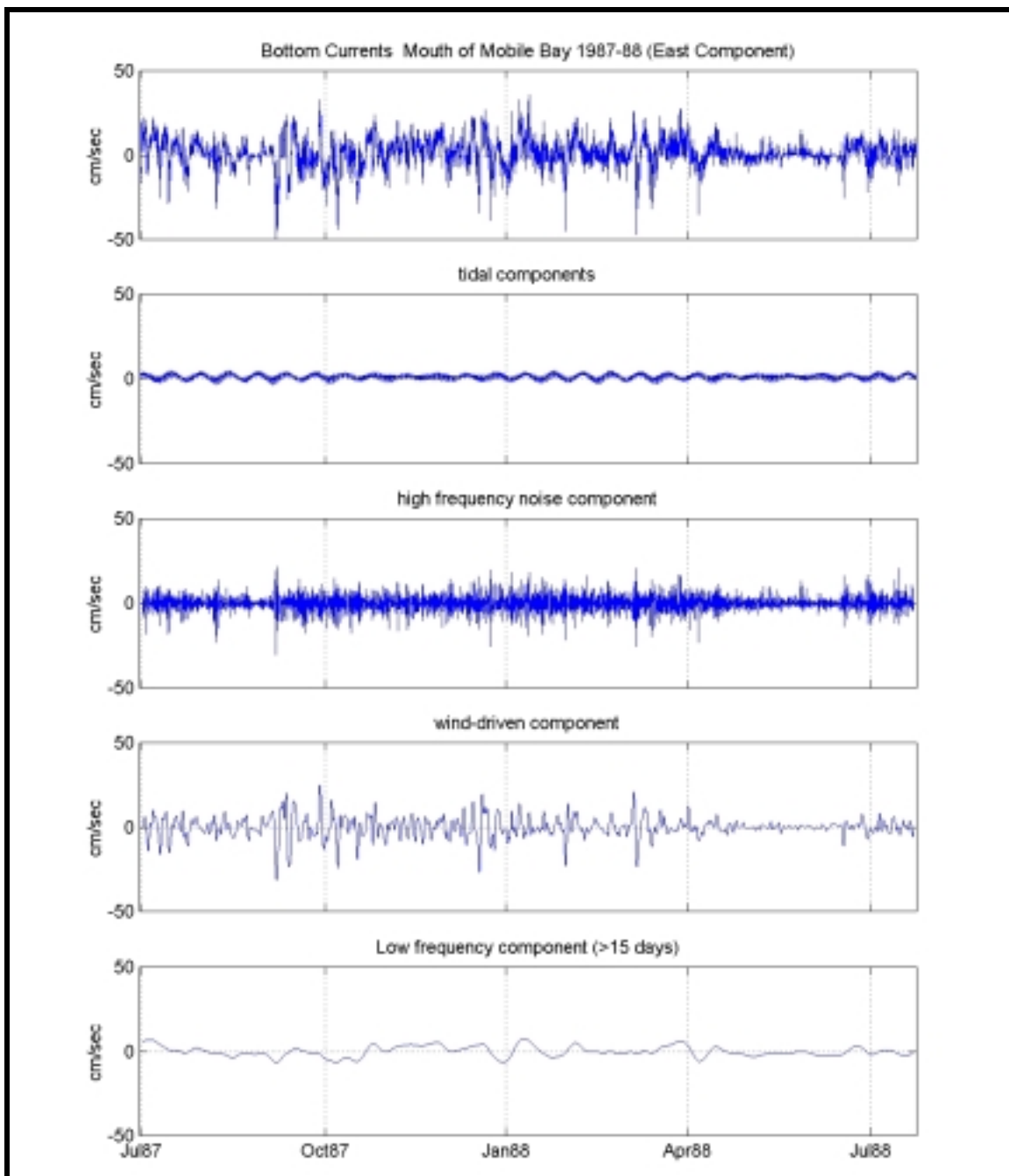
Figure 5-2. An example of the numerical separation of bottom current data collected within Shell Block 132, to the immediate southeast of the entrance to Mobile Bay (from Continental Shelf Associates, Inc. 1989). The data represent the east component of flow.
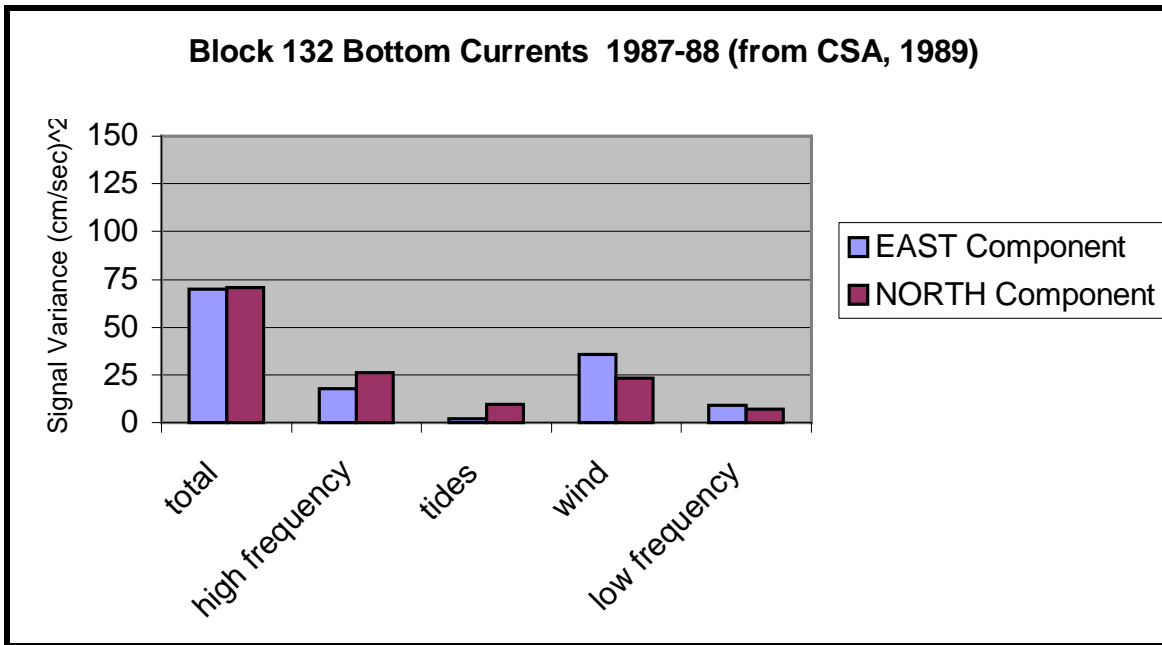
Figure 5-3. Variance histogram for Shell Block 132 Mooring, representing the fraction of total energy attributed to individual forcing mechanisms.
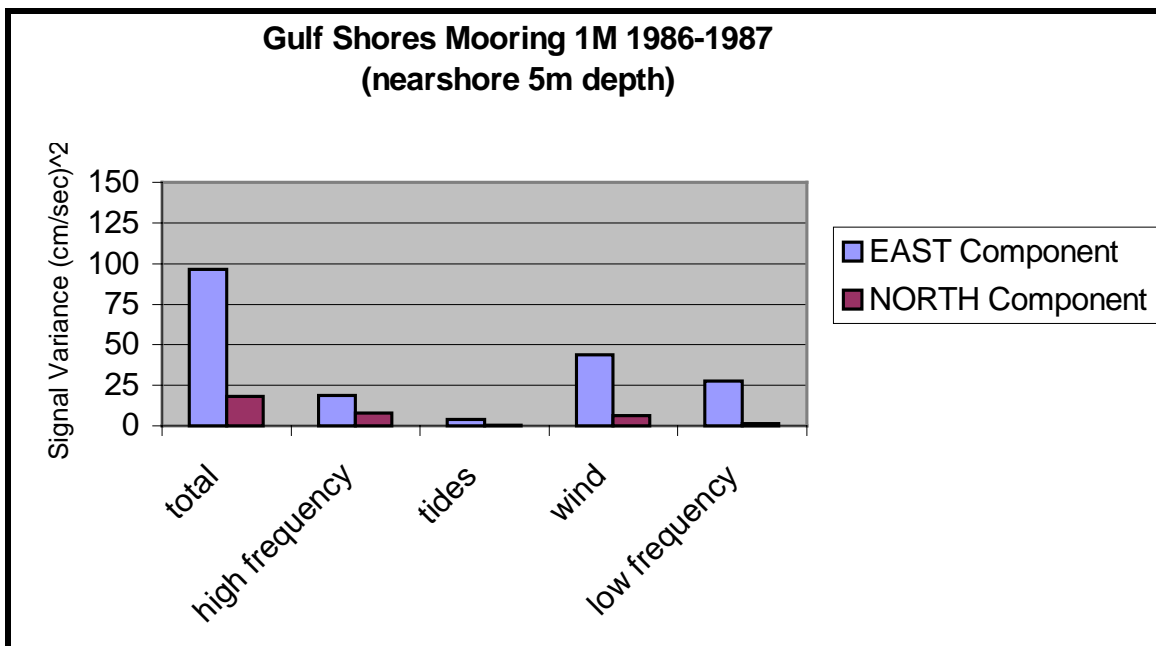

Figure 5-4. Variance histogram for Gulf Shores Mooring 1M, representing the fraction of total energy attributed to individual forcing mechanisms.
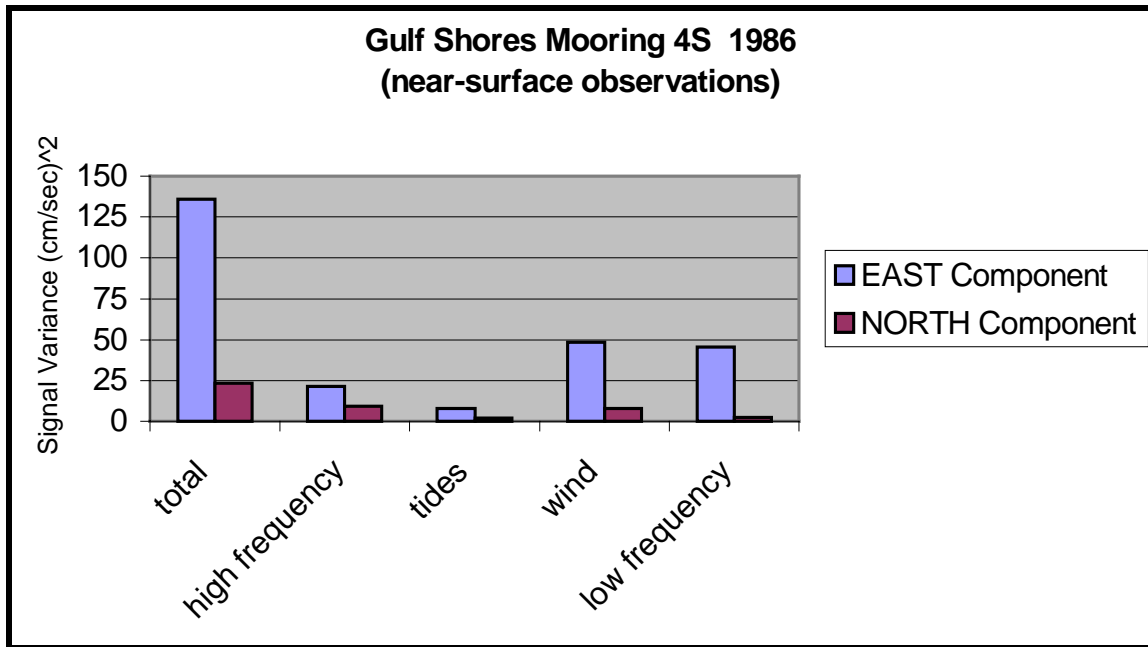
Figure 5-5. Variance histogram for Gulf Shores Mooring 4S, representing the fraction of total energy attributed to the individual forcing mechanisms.
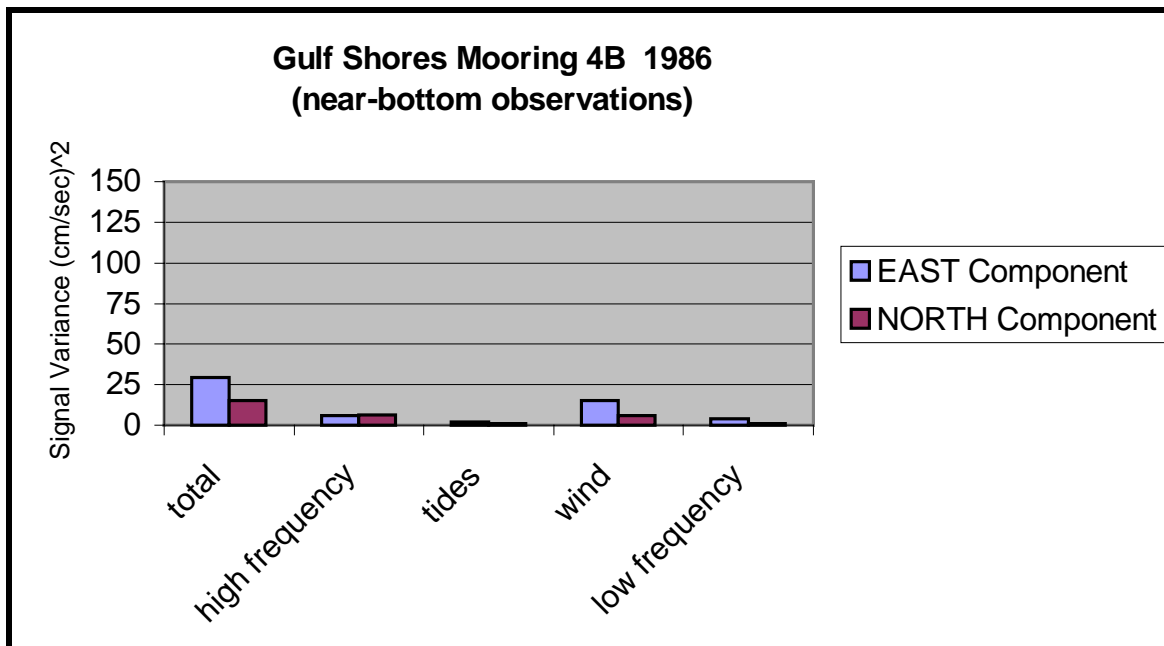

Figure 5-6. Variance histogram for Gulf Shores Mooring 4B, representing the fraction of total energy attributed to the individual forcing mechanisms.

The energy associated with alongshore flow at near-surface 4S was approximately 5 times the energy of the alongshore flow near the seafloor. The attenuation of alongshore current energy near the shoreline and seafloor likely was due to boundary frictional effects. The energy associated with cross-shore currents was similar between the 1M and 4S moorings, with a 50% reduction in cross-shore energy observed at site 4B. Damping of the cross-shore signal should occur in the vertical axis alone, as there is no shoreline boundary to affect flow between site 1M and 4S. The decrease of cross-shore flow at 4B relative to 4S is consistent with frictional damping of the seafloor; a factor of two decrease (versus a factor of five decrease in the alongshore direction) also is consistent with the relatively slower speeds of cross-shore flow versus alongshore flow. Frictional losses are proportional to the square of velocity; at low speeds frictional losses are proportionally smaller than at higher speeds.

5.1.1.2 Current Components

Tidal signals in the eastern part of the study area have a small contribution to the overall current energy, accounting for approximately 3 to 7% of the total observed currents. Of this contribution, alongshore-directed tidal currents were stronger than cross-shore flows. Tidal flow along the sea floor was quite small, with a stronger effect at the surface and near-shore environments.

High-frequency currents, defined as non-tidal variability of frequency less than approximately 33 hours, contribute approximately 16-20% of the total alongshore signal, and approximately 40-45% of the total cross-shore signal. High-frequency currents may stem from several sources: wave-induced flow, high-frequency wind-driven flow where the water column responded rapidly to sudden changes in wind stress, or simply from measurement noise inherent to the current meter. Figure 5-2 shows a high-frequency time series that is well-correlated with the wind-driven time series. As such, the assumption that the high-frequency signal is attributed to wave-induced flow or high-frequency responses to changes in wind stress appears accurate.

Wind-driven flow had the greatest influence on total observed currents at all sites. Approximately 36 to 51% of the total alongshore current was due to winds; in the cross-shore direction, wind-generated flow accounts for approximately 34 to 38% of the signal. Alongshore wind-driven flow was approximately 6 to 7 times stronger than cross-shore wind-driven flow, specifically at sites 4S and 1M. At site 4B, alongshore flow was approximately three times the energy of the cross-shore component. The energy associated with cross-shore wind-driven flow was quite similar between all sites, with little spatial variability.

Low-frequency currents varied considerably with location. These currents may be attributed to many sources, including variations in discharge from Mobile Bay, variations in seasonal wind patterns, and basin-wide fluctuations that may impinge upon the coastline. Low-frequency currents were relatively strong in the alongshore direction relative to the cross-shore direction, and they had greater influence on the site 4S signal (approximately 33% of the total) than at the 4B site (13%) or 1M site (approximately 28%). There appears to be some correlation between these low-frequency signals and the wind-driven signals, suggesting that low-frequency currents may be due to seasonal shifts in prevailing wind patterns.

5.1.1.3 Total Observed Currents

Total observed currents as frequency-of-occurrence rose diagrams illustrate the directional character of flow at each site (Figure 5-7). These rose plots show percent occurrence as a function of earth direction and current speed. Radial (circular) lines define the percent occurrence magnitude, with currents divided into discrete directional bins. The length of the pie slices indicates
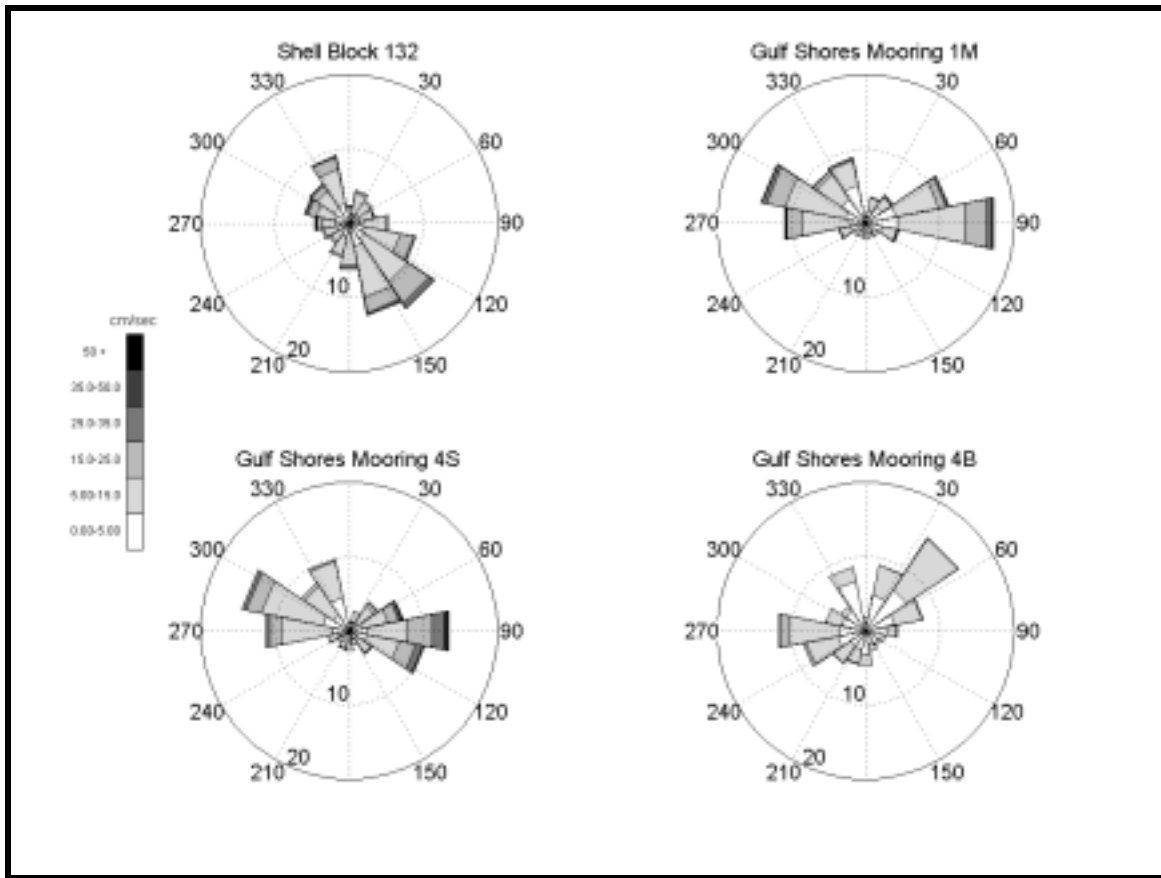
Figure 5-7. Rose diagrams illustrating four historical data sets in the study area. The spokes of the diagram represent compass directions (90=east, 270=west, etc). The circumferential lines represent percent occurrence, with the inner annulus representing 10%, and the outside diameter representing 20% occurrence. A 'pie slice' extending to the outer circumference means that 20% of the time, currents are flowing in that direction. Current speeds are represented by the shading of the pie slice, with white (no shading) portions representing the fraction of time currents are between 0 and 5 cm/sec and black portions indicating the percent occurrence of currents over 50 cm/sec.

percent occurrence; longer slices indicate that currents flow in the specified direction more often than if the pie slice were short. The shading of each pie slice indicates the magnitude of current speed; no shading means the speeds were quite small (between 0 to 5 cm/sec), with increasing intensity as current speeds increase. Portions of the pie slice shaded black infer that speeds were greater than 50 cm/sec. Figure 5-7 shows that currents at all the mooring sites flow predominantly in the alongshore direction with typical speeds of order 5 to 15 cm/sec.

Near-bottom currents west of Mobile Bay entrance, represented by the Shell Bock 132 rose diagram in the upper left corner of Figure 5-7, typically were oriented along a northwest-southeast axis which is parallel to the bathymetry contours at the site. The strongest flow at this site was to the southeast with speeds of order 15 to 25 cm/sec occurring approximately 8 to 10% of the time. Occasional currents with speeds exceeding 25 cm/sec were observed, although these higher speed currents occurred less than 2% of the time.

Currents to the east of Mobile Bay, represented by rose diagrams for Gulf Shores Moorings 1M, 4S, and 4B, were strongest at the surface (Mooring 4S) and weakest at the bottom (Mooring 4B). Flow was stronger offshore (Mooring 4S) than nearer to shore (Mooring 1M), consistent with the variance plots detailed earlier. Currents from these sites also were oriented primarily in the

alongshore direction. The strongest flow was observed at the surface (Mooring 4S), and while surface flow was oriented to the west and northwest most commonly (approximately 33% of the time), this westward flow was typically weaker than flow to the east. Westward flow at Mooring 4S greater than 15 cm/sec occurred approximately 5% of the time, while eastward flow exceeding 15 cm/sec occurred approximately 17% of the time. Approximately 1% of the time, eastward flow exceeded 35 cm/sec, whereas the westward flow never exceeded 35 cm/sec.

The separated signals (tides, high-frequency, wind-driven, and low-frequency currents) were also depicted as rose diagrams to understand the directional distribution for each individual process. Figure 5-8 depicts the frequency of occurrence rose diagrams for each individual process for the Shell Block 132 data set. High- and low-frequency processes illustrate much greater directional variability than either tidal or wind-driven currents. Tidal currents along the bottom at this location appear to flow principally offshore (to the south-southeast) for a majority of the time; the offshore-directed tidal flows were stronger (5 to 15 cm/sec) than the on-shore directed tidal flows (0 to 5 cm/sec). The rose plot of wind-driven flow shows that wind processes dominated total observed currents at the site (compare to Figure 5-7). The dominant wind-driven flows were oriented southeast and northwest, also parallel to the isobaths in the area, which is consistent with the alongshore dominance of currents in the inner shelf region. Near-bottom wind-driven currents were approximately 5 to 15 cm/sec, with occasional currents exceeding 15 cm/sec. Less than 1% of the time, wind-driven currents were oriented to the northwest at speeds exceeding 25 cm/sec.
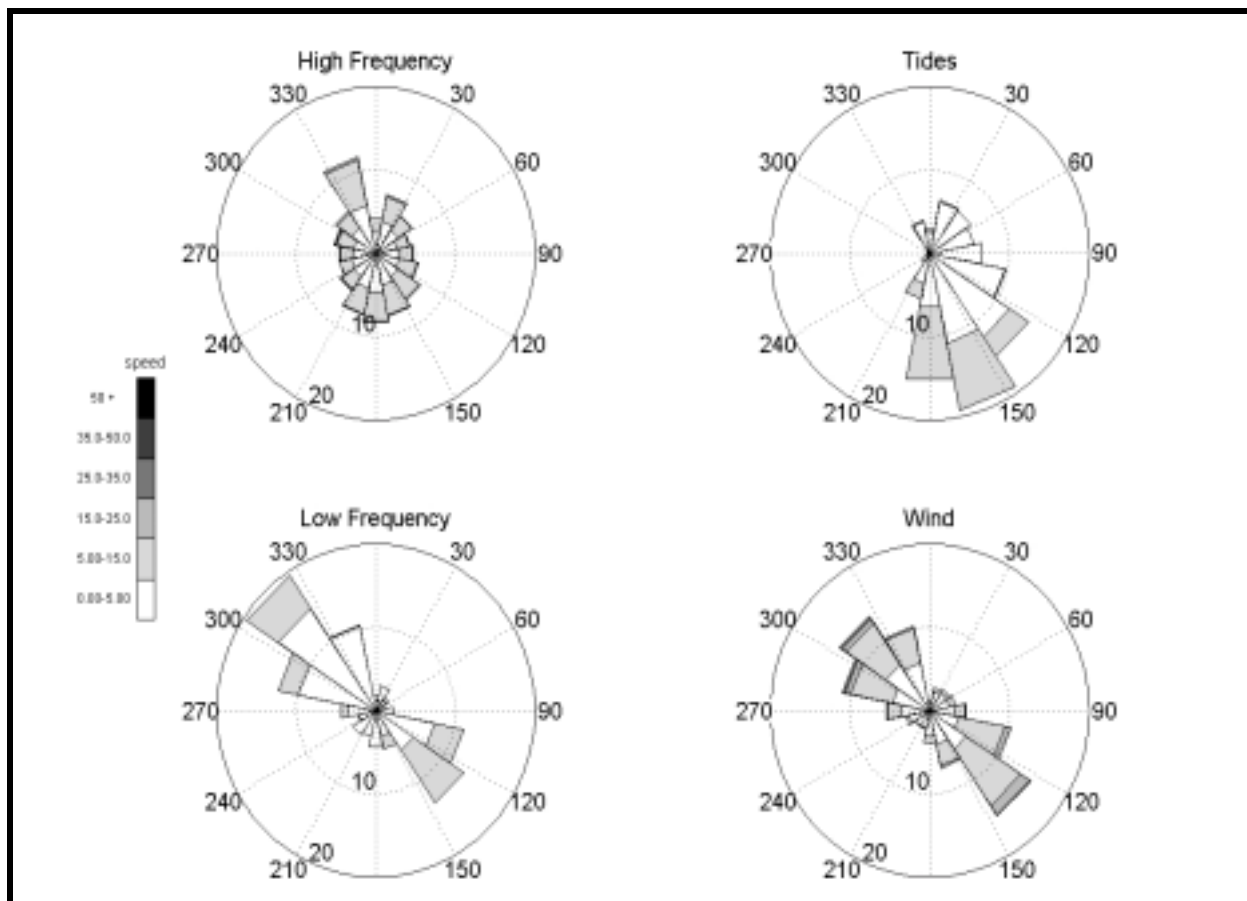

Figure 5-8. Rose diagrams for individual processes at Shell Block 132 (west of Mobile Bay, near-bottom) from September 30, 1987 to October 24, 1988. These data illustrate the relative strength of wind, and that water flow was directed primarily parallel to the isobaths, which are oriented northwest-southeast.

Figure 5-9 shows the rose diagrams for separated signals for Mooring 4S. Figure 5-10 shows the rose diagrams for near-bottom currents collected at Mooring 4B. The high-frequency and low-frequency rose diagrams for both sites indicate these processes are distributed in all directions and do not seem as polarized as wind-driven or tidal currents. Wind-driven currents dominate these sites as well.

The wind-driven signal at Moorings 4S and 4B had an obvious alongshore orientation. Comparison of rose plots for Mooring 4S and 4B show the predominant directional axes are rotated slightly with depth. The predominant direction of flow at 4S was along an approximate east-west axis, whereas the direction of flow at the bottom was an approximate northeast-west turn. The flow appeared to be rotated slightly (perhaps 45 degrees) counterclockwise with increasing depth. This observation at the Mooring 4 location is not consistent with classical Ekman response of the water column to wind forcing, which expects flow to rotate to the right of the wind, or clockwise with depth.
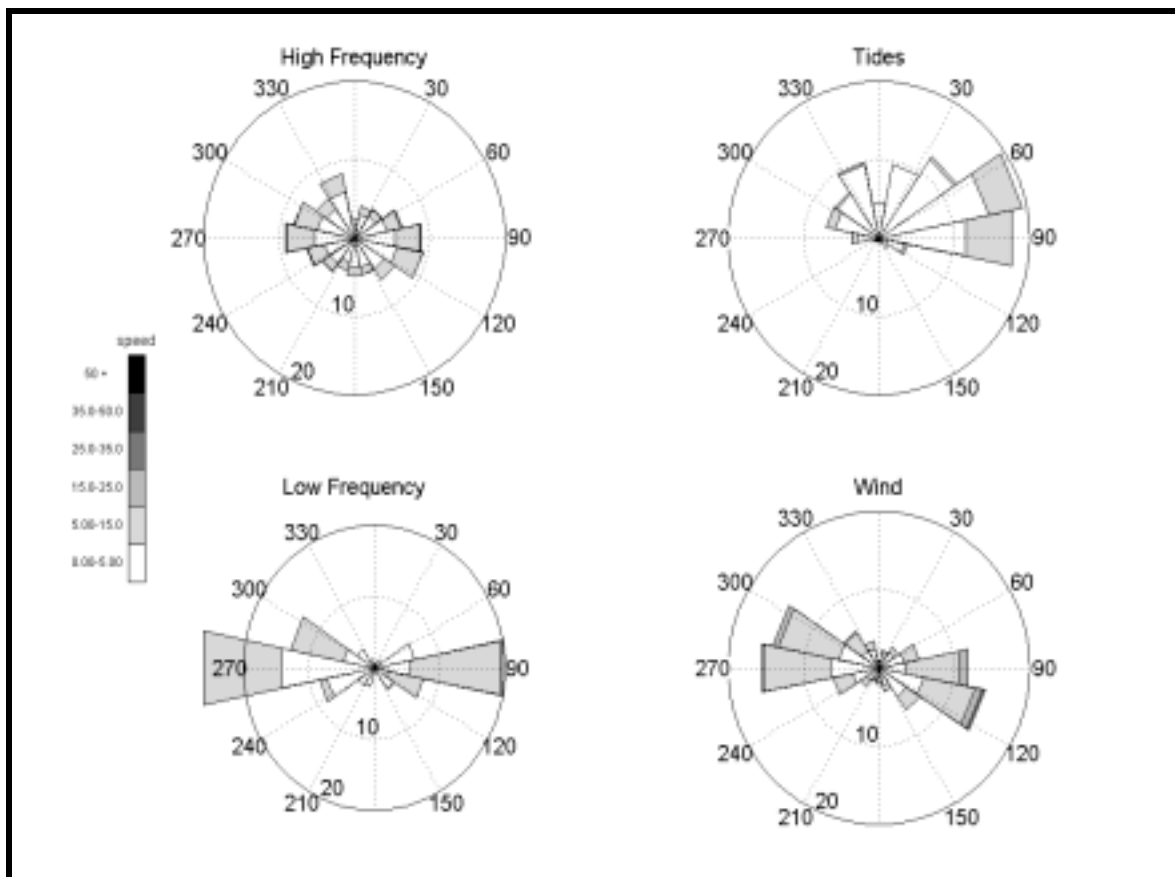

Figure 5-9. Rose diagrams for individual processes at Mooring 4S (near-surface). These data illustrate that wind influence was primarily in the alongshore direction, the high- and low-frequency currents possessed the greatest directional variability, and that tides flowed predominantly to the east-northeast.
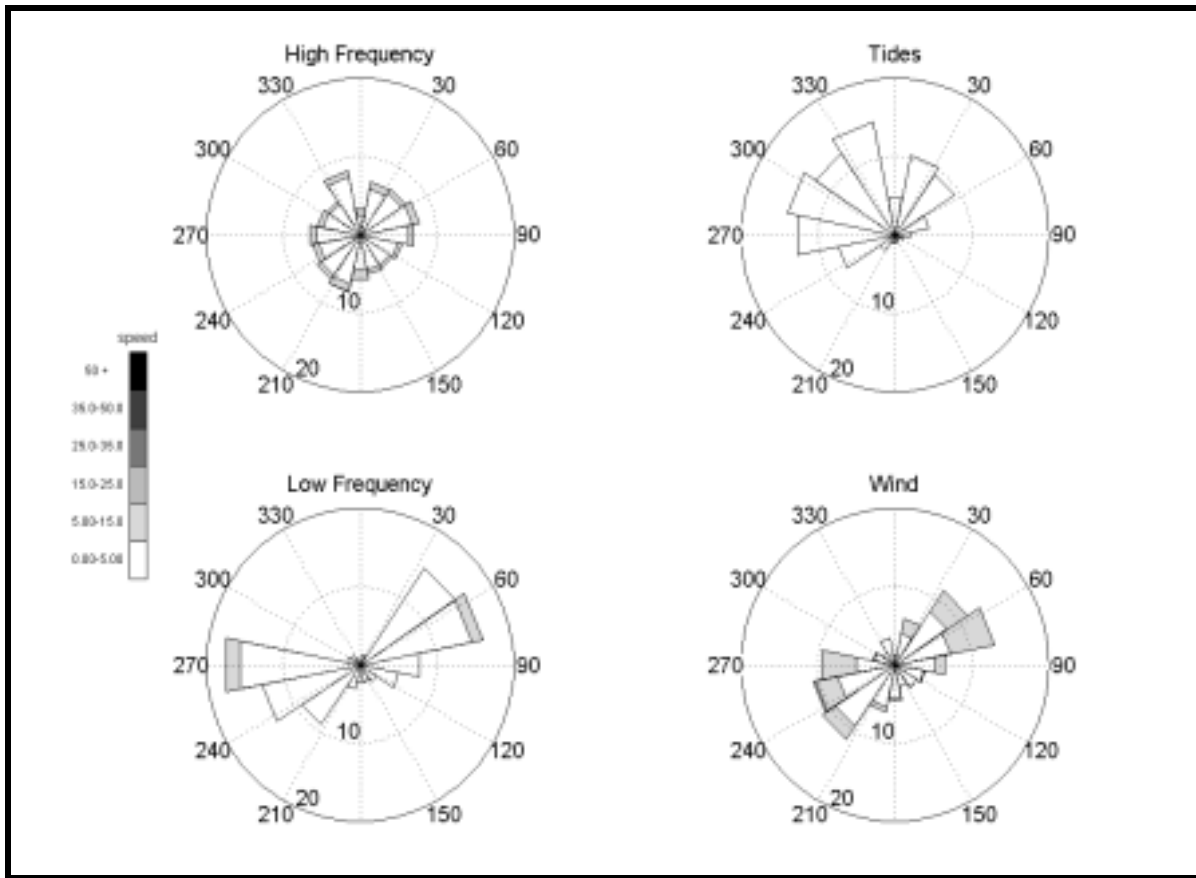
Figure 5-10. Rose diagrams for individual processes at Mooring 4B (near-bottom). These data indicate that wind influence was rotated counter-clockwise relative to surface currents (Figure 5.9), that high- and low-frequency currents possessed the greatest directional variability, and that tides flowed predominantly to the northwest.

An explanation for this vertical counterclockwise rotation may be found by exploring the cross-shore response to wind stress. West winds (winds from the west) force flow to the east and create an upwelling-favorable situation, where the surface flow will tend to drift slightly offshore (or to the right in the northern hemisphere). This drift to the right of a west wind creates a small cross-shore component directed offshore. This offshore component at the surface requires an onshore return flow along the bottom to balance. This balance maintains a cross-shore circulation cell, where bottom water will be driven on-shore, or up-welled, in response to offshore drift of surface flow. East winds will create a downwelling-favorable situation, where surface flow to the west will tend onshore, with bottom waters balancing this cross-shore cell with a slightly offshore bias. Thus, for east winds, the surface flow will tend slightly to the right of the alongshore direction, with bottom waters tending slightly to the left (or onshore) of the alongshore direction. For west winds, the surface flow will again be slightly to the right of the alongshore direction, with bottom waters deflected slightly to the offshore side of the alongshore direction. This cross-shore balance, combined with direct wind forcing, creates the effect of a counter-clockwise rotation of flow with increasing depth. The same counterclockwise rotation of flow in the vertical was observed by Murray (1970) analyzing inner-shelf flow response to high winds during Hurricane Camille.

The rose diagrams for tidal currents at site 4B (Figure 5-9 and Figure 5-10) illustrate different behavior for near-surface tidal currents versus near-bottom tidal currents. Tidal currents at the surface appear to flow to the east-northeast most of the time, with little or no current to the southern

136

quadrants of the compass. Tidal current speeds were below 15 cm/sec most of the time. At the bottom, tidal behavior was quite different than at the surface. Tides flowed to the northwest quadrant most of the time. Near-bottom tidal currents were less than 5 cm/sec most of the time.

5.1.1.4 Seasonal Variability

The previous section provided evidence that currents along the inner shelf were controlled primarily by surface winds. Currents with 1 to 15 day periodicity (termed wind-driven currents) were shown to be the largest contributor to overall observed currents. Analysis of historical data sets also revealed that wind-driven currents were steered by local bathymetric features. Thus, predominant current directions were controlled not only by the direction of alongshore wind but also by the shape of the shoreline and bottom boundaries. Winds with a western component (from the south-southwest to the north-northwest) appeared to drive flow generally in the alongshore direction to the east. The pattern reverses for winds from the east, which tend to push flow alongshore to the west. This understanding implies that seasonal variability of currents within the sand resource areas is likely to be governed by seasonal wind characteristics.

Figure 5-11 shows the frequency-of-occurrence distribution of currents for the winter (December to February), spring (March to May), summer (June to August), and fall (September to November) seasons for Shell Block 132 observations. This figure represents the directional distribution of flow during specific time periods, and is a further synthesis of data presented in
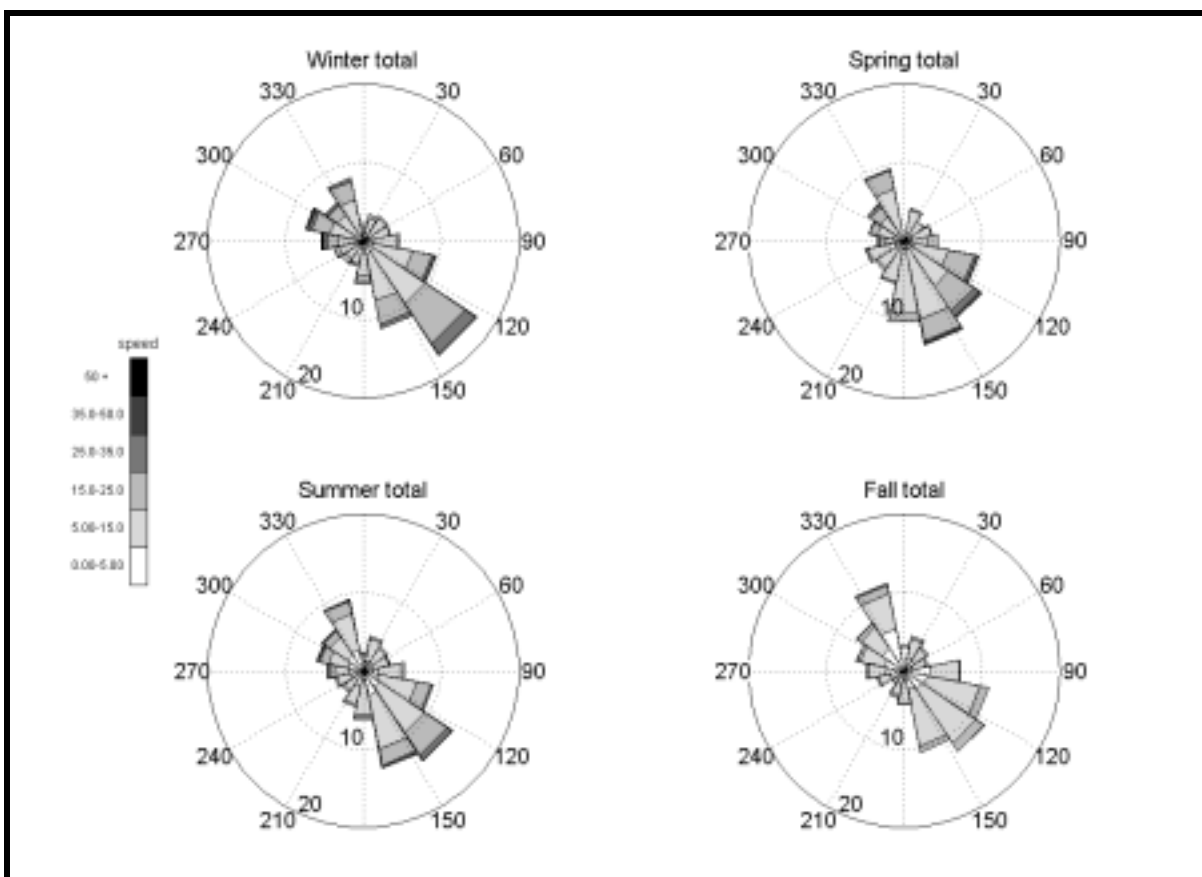

Figure 5-11. Rose diagrams for seasonal currents observed at Shell Block 132 (near-bottom currents). The individual plots represent the original time series divided into seasonal periods.

Figure 5-7 (upper left plot). The data show that the direction of flow changed little with season and maintained a predominant orientation parallel to isobaths. There was also the indication of strengthened flow in the winter, when flows exceeding 15 cm/sec occurred more frequently than at other times of year. The diagrams for the spring and summer seasons show that currents exceeding 15 cm/sec occur less frequently in the spring than in winter; the frequency of these stronger currents diminished further into the summer. For this data set, it appears that currents observed between September and November were the weakest.

Existing literature suggests the wind climatology of this region is influenced in winter by periodic intrusions of cold Arctic air fronts and in summer by milder tropical air due to the northerly position of the Atlantic Bermuda High pressure zone. In winter, stronger northerly winds were more common, while in summer milder southern winds were predominate. Figure 5-12 illustrates observed wind data from the 1987 to 1988 time period separated into winter (December-April) and summer (May-October). Wind-driven currents during this time period are also shown. Wind patterns
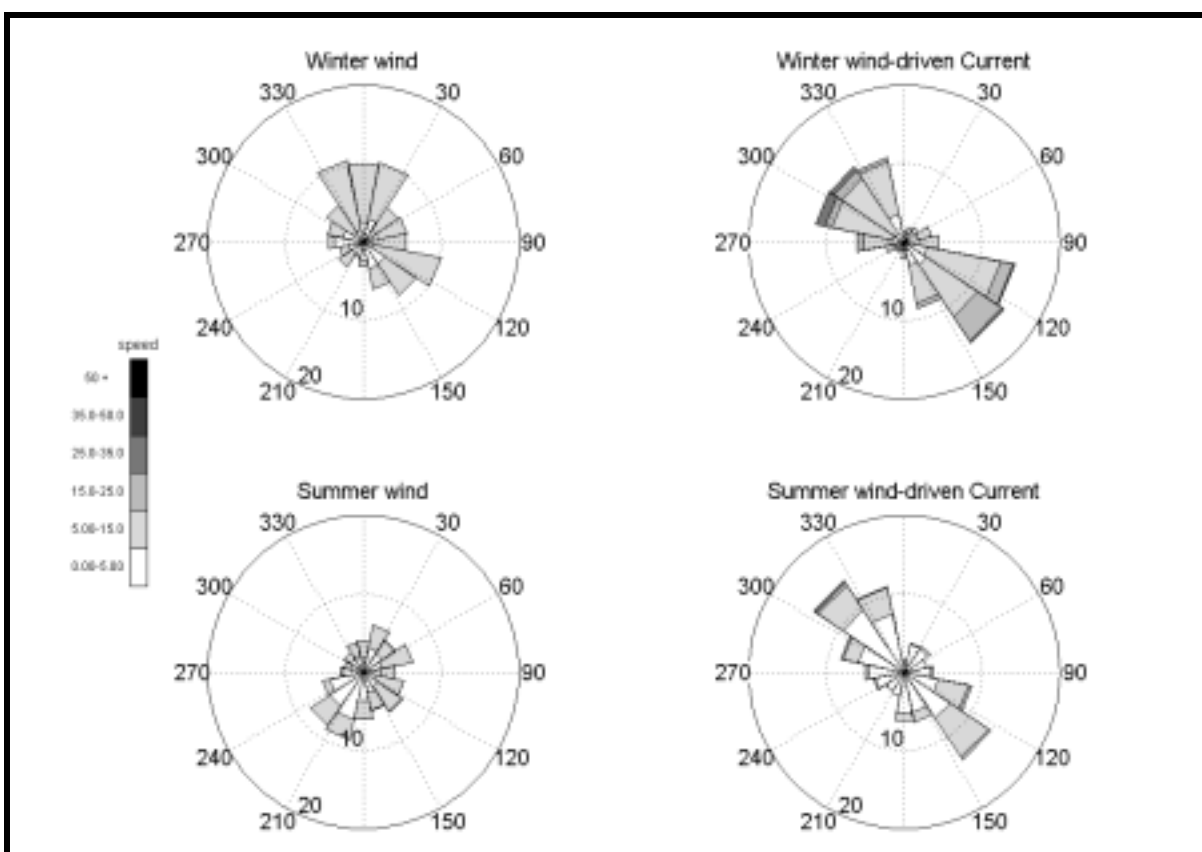

Figure 5-12. Comparison of seasonal winds versus seasonal wind-driven currents for Shell Block 132 (near-bottom) observations. Wind data were obtained from the NOAA station on Dauphin Island. Wind speed units are m/sec; current speed units are cm/sec. Radial circles of each plot represent the frequency of occurrence (in percent); the outer radius depicts 20%, the inner annulus depicts 10% occurrence.

during this period were consistent with historical observations, showing winter winds relatively strong and from the north, with a significant but less frequent southeastern direction. The summer winds were generally weaker and more frequently from the southwest. Wind-driven currents maintained an alongshore direction (northwest to southeast) and were generally consistent with variations in seasonal wind strength. In summer, wind-driven currents exceeded 5 cm/sec approximately 23%

of the time and exceeded 15 cm/sec only about 3% of the time. In winter, wind-driven currents exceeded 5 cm/sec approximately 60% of the time, 15 cm/sec 13% of the time, and greater than 25 cm/sec 3% of the time. In summer, wind-driven flow did not exceed 25 cm/sec.

The analysis suggests that while local bathymetric features govern the predominant directional axis of flow, driving the current in the direction of the alongshore wind stress, it is the strength of the wind that gives an indication of the strength of the current. Throughout the year, flow observed at Shell Block 132 ran either to the southeast (if winds were generally out of the west) or to the northwest (if winds were generally out of the east). In winter, when wind speeds were relatively strong, wind-driven currents also were strong. In summer, when mild wind conditions were most common, flow was relatively weak.

5.1.2 Field Data Collection

Field measurements of currents within the Sand Resource Areas 2 and 4 were conducted in Spring and Fall of 1997. The purpose of these measurements was to observe spatial flow-variations in eastern and western portions of the study area. A total of four surveys were completed; one survey in each of Areas 2 and 4 in the Spring and Fall of 1997. The results of the surveys yielded observations on flow variations throughout the region, and were used in concert with long-term historical current data to augment our understanding of flow characteristics on the inner-continental shelf offshore Alabama.   The observations support the results of historical data analyses, suggesting the flow offshore Alabama is dependent upon local bathymetry and changes in wind conditions; tides appear to have little effect on the observed flow.

This section briefly describes field data collection procedures, including instrumentation, survey techniques, and data processing.   Furthermore, flow conditions observed at each site during the surveys are discussed. The setup conditions determining flow characteristics (i.e. winds, tides, freshwater discharge) were different during each survey. The following discussion describes how flow in Areas 2 and 4 responded to different forcing conditions. Survey data results are presented in more detail in Appendix D5.

5.1.2.1 Survey Instrumentation and Techniques

Each survey was designed to measure currents throughout the east and west portions of the study area during an approximate 12-hour period. A survey transect grid was created with transect lines traversed repeatedly throughout the survey.   Currents were measured using an acoustic doppler current profiler (ADCP) mounted rigidly to a small vessel. The ADCP is capable of high-resolution measurements of the vertical structure of current flow beneath the instrument transducer. When mounted to a moving platform, such as a small vessel, and used to traverse regional areas, a detailed synoptic view of the current field can result. Repeating these transects at regular time intervals throughout a complete tidal cycle provides a method for evaluating the spatial and temporal variation in current structure in the study area.

The survey transect lines were designed to approximate a butterfly pattern, with two parallel lines running cross-shore (longitudinally north-to-south) separated by approximately 5.6 km (3 nautical miles). Two return lines were run diagonally from the (offshore) end of one cross-shore line to the start of the second cross-shore line in the near-shore zone. The intersection of the two diagonal return lines was located in the approximate center of each sand resource area. The two north-south longitudinal transects were traversed in the offshore-onshore direction, while the two diagonal return lines were run in the onshore-offshore direction.

Each line was completed in approximately one hour, with an entire four-line cycle traversed every four hours. The transect schedule allowed for three complete cycles for Area 2, and two and a half complete cycles for Area 4. The intersection point (center of the sand resource area) was

passed at twice the cycle frequency, resulting in six measurements in the center of the site (once every two hours) per survey. This survey technique provided adequate spatial coverage of the sites with reasonable synopticity, and it was designed with the cross-shore bias to more adequately observe the more dominant alongshore flow processes.

For this study, the ADCP was configured to balance maximum accuracy with reasonable vertical resolution, resulting in a standard deviation (or accuracy of current measurement) of approximately 1.3 cm/sec. The vertical resolution was 1 m, or one velocity observation every 1-m water depth. Each vertical profile took approximately 4 seconds to collect. Averaging parameters resulted in a horizontal resolution of approximately 10 to 12 m along the transect line.

Position information was collected using Hypack, an integrated navigation software package running on a PC computer, linked to a NorthStar 941DX differential GPS. Position data were read from the device in WGS-84 coordinate system and transformed on-the-fly to NAD 1983 State Plane Alabama West zone. Position updates were available every 2 sec, although brief interruptions of position data were experienced when thunderstorms were in the area. These brief losses of position data (less than 10 sec) did not compromise results. Raw position data was also sent to the ADCP Toshiba laptop to assist in verifying clock synchronization between the GPS and ADCP.

The survey resulted in two types of data: current velocity profiles (or ensembles) and vessel position. The ADCP data for a single transect consisted of velocity components at every depth bin for every profile. For these surveys, the two earth-referenced velocity components (V_{east} and V_{north}) were reported, as well as current speed, current direction, and error velocity. The conversion process outputs each ensemble profile as a function of depth (i.e., V_{east} vs. depth, V_{north} vs. depth, etc.). The entire data file represents each ensemble profile along the transect. Approximately 1000 individual profiles were obtained per transect. Twelve (12) transects were completed each survey day, resulting approximately 12,000 independent current profiles through the study area per day.

Position data were recorded as time-northing-easting within Hypack. The ensemble profiles were merged with the position data to assign a unique x-y pair to every ensemble. This merging operation was done using time and GPS position as the common link between the Hypack and ADCP data files. By searching for the unique position at a specific time for each of the data sets, an accurate x-y location was assigned to each ensemble.

Current measurements were presented as vector maps throughout the survey areas. The vector maps represented spatially-averaged current velocities at specific locations within the survey domain. Velocity profiles were separated into near-surface, mid-depth, and near-bottom layers, and grouped within discrete segments along the transect paths. Each survey transect was divided into 16 segments, with an average velocity value calculated for each transect segment at the three depth layers. Each segment was approximately 450 m (1500 ft) long. The resulting vector was located within the center of each segment. The vectors corresponding to a single survey cycle (4 transects) were then displayed on an area map. These vector maps were produced for each of the three depth layers and for each of the three survey cycles. Each survey cycle took approximately four hours to complete. A series of plots shows temporal and spatial variation in horizontal and vertical currents during the survey. A complete set of vector maps for each survey is presented in Appendix D5. Examples of the data will be presented in the next section.

5.1.2.2 Spring 1997 Survey Results

Sand Resource Area 4 was surveyed May 21, 1997. This site is located immediately south of eastern Dauphin Island (Figure 1-1). The area has complex bathymetric features associated with the Main Pass ebb-tidal delta that influence local circulation patterns. Flow exchange between the Bay and the inner shelf occur primarily through Main Pass. The northeast corner of the area is highlighted by sloping bathymetric contours (along a southeast-northwest axis) which define Pelican Island, a portion of the ebb-tidal delta due south of the eastern tip of Dauphin Island and to the north

of the sand resource area. The ebb-tidal delta is dissected by the dredged channel at Main Pass. An experimental sediment mound lies in the center of the Area 4; elevations on the mound are 2 to 6 m higher than the surrounding region (Hands, 1994). Sand Resource Area 2 was surveyed May 22, 1997. This site is east of the entrance to Mobile Bay in a region of complex bathymetry associated with shore-oblique linear shoals across the entire continental shelf. However, abrupt bathymetric changes related to ebb shoals at Main Pass likely have greater influence on shelf flow patterns throughout the study area.

In the days preceding the surveys, winds were generally blowing onshore (from the south or southeast) at 10 to 15 kts (Figure 5-13). Winds shifted south-southwest three days before the survey. These southwest winds abated to less than 10 kts. On May 21, the day of the Area 4 survey, winds were approximately 10 kts from the west. During the survey, field notes document intense rain squalls and thunderstorms passed the area. On the night of May 21, the winds shifted offshore (from the north) with speeds less than 10 kts. The winds strengthened to 12 to 15 kts in the morning of May 22 and originated from the northeast. These winds calmed during the afternoon of the Site 2 survey to approximately 5 kts.

Tidal elevations during the survey were collected from the NDBC site on Dauphin Island (Figure 5-14). Diurnal tides dominate the region, specifically the K1 and O1 tidal constituents, resulting in one high and one low each day. On May 21, 1997, low water occurred after midnight and high water was observed in early afternoon (1500 hours). The tide range on this day was of order 0.4 m, which appeared to be close to the maximum tidal range in the tropic/equatorial cycle. On May 22, 1997, low water occurred at approximately 4 AM (EDT) and high water was observed at approximately 1600 hours (EDT).   The tide range on this day was also 0.4m.

Salinity profiles obtained by CSA during the survey showed the surface layer at all sites to be less saline than underlying layers (see Table 5-2), particularly those close to the mouth of Mobile Bay. Sand Resource Area 1 showed the least vertical variation in salinity, suggesting the freshwater plume had not been carried fully to that location. The strong vertical density stratification between surface and underlying layers affects the flow regime (Stumpf et al., 1993), and it may help to explain both the spatial and temporal current variations observed during the surveys.
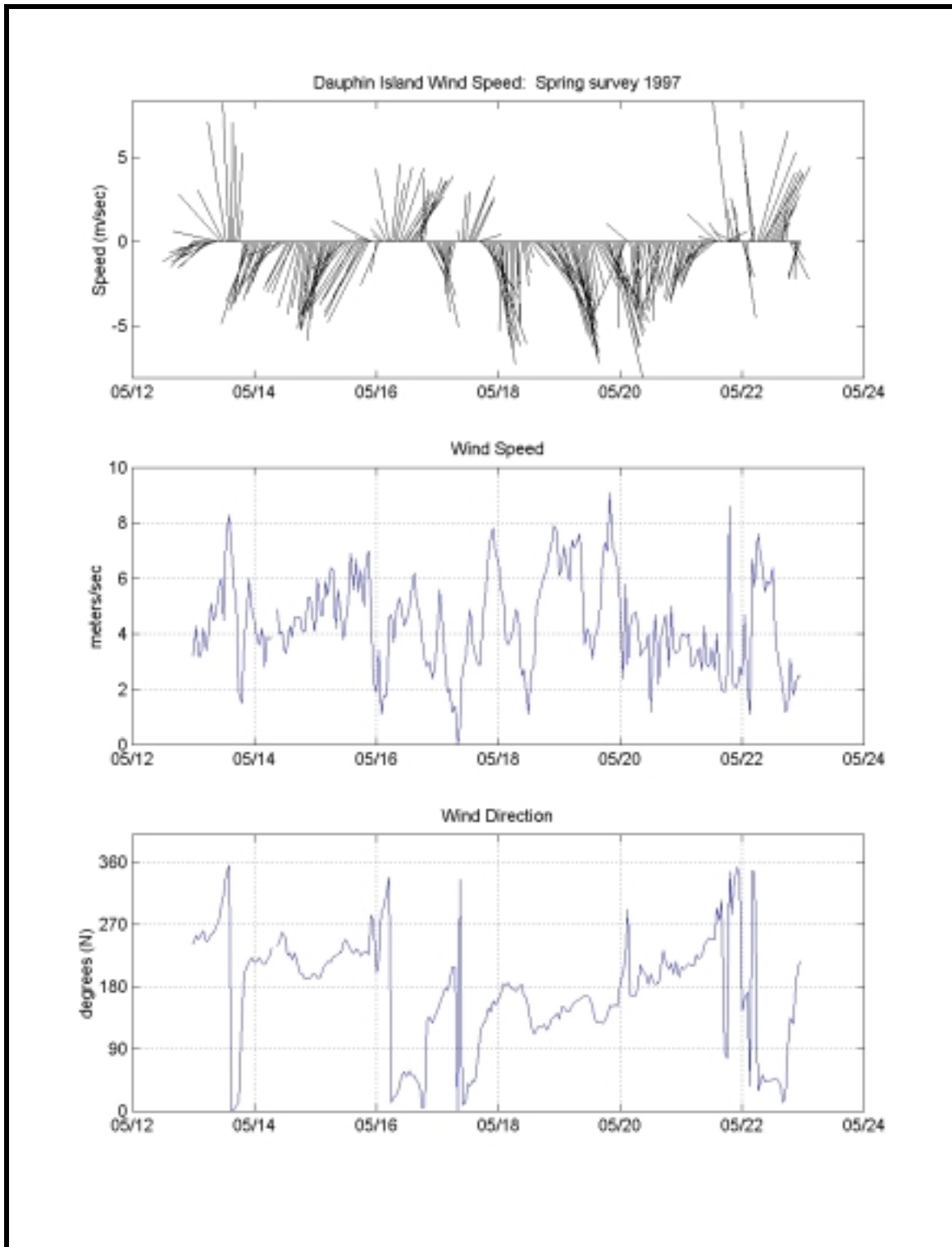
Figure 5-13. Wind conditions prior to and during the field surveys on May 21-22, 1997. Dashed grid lines depict 0000 hours of the day labeled on the bottom axis. Winds are reported as direction from which the wind is blowing.
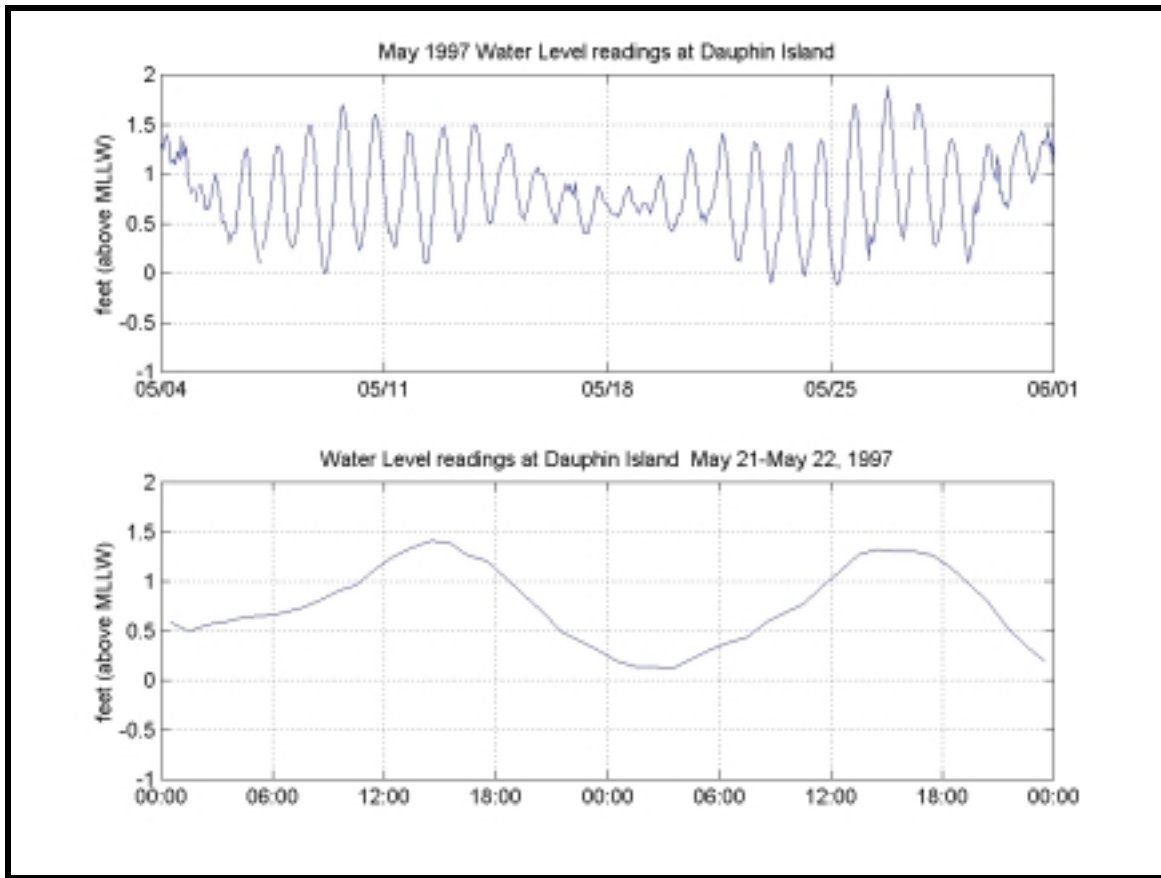
Figure 5-14. Water elevation readings obtained from the NDBC station on Dauphin Island prior to and during field surveys on May 21-22, 1997.

Table 5-2. Average salinity profiles at sand resource areas 1 – 5 May 1997					
Practical Salinity Units					
Depth Layer	Area 5	Area 4	Area 3	Area 2	Area 1
Surface	18.8	20.2	17.8	19.6	26.6
Mid-layer	30.0	30.5	27.5	26.6	30.2
Bottom	33.6	33.5	28.3	28.4	31.9
Obtained by Continental Shelf Associates, Inc. (see Section 6.0).					

Spatial Variability at Sand Resource Area 4

The vertical and horizontal variability observed at Area 4 appeared to be due to flow exchange with Mobile Bay, as well as modifications of the flow regime by bathymetric features. The surface and mid-layer currents observed during the survey showed small horizontal variation at any given time (Figure 5-15). Flow in these upper layers was directed primarily west to east, responding to the westerly longshore component of the winds that had been blowing for the previous few days. Flow in the southern (deeper) portion of the area was to the east, consistent with the direction of the depth contours, with amplitudes of approximately 25 to 35 cm/sec. Flow in the northern (shallow) regions was southeast, steered by the local bathymetry around Pelican Island, with similar magnitude as flow in deeper areas. Surface flow was greater (25 to 35 cm/sec) than flow in the mid-depth layers (20 to 25 cm/sec). Flow in the upper vertical layers of Area 4 appeared to be dependent upon the shape and direction of the bottom depth contours.
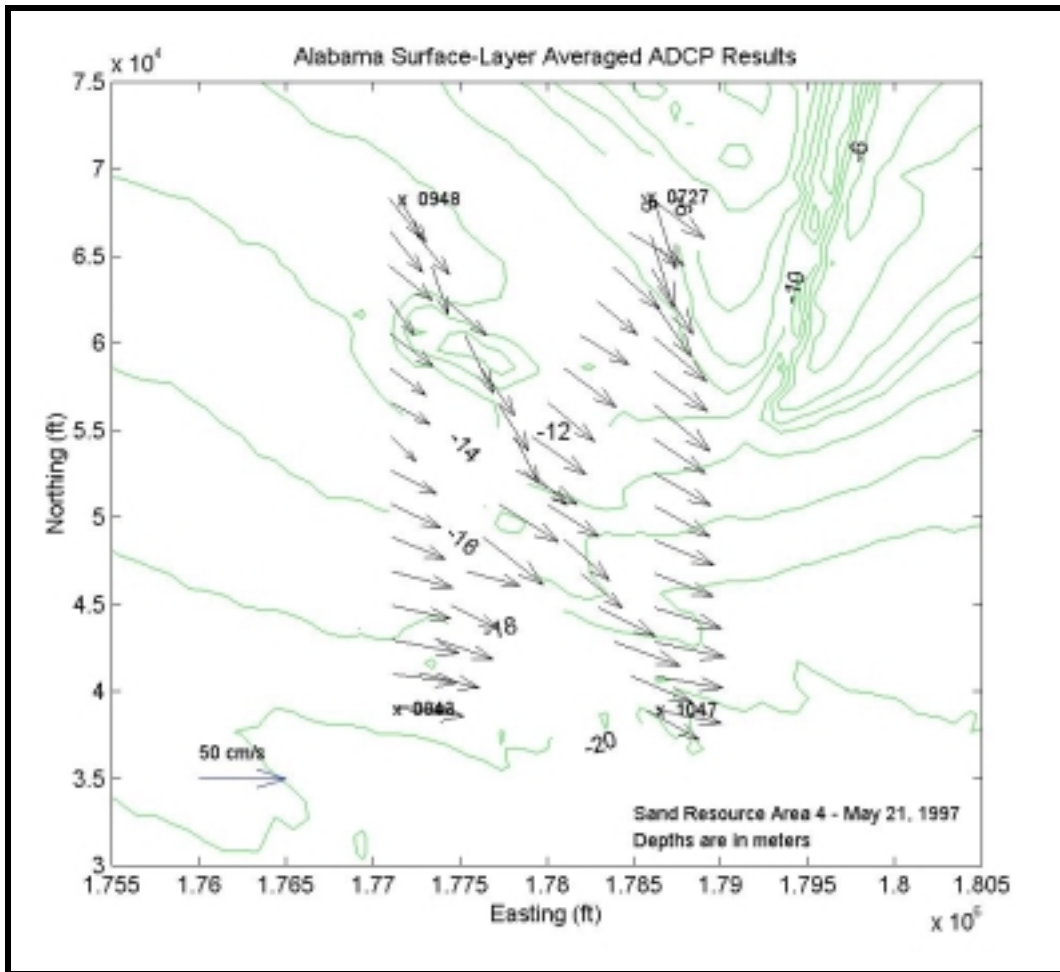
Figure 5-15. Vector map of observed flow patterns for Sand Resource Area 4; May 21, 1997 from 0727 hours to 1150 hours. Current vectors represent average flow in the surface layer only (upper one-third of the water column). Bathymetry of Main Pass is noted in the upper right of the figure. The numbers in each corner of the transect grid (0727, 0948, 0848, and 1047) state the time (hour of day) that the transect line was started.

.   Bottom flow was not similar to surface flow. During a rising tide (early in the survey only), current vectors along the seafloor were oriented toward the mouth of the Bay, which was perpendicular (not parallel) to the bottom depth contours, with speeds approximately 15 to 25 cm/sec (Figure 5-16). The vectors varied slightly in the bottom layer, but each appeared directed toward the narrow Main Pass opening between Pelican Island and Mobile Point. As tide slackens later in the survey, bottom vectors changed to a west-east orientation, consistent with overlying layers.

The dredged material mound located within the northeast quadrant of the sand resource area appeared to modify the bottom flow field weakly, as current vectors shown near the sediment mound (Mobile Outer Mound; Hands, 1994) bend slightly around the obstruction.   No significant acceleration of currents was noted due to this diversion.
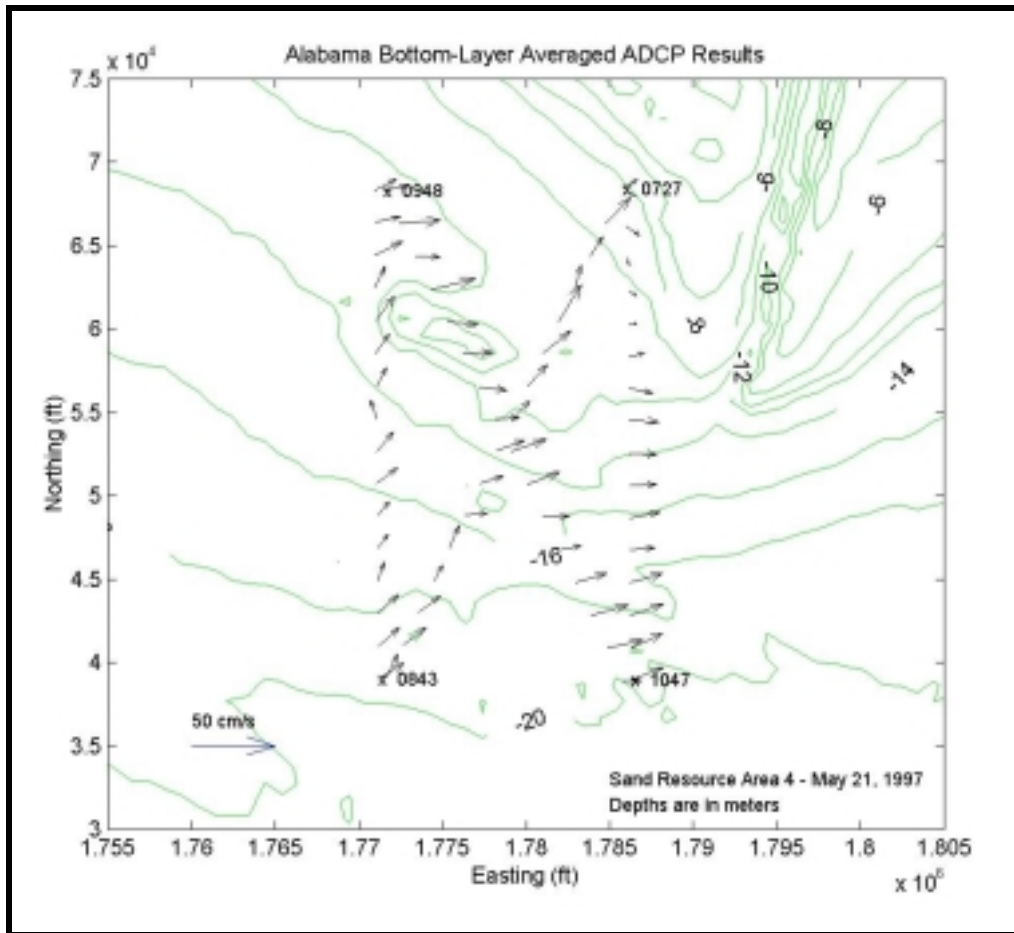
Figure 5-16. Vector map of observed flow patterns for Sand Resource Area 4; May 21, 1997 from 0727 hours to 1150 hours. Current vectors represent average flow in the bottom layer only (lower one-third of the water column).

During the survey, the current regime appeared to respond to temporal changes in tide as well as wind. Early in the survey, water elevations at Dauphin Island approached a peak (high tide was approximately at 1500 hours). The flood of water into the Bay early in the survey was observed along the bottom in areas closest to the Main Channel. Mid-way through the survey, flood flow at the bottom weakened to near-zero conditions (Figure 5-17). When the tide was ebbing from Mobile Bay, bottom currents exhibited alongshore flow consistent with the upper layers. These observations illustrate the manner in which water flows into Mobile Bay in the presence of a persistent freshwater outflow. The near-constant freshwater plume discharged from Mobile Bay at this time may create a vertical layering to the water column, with less-dense fresh water atop a dense layer of ambient shelf water. Surface water discharged from the Bay to the inner shelf is driven either east or west depending on the direction of local winds. Tidal exchange between the inner shelf and the bay may occur in bottom and, to a lesser extent, mid-depth layers as dense shelf water floods into Mobile Bay along the bottom and less-dense fresh water from Mobile Bay is discharged at the surface.
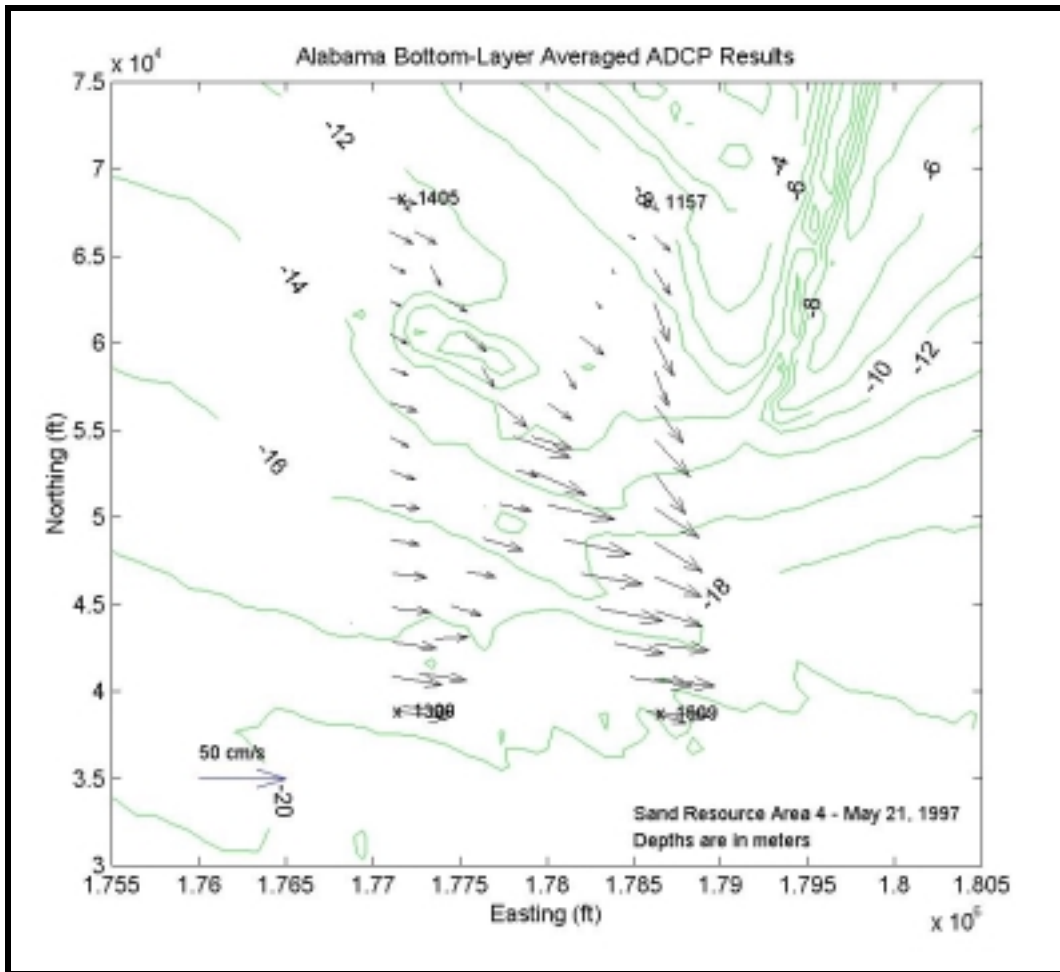
Figure 5-17. Vector map of observed flow patterns for Sand Resource Area 4; May 21, 1997 from 1157 hours to 1620 hours. Current vectors represent average flow in the bottom layer only (lower one-third of the water column).

The surface flow field also demonstrated the tidal influence of Mobile Bay. During flood tide, surface flow was observed west-to-east, consistent with long shore wind forcing in the absence of an inlet. At the northern portion of the area, near the shoals of Pelican Island, surface flow was directed southeast, modified more strongly by the bathymetry than flow in the deeper southern portions of the area. As the tide reached peak approximately mid-day, near-bottom flood currents weakened. However, the surface flow vectors appeared to bend to the southeast around Main Pass, perhaps deflected southerly by a surface discharge from the Bay.

Winds were from the west early in the survey, later in the afternoon wind squalls and thunderstorms passed the area, creating localized flow responses to this variable wind field (Figure 5-18). When wind squalls were observed later in the afternoon the surface flow was quite variable, with directions changing by more than 90° in less than three hours. This directional variability was detected most noticeably in shallow regions to the north, demonstrating the rapid response of the surface flow field to changes in wind stress. Amplitudes of flow during the wind squalls were less than 15 cm/sec, suggesting the wind stress directed to the west may be counteracting the predominant eastward flow.
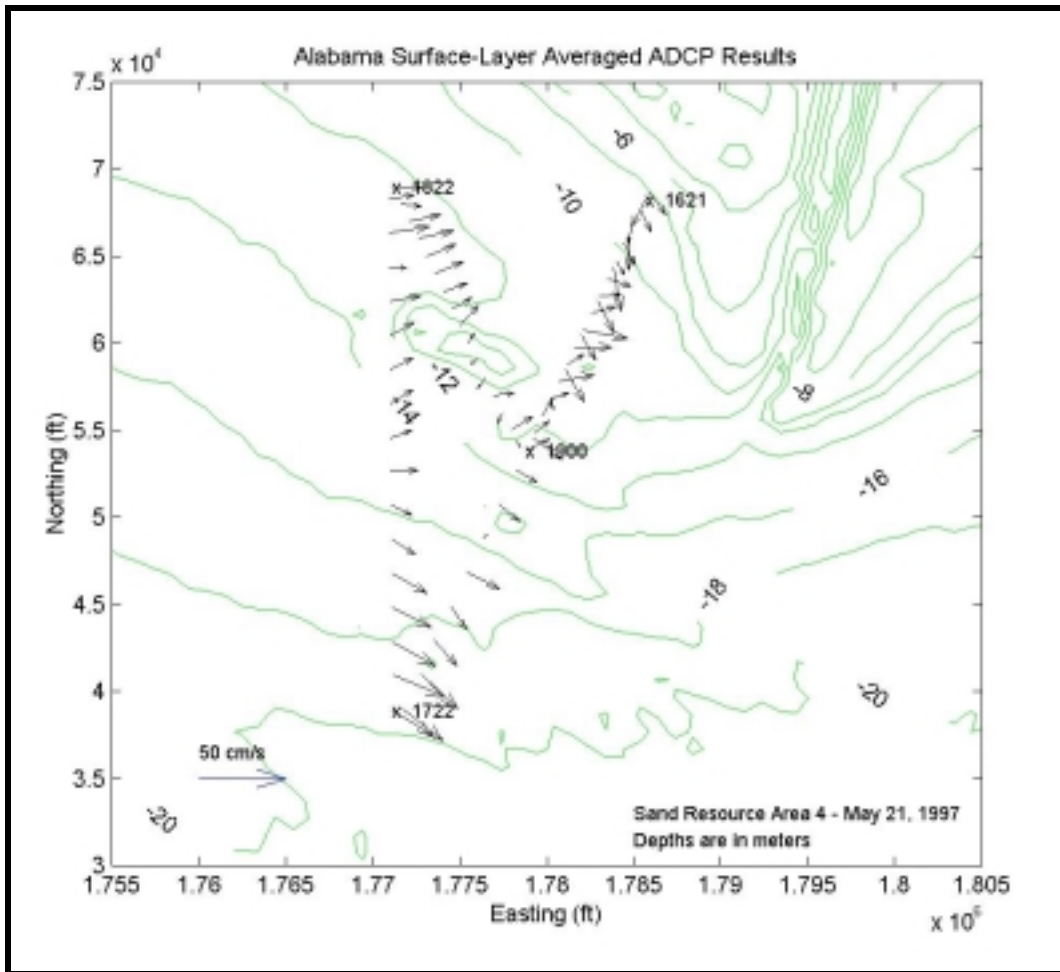
146

Figure 5-18. Vector map of observed flow patterns for Sand Resource Area 4; May 21, 1997 from 1621 hours to 1930 hours. Current vectors represent average flow in the surface layer only (upper one-third of the water column). These currents were measured as wind squalls and thunderstorms passed the area, and demonstrate the rapid response of surface flow to sudden changes of wind speed and direction.

Spatial Variability at Sand Resource Area 2

Sand Resource Area 2 has equally-complex bathymetric relief as Sand Resource Area 4; however, the influence of flow processes at Mobile Bay entrance complicates shelf flow patterns in Area 4. Currents in Area 2 were separated initially into three depth layers: the near-surface layer (1 to 4 m from the surface), the mid-depth layer (4 to 8 m below the surface), and the near-bottom layer (8 to 12 m below the surface). Each of the three layers appeared to possess distinct flow characteristics, with the mid-depth and bottom layers exhibiting a strongly coupled relationship. Near-surface flows appeared to be somewhat decoupled from underlying flows.

Distinctions in flow characteristics between the surface layer and underlying layers can be traced to a strong vertical stratification of the water column, likely resulting from the eastward advection of fresh water discharged from Mobile Bay due to southwest and west winds earlier in the week. An example of a single vertical profile is shown as Figure 5-19, showing the abrupt variation of flow within the upper layer.

Currents in the surface layer were relatively uniform in a directional sense, with flows oriented north-northeast at speeds of approximately 15 to 30 cm/sec early in the day (Figure 5-20). Later
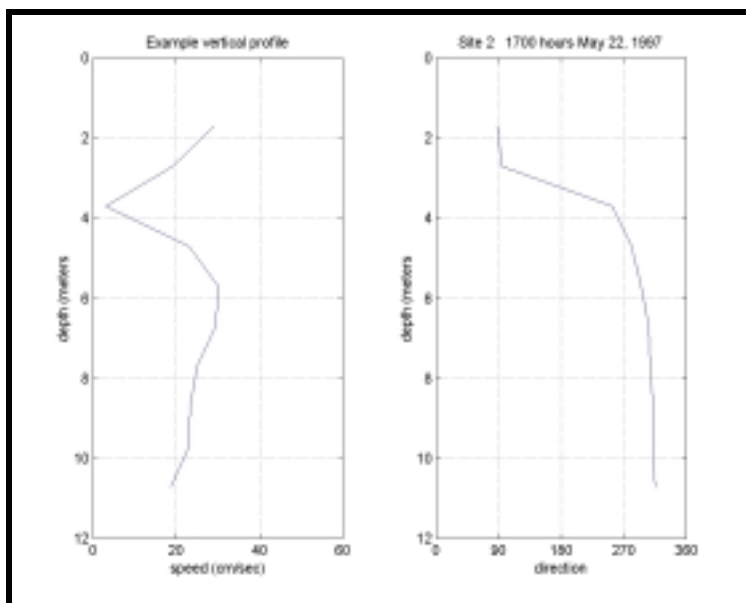
147

Figure 5-19. Example of a single vertical current profile measured in Sand Resource Area 2 on May 22, 1997. Strong vertical shear is apparent, as surface flow was directed to the east (90°) at approximately 35 cm/sec. Mid-layer and bottom flow were directed to the northwest (315°) at about 20 to 30 cm/sec.
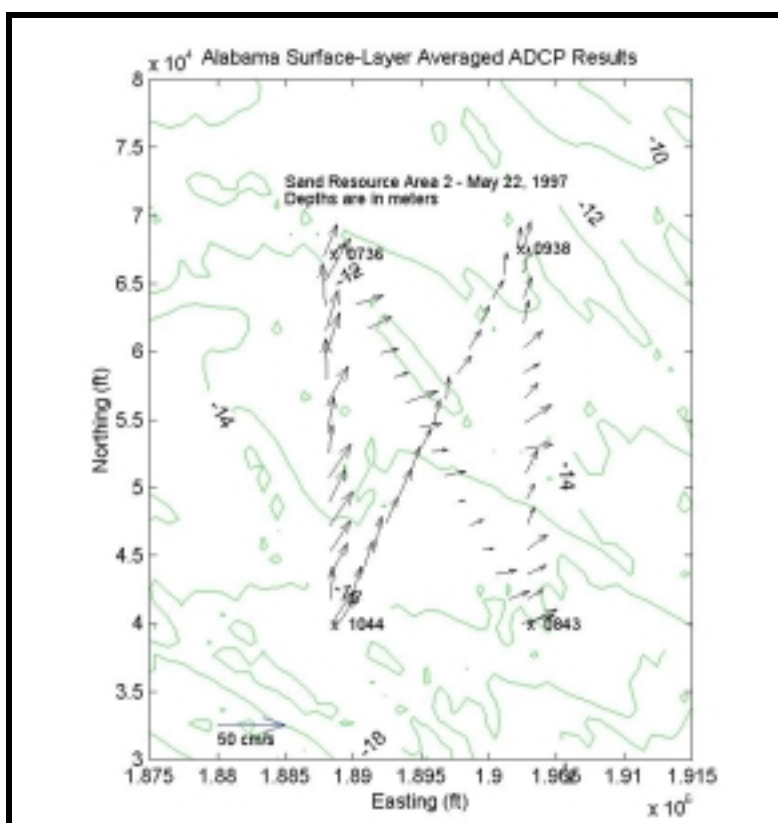

Figure 5-20. Vector map of observed flow patterns for Sand Resource Area 2; May 22, 1997 from 0736 hours to 1130 hours. Current vectors represent average flow in the surface layer only (upper one-third of the water column).

148

in the day, surface currents shifted east-northeast and maintained a range of speeds approximately 15 to 40 cm/sec. The slight shift in current direction may correspond weakly to a shift in wind direction from the north to the northeast. The entire surface flow field appeared oriented in a uniform direction at any one time with little horizontal directional variability. There did not appear to be specific locations within the survey area where some currents were consistently weaker or stronger than others. The range of surface current speeds throughout the survey was approximately 15 cm/sec in isolated locations to more commonly observed speeds of 30 to 40 cm/sec throughout the region.   Speeds of around 45 cm/sec were observed briefly.

The surface layer appeared to be influenced by freshwater discharge from Mobile Bay, as winds had been blowing from the southwest and west for the previous 36 hours. Using an average speed of 30 cm/sec over a duration of 36 hours yields a translation distance of approximately 39 km, a value greater than the distance between Area 2 from the mouth of Mobile Bay. Note that salinity at Area 1, farthest to the east, did not show as strong a vertical gradient in salinity as Areas 3 and 2, suggesting the freshwater plume had not fully reached that far to the east (Table 5-2). The relatively low salinity values measured in underlying (middle and bottom) layers at Areas 3 and 2 suggest that some vertical mixing had occurred between the surface plume and underlying layers.

Mid-depth and near-bottom flows also indicated little horizontal variability for any time period. Flow vectors were oriented in a relatively consistent direction. Near-bottom vectors appeared slightly more variable than mid-depth layer currents, owing to the modification of near-bed flows by bathymetric features. The region is a gently sloping area with few relief features; hence, the observation of low directional variability near the bottom is reasonable. Current speeds decreased with depth and were observed to be approximately 10 to 35 cm/sec in the mid-depth layer and approximately 5 to 25 cm/sec in the near-bottom layer (Figure 5-21). As with observations of surface flow, there did not appear to be localized pockets of weak or strong flow. Speed variability was due more likely to the weak turbulent conditions characteristic of shallow water inner-shelf flow and less dependent upon site-specific behavior resulting from flow modification from seabed bathymetric features.

Two distinct vertical layers (surface and middle/bottom layers) exhibited different temporal changes through the duration of the survey. The surface layer tended to move eastward early in the day, correlated well with the wind direction (from the southwest). Observations that the freshwater plume discharged from Mobile Bay is highly correlated to local wind stress has been reported by Gelfenbaum and Stumpf (1993). As wind shifted to the northeast on the day of the survey, surface currents appeared to rotate slightly to the east-northeast, perhaps as an initial response to the shift in wind direction. The survey did not extend later in the day to observe a continuation of the surface flow field response to this shift in wind direction.

The mid-depth and near-bottom layers appeared to rotate clockwise throughout the survey duration. Mid-depth layers were observed in the morning to flow east-southeast, rotating with time to the southeast (at mid day) and subsequently to the northwest at the end of the survey. The near-bottom layer showed this same rotation, with flow directions oriented east and southeast early in the day, shifting south and then west and northwest late in the day (Figure 5-22). The near-bottom flow was rotated slightly clockwise with respect to the overlying flow. The clockwise rotation of the regional current vectors appeared to make an approximate 180° turn (half a complete cycle) during the approximate 12-hour duration of the survey. This extrapolates to a complete cycle over a 24-hour time period, falling approximately upon both major tidal periods for this region.

The decoupling of surface layer currents with underlying flows was observed during the survey, specifically with surface currents appearing to respond rapidly to variations in wind stress, and the underlying flows forced by processes of longer time scales. Gelfenbaum and Stumpf (1993) report a similar finding in this region, with the upper layer of a stratified water column having little
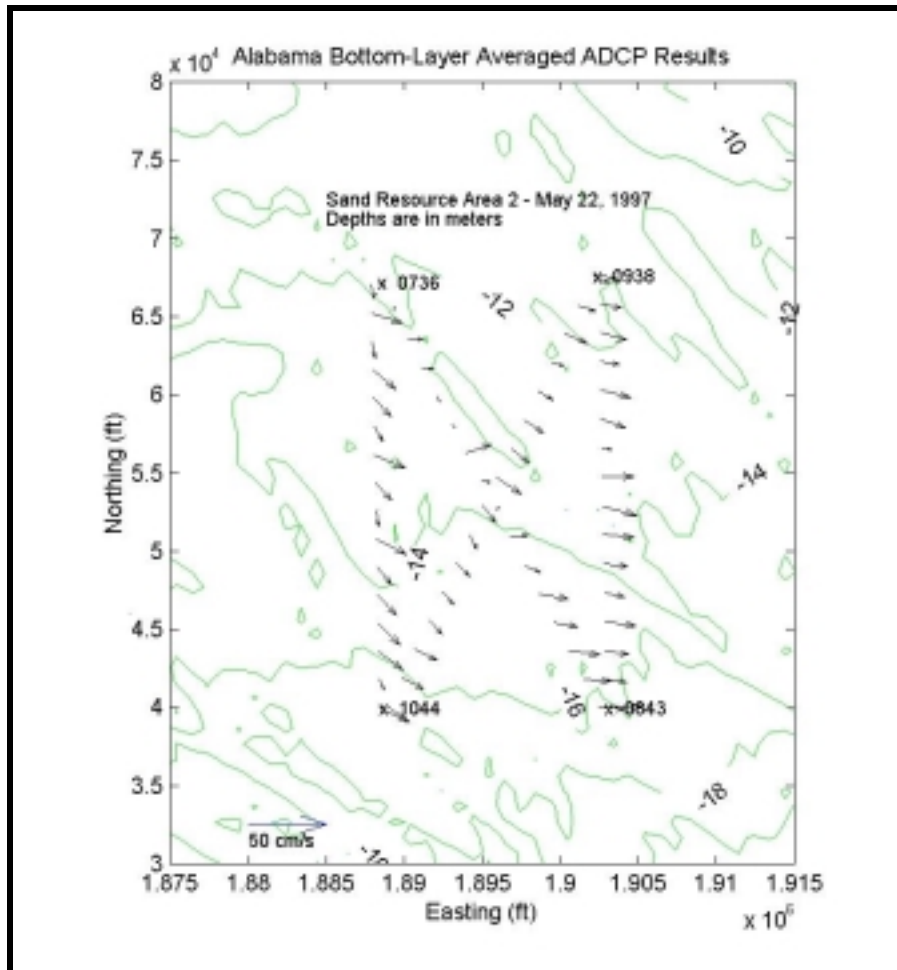
Figure 5-21. Vector map of observed flow patterns for Sand Resource Area 2; May 22, 1997 from 0736 hours to 1130 hours. Current vectors represent average flow in the bottom layer only (lower one-third of the water column).
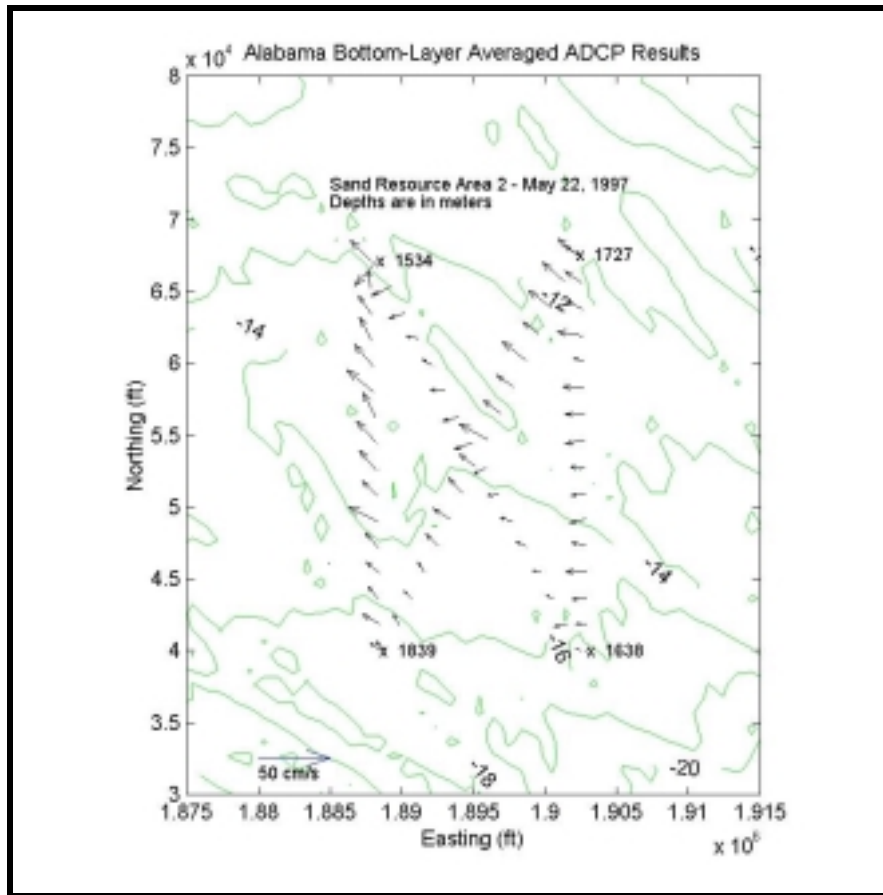
Figure 5-22. Vector map of observed flow patterns for Sand Resource Area 2; May 22, 1997 from 1534 hours to 1929 hours. Current vectors represent average flow in the bottom layer only (lower one-third of the water column). Note the 180° counterclockwise rotation of flow vectors since the beginning of the survey (see Figure 5-21).

effect on the movement of underlying water. These authors suggest two layers do not mix very efficiently in the vertical, however the observation of lower salinity waters in the region (Areas 3 and 2) suggest some vertical mixing between layers can occur.

5.1.2.3 Fall 1997 Survey Results

Area 4 was surveyed again after the summer to determine flow characteristics during a different season. On September 30, the same survey transects were occupied as the Spring survey.   Area 2 was surveyed the following day, October 1, 1997. The wind field was relatively constant, and tidal variation was small. While no discharge data were collected from Mobile Bay, historical data suggest that discharge during the survey was less than discharge during the previous survey in May.

On September 30, winds were steady from the west at about 10 kts (Figure 5-23), weakening slightly in the afternoon. On October 1, winds maintained a speed of 10 kts from the west, shifting north to less than 10 kts during the afternoon.   A strong wind event four to five days before the surveys produced winds from the northwest in excess of 20 kts.   This event persisted for approximately 24 hours.   After this event, winds blew offshore (from the north) at approximately 10 to 15 kts for the next two days. Winds rotated southwest and west at approximately 10 kts during the two-to-three days before the surveys.
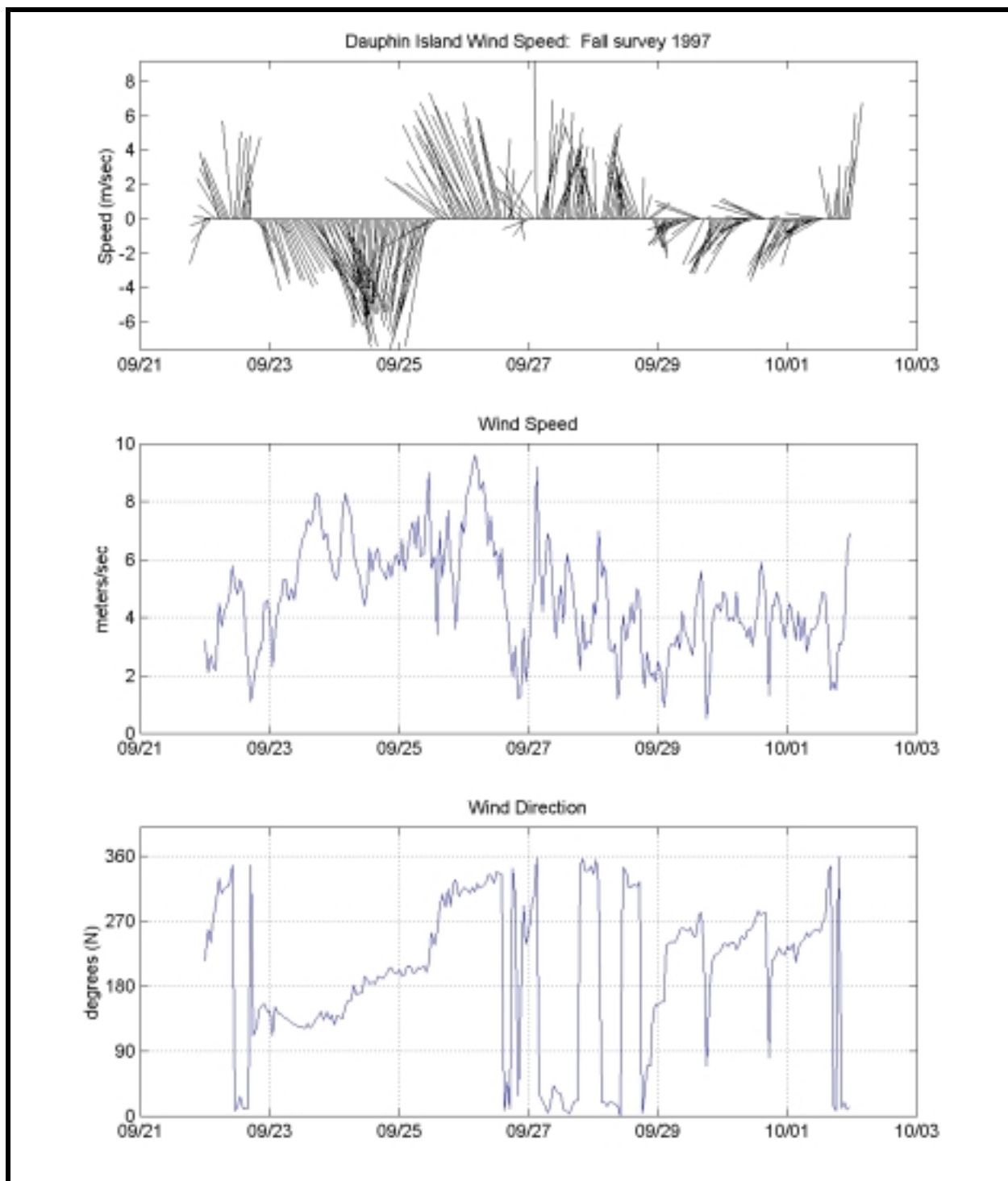
Figure 5-23. Time series of wind speed and direction for 10 days preceding the fall 1997 field survey. Surveys were completed on September 30 and October 1, 1997. The horizontal dashed grid lines represent 0000 hours on the specified day.

Tides during the survey were in the equatorial (minimum) phase, producing small elevation changes at the Dauphin Island station (Figure 5-24). This is in contrast to the spring survey, which occurred during the tropic (or maximum) phase of tide. On September 30, the change in water level was 12 cm. The usual tidal variations observed earlier in the week appeared to be contaminated by non-tidal influences, as the tidal record for October 1 appears almost as a flat line, with a water elevation variation of less than 8 cm. It is unclear what caused this perturbation in the water elevation record.
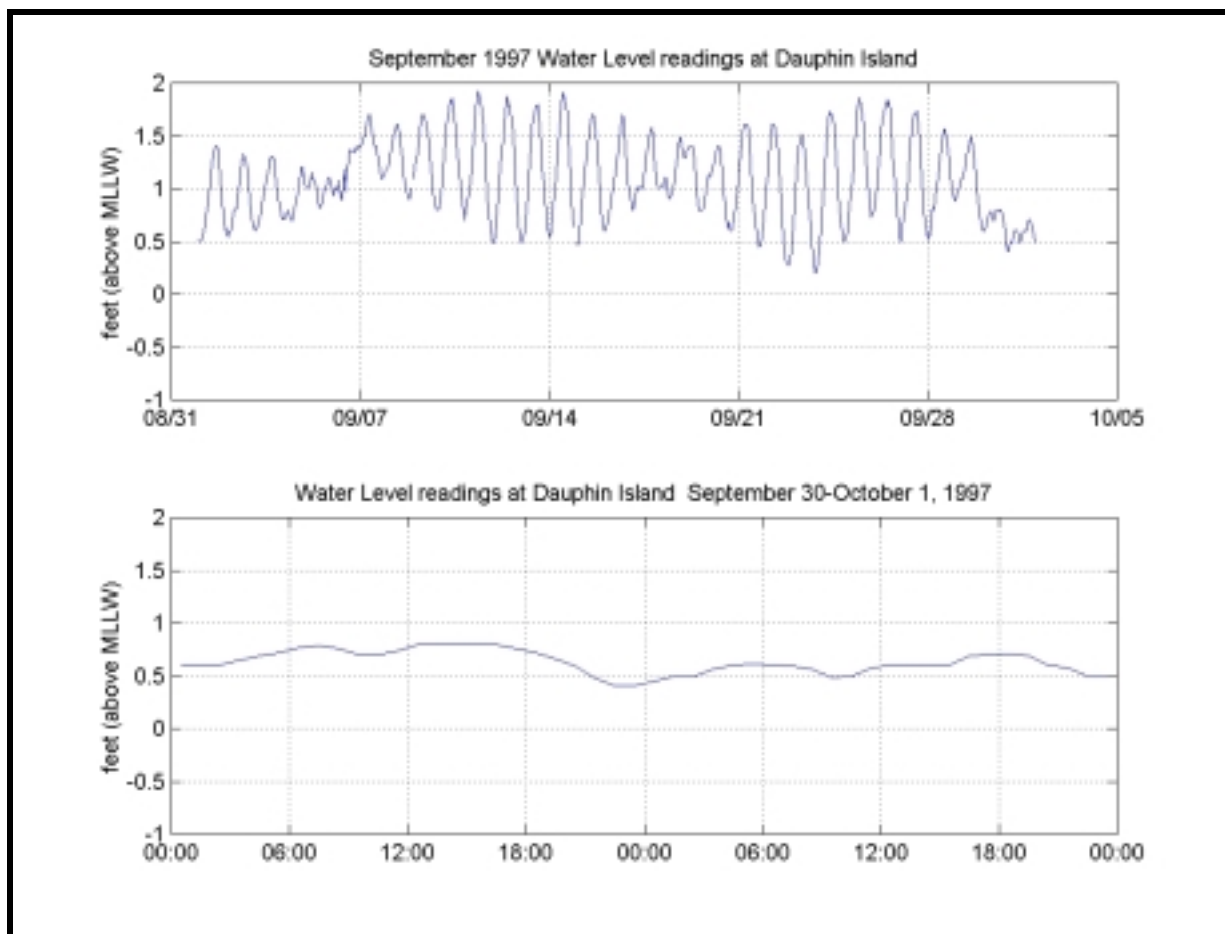

Figure 5-24. Water elevation readings obtained from the NDBC station on Dauphin Island prior to and during the fall field surveys. The data show the tides were near the equatorial (minimum) phase of the cycle on September 30 and October 1, 1997.

The strong vertical stratification observed during the previous survey in May, and resulting decoupling of surface layer versus underlying currents, was absent during the fall. The lack of a highly stratified water column results in more efficient vertical mixing, and therefore, a more homogeneous behavior to the flow field. While no profiles of temperature and salinity were obtained during the October survey, there were profiles obtained during a subsequent cruise in early December, 1997. These observations show the water column to be extremely well-mixed, with little vertical gradient to these parameters. This mixing may be related to two sources; the reduced fresh water input discharged from Mobile Bay in this season, and the more frequent and energetic storms that pass the region during the autumn, providing sufficient vertical mixing forces to the water column.   The absence of vertical variability of currents during the October survey suggests the water column was less stratified than during the May survey.

Spatial Variability at Sand Resource Area 4

Current flow through the region appears to result from wind forcing and shows a dependence upon bottom bathymetry, with the flow generally oriented parallel to depth contours. There was vertical variation between surface and bottom layers, suggesting a well-mixed water column.

Surface flow throughout the sand resource area generally followed the depth contours, with flow in the deeper south regions oriented to the southeast (Figure 5-25). Currents were likely wind-driven, but there could have existed a surface plume discharged from the Bay that may have deflected the flow slightly to the south as well. Currents in shallower regions of the northeast quadrant were also directed to the southeast, including currents measured adjacent to the Main Channel. Currents near the Main Channel appeared to be deflected weakly to the south, perhaps influenced by some surface discharge from the Bay. However, this deflection was observed late in the afternoon when there was a small decrease in tidal elevation at Dauphin Island. The range of speeds for currents measured in the surface layer was 40 to 50 cm/sec.
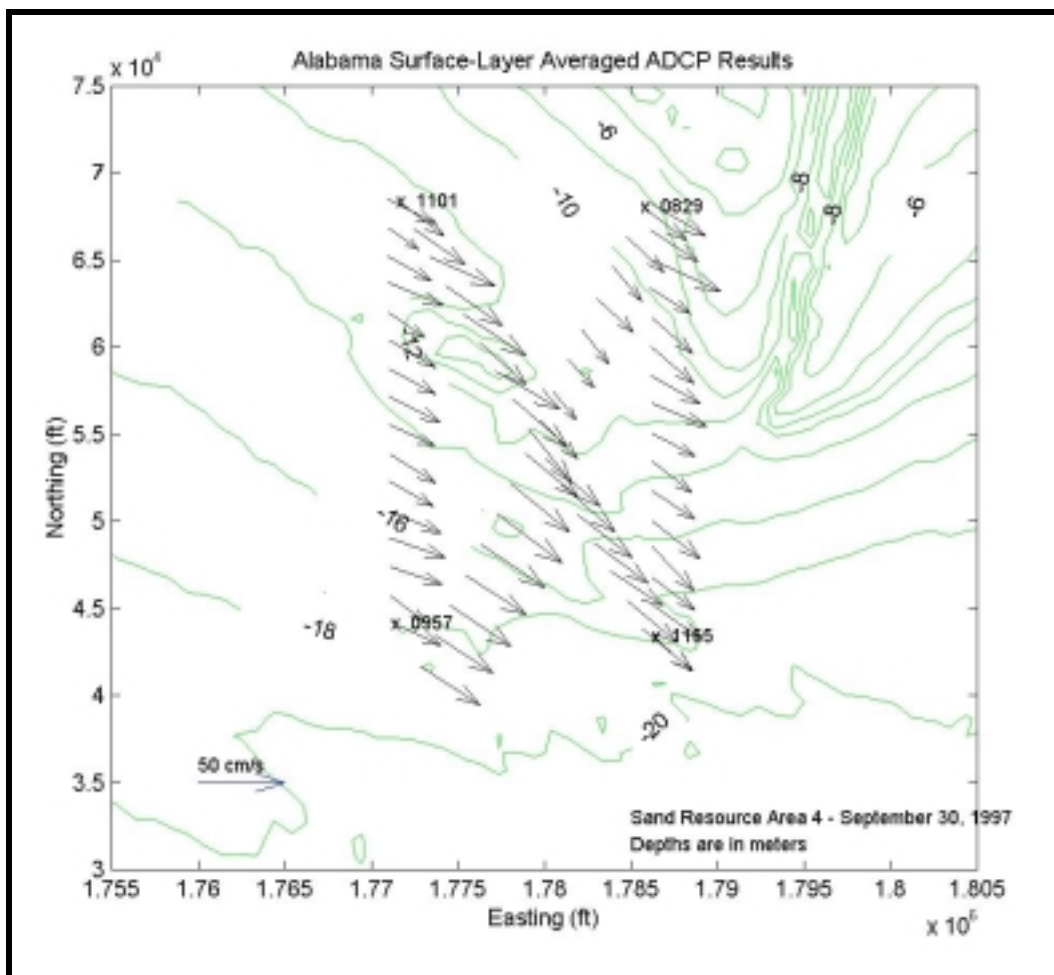

Figure 5-25. Vector map of observed flow patterns for Sand Resource Area 4; September 30, 1997 from 0829 hours to 1255 hours. Currents vectors represent average flow in the surface layer only (upper one-third of the water column).

Mid-layer flow had a similar southeast directional orientation, with speeds slightly reduced to approximately 25 to 35 cm/sec throughout the region. Bottom flow was weaker than overlying layers, with areas of low speed flow (approximately 15 cm/sec) and other areas where the speed was approximately 25 cm/sec (Figure 5-26). The weakest bottom currents appeared to be located on the down-current side of the dredged material mound; the strongest bottom currents were located in deeper water and those near the Main Channel. Bottom layer flow generally was oriented to the east, versus overlying flow to the southeast. This may be due to the presence of a surface plume discharged from the Bay, affecting more strongly the surface layers and hence deflecting surface currents weakly to the southeast. Meanwhile, bottom flow was relatively unaffected and free to follow the bottom contours.

Temporal changes in the flow field during the survey consisted of a slight weakening in surface current speed in the afternoon due likely to decreasing west winds (to approximately 6 kts versus 10 kts early in the day). The observed surface currents decreased from speeds of 40 to 50 cm/sec in the morning to speeds ranging from 20 to 30 cm/sec in the late afternoon. No directional changes were evident.
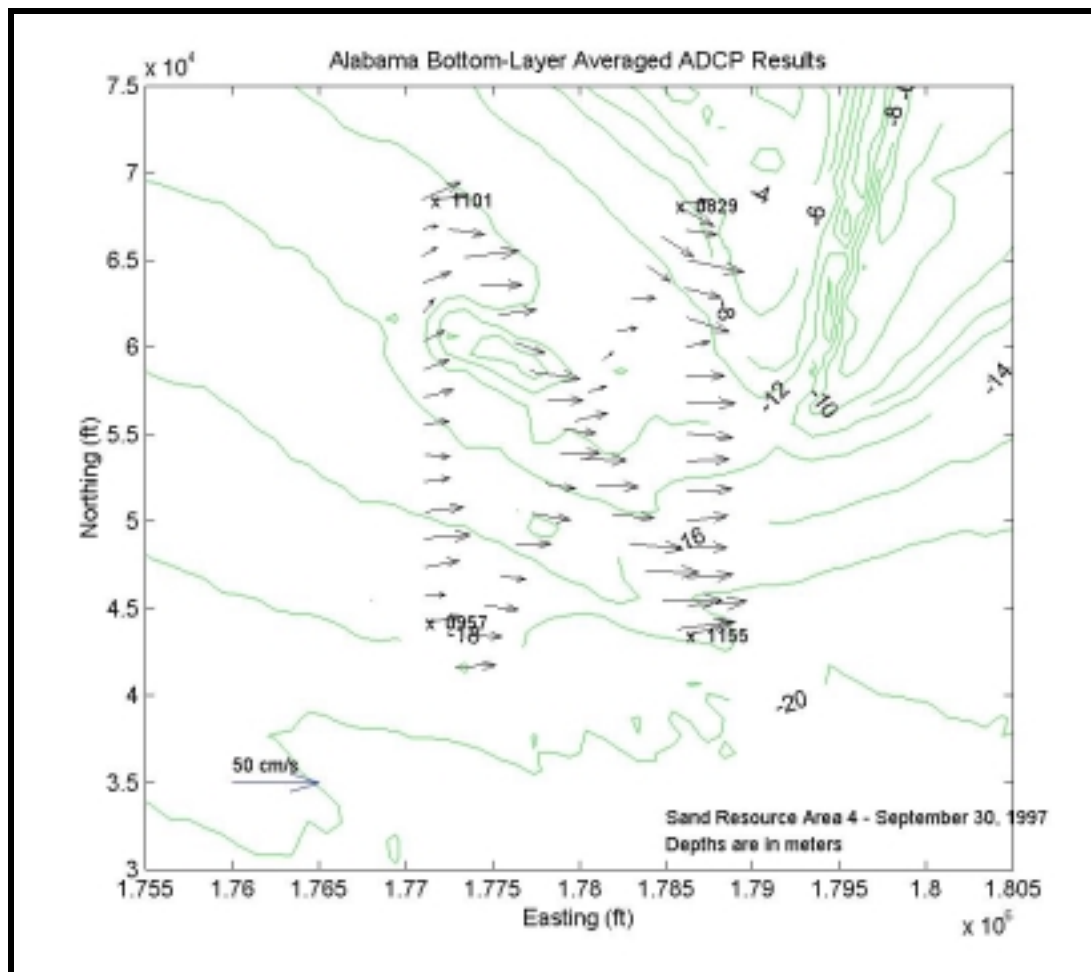

Figure 5-26. Vector map of observed flow patterns for Sand Resource Area 4; September 30, 1997 from 0829 hours to 1255 hours. Currents vectors represent average flow in the bottom layer only (lower one-third of the water column).

155

A slight modification of flow was observed later in the survey, likely due to weak ebb flow from Mobile Bay. The tide curve shows a decrease in water elevations in the afternoon, although this decrease was quite small (8 cm). Flow near Main Pass was observed to deflect slightly to the south, consistent with flow interaction between ambient west-to-east coastal currents and a southward discharge from the Bay entrance (Figure 5-27). This flow collision modified both surface currents as well as bottom currents. Flow along the bottom shifted southeast, versus an eastward flow earlier. Upper and middle layer flow was deflected to the south, versus an earlier southeast orientation.

Spatial Variability at Sand Resource Area 2

Currents throughout Area 2 were again quite uniform, meaning there was little directional variability observed at any one time. A slight clockwise rotation was observed during the survey, however the rotation appeared to be approximately 45° over the 12-hour period, and likely due to changes in the wind stress field.

No significant horizontal variation was observed in the surface layer, as the flow field was uniformly directed to the east or east-southeast (Figure 5-28). Speeds were relatively consistent and ranged from approximately 25 to 50 cm/sec. The mean speed at the surface was approximately 40 to 45 cm/sec. The relatively large range of observed current speeds at the surface indicates
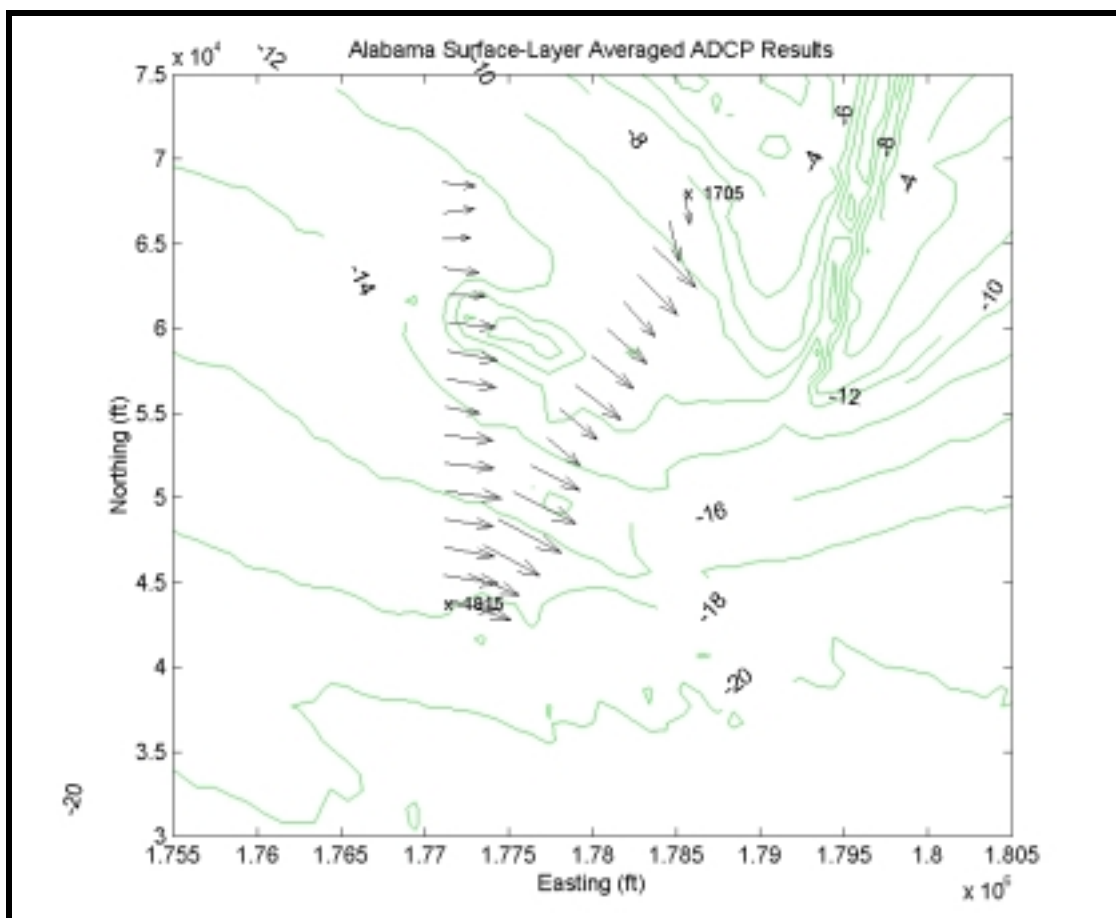

Figure 5-27. Vector map of observed flow patterns for Sand Resource Area 4; September 30, 1997 from 0829 hours to 1255 hours. Currents vectors represent average flow in the surface layer only (upper one-third of the water column).
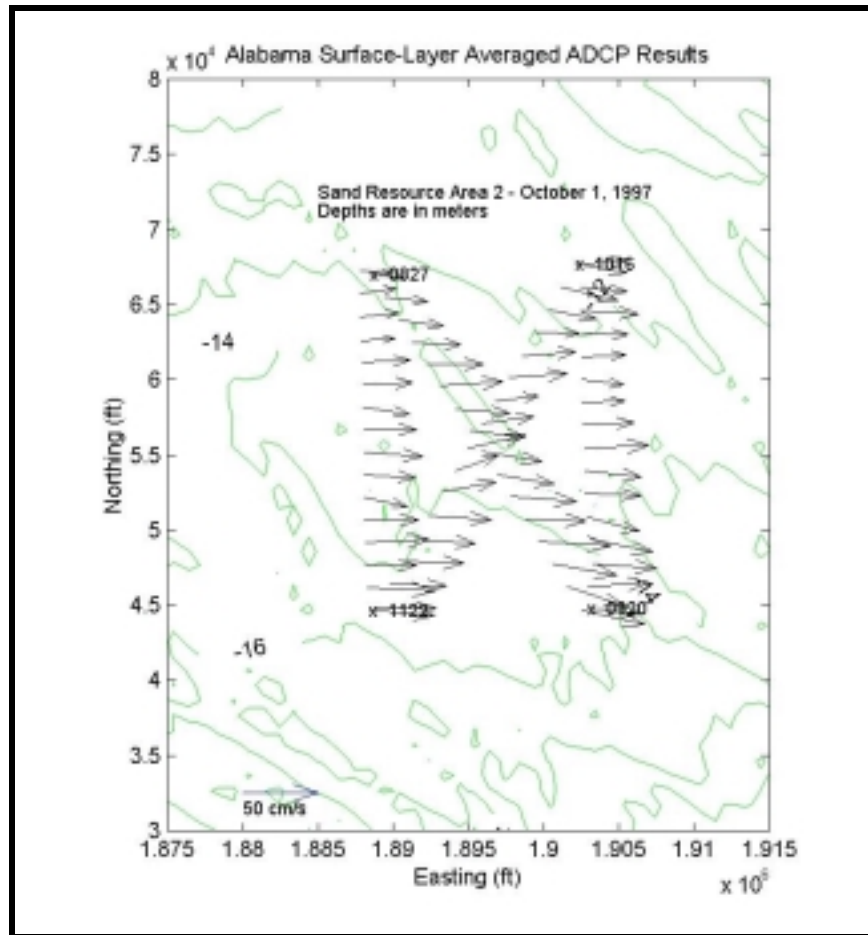
Figure 5-28. Vector map of observed flow patterns for Sand Resource Area 2; October 1, 1997 from 0827 hours to 1215 hours. Currents vectors represent average flow in the surface layer only (upper one-third of the water column).

a weakly turbulent flow regime. The mid-depth and near-bottom layers also exhibited this same uniformity, with all mid-depth currents flowing to the east-northeast. Speeds in this middle layer were approximately 15 to 40 cm/sec, with an average speed of approximately 30 cm/sec. Near-bottom currents showed slightly more directional variance, again due to the moderate influence of bathymetric relief; however, the currents generally pointed northeast. Mean speeds were approximately 20 cm/sec in the near-bottom layer, with a range from 10 to approximately 25 cm/sec (Figure 5-29).

The vertical variation in currents was much weaker than observed during the previous survey. In autumn, as river discharge abates, it is expected that the nearshore water column would lose vertical stratification and become more homogeneous with more efficient mixing between the surface and underlying layers. During the Fall survey, there was little difference between flows at the surface and near-bottom. A slight rotation was observed with depth; however, the rotation was counterclockwise to surface flows directed east and near-bottom flows directed to the northeast. This counterclockwise rotation may be the result of coastal upwelling. For a west wind producing a wind-driven flow to the east, there will be a slight cross-shore component produced to the right of the flow vector, or in this case, offshore. Bottom flow compensates for this offshore-directed transport to create a weak on-shore return component. The net result of this is an apparent counter-clockwise rotation of flow with increasing depth.
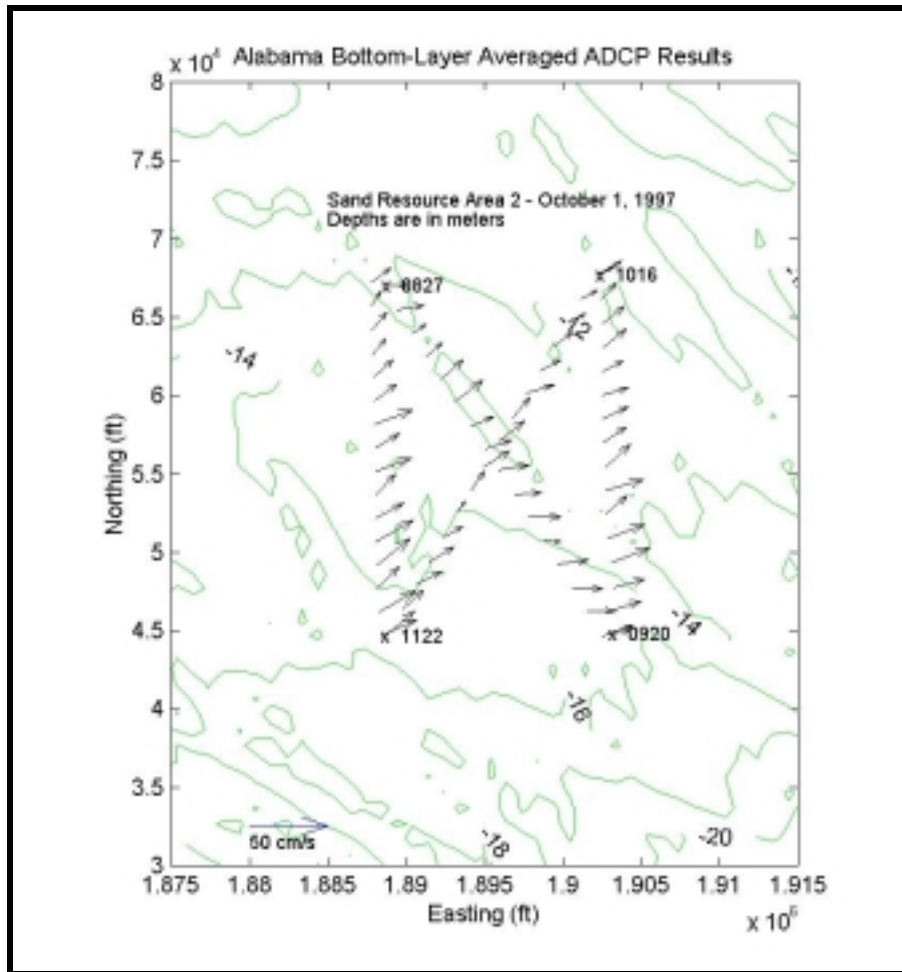
157

Figure 5-29. Vector map of observed flow patterns for Sand Resource Area 2; October 1, 1997 from 0827 hours to 1215 hours. Currents vectors represent average flow in the bottom layer only (lower one-third of the water column).

The flow field varied little throughout the survey, maintaining an approximate eastward direction with speeds ranging from 40 cm/sec at the surface to approximately 20 cm/sec in the near-bottom layer. During the 12-hour duration of the survey, a slight modification of near-surface current vectors was observed in response to a shift in the wind direction. This response to changes in wind stress was noticed initially in the surface layer; underlying layers appeared unaffected by this change, likely because the survey ended prior to the effects passing through the surface to underlying layers.

The response of the near-surface flow field to changes in wind stress is identified by a gradual shift in current direction from east-southeast and east, the predominant orientation of the flow during the early morning and afternoon, to the southeast later in the day. The shift in wind direction occurred at approximately 1500 hours. The first evidence of surface layer response was noted approximately two hours later at 1700 hours, when currents began deflecting southeasterly. This deflection of flow to the south appeared more consistently in shallower near-shore regions of the survey grid than in the deeper (offshore) regions of the area. There was also some evidence that surface flow vectors were decelerated by this deflection, with speeds measured in the range of 5 to 30 cm/sec (versus a range of 25 to 50 cm/sec early in the day, and a range of 15 to 45 cm/sec at mid-day).

158

5.1.3 Summary of Flow Regimes at Offshore Borrow Sites

The information presented above indicates the flow regimes within the study area are dependent upon wind forcing, density stratification, seafloor topography, and coastal boundaries. Tides had little influence on observed currents.

Historical data, in the form of long-term current observations at specific locations, were separated by time scales of individual physical processes: winds, tides, high-frequency currents, and low-frequency currents. For this analysis, it was clear that the observed currents at each location flowed predominantly in an alongshore direction. Wind-driven flow, defined as flow occurring at time scales between 1 and 15 days, had the greatest fraction of total signal energy. Wind distributes energy to the water column at a variety of time scales, from high-frequency bands (periods less than 24 hours) to low-frequency bands (periods greater than 15 days), so it must be assumed that some wind influence was included inherently in other separated signals as well. The separated low- and high-frequency signals also possessed significant energy, though not as great as the energy attributed to the defined wind-driven processes. These low- and high-frequency signals also appeared to be correlated to the strength of the wind.

Seasonal variation in currents also was correlated to seasonal changes in wind. Comparison of wind data in winter versus summer indicated the winter season was characterized by relatively strong northern winds, while the summer period was characterized by weak winds from the south. Generally, winter current speeds were shown to be greater than those observed in summer. Although wind directions varied considerably between seasons, the direction of the currents at these locations did not vary. The predominant alongshore orientation of currents at all sites did not change throughout the year.

The separation analysis also noted that tides have small influence on the overall observed currents. Tide accounts for less than 10% of the total signal energy. Tidal currents were greatest in the alongshore direction, as well as stronger at the surface than at the bottom. Tidal current speeds reached approximately 5 cm/sec (at the bottom) during tropic (maximum) phases and less than 1 cm/sec during equatorial phases; at the surface, maximum tidal speeds were approximately 8 cm/sec.

Results of the field surveys showed the spatial influence of bathymetric features, tidal exchange between Mobile Bay and the inner shelf, and the wind forcing on the nearshore circulation patterns. Wind conditions prior to and during both surveys had significant westerly longshore components. As a result, the prevailing currents flowed generally eastward, consistent with previous analyses. This wind-driven longshore flow was influenced locally by bathymetric features, specifically the ebb-tidal delta of Main Pass, which tended to steer longshore flow to the south, while flow in areas farther offshore, removed from this coastal boundary, did not have such strong deflections. At Area 2, east of Mobile Bay and in an area of gently sloping bathymetry with no abrupt features, the spatial variation of flow was small.

Survey data also illustrate the rapid response of surface flow to sudden changes in wind stress. During wind squalls on May 21, the surface flow field became quite variable just a few hours after wind gusts blew through the area. Also, on October 1, the surface flow regime was observed to respond rapidly to shifts in wind direction. This response occurred approximately two hours following a shift in the wind. This high-frequency response to changes in the wind field offers evidence that high-frequency signals, separated numerically from the original signal during the historical analysis, must be influenced by wind forcing as well. The directional distribution (rose diagrams) for this high-frequency component lacks the directional polarity of the wind-driven (1 to 15 day) signal, suggesting that sudden changes in wind direction result in flow in the same direction.

However, comparison of the spring and fall surveys revealed some distinctions, the most obvious difference was the vertical structure of the water column and the resulting effect of this

vertical stratification on the current field. In May, especially at Area 2, the water column appeared strongly stratified, due mostly to eastward advection of the freshwater plume discharged from Mobile Bay. Circulation was modified by vertical stratification with the surface appearing to respond strongly to localized wind stress. The underlying layers had little direct response to these sudden changes. In October, when freshwater discharge from the Mobile Bay estuary is generally smaller than discharges during the spring, there was little evidence of a stratified water column. Flow at the surface had similar characteristics as flow along the bottom. There seemed to be some dependence of the near-bottom flows on overlying near-surface flow. The lack of a stratified water column in October suggests that the freshwater plume had smaller influence on circulation dynamics during this season.

Tidal conditions were also quite different during the two surveys. In May, tides were in the tropic phase, at or near the largest range of elevations (approximately 0.45 m). In October, tides were in the equatorial phase, or the minimum range of the tide, and the water elevation changes during the survey were less than 15 cm. Tides were identified in the historical analysis to be a small contributor to the overall circulation dynamic in this region; however, during the May survey in Area 2, a significant clockwise rotation was observed which dominated current direction variations. This rotation may have been tidal in origin, although the magnitude of the currents suggest other processes (possibly baroclinic). In October, when small water elevation changes were observed (as well as weak vertical stratification), no such rotational phenomena was observed. During the spring survey at Area 4, tidal currents were observed briefly along the bottom during flood tide, as denser shelf water entered the Bay during the rising tide. This suggests that tides, while generally of lesser importance than wind effects, may have localized and transient importance, such as during tropic tide phases when freshwater discharge is significant. At these times (tropic flood tides in springtime when discharge is high), tidal currents flooding into Mobile Bay may be relatively strong, with magnitudes of order 15 to 25 cm/sec, versus more prevalent tidal currents of approximately 5 cm/sec.

5.1.4 Wave-Induced Bottom Currents

A propagating wave not only causes a displacement in the water surface, but also displaces water particles beneath the passing wave. This displacement induces local currents, which over the period of the passing wave take on an orbital shape (orbital velocities). In shallow water, the orbits of water particles tend to take on an elliptical shape, while in deeper water the orbits are more circular (Figure 5-30). Associated with these water particle trajectories are the particle horizontal (u_{orbit}) and vertical (w_{orbit}) orbital velocity components. These velocity components contribute to the initiation and transport of sediment at the seabed. Therefore, knowledge of orbital velocities at the seabed is a key parameter for determining sediment transport characteristics at potential offshore borrow areas. This section describes the method used to calculate wave-induced orbital velocities at the seabed.
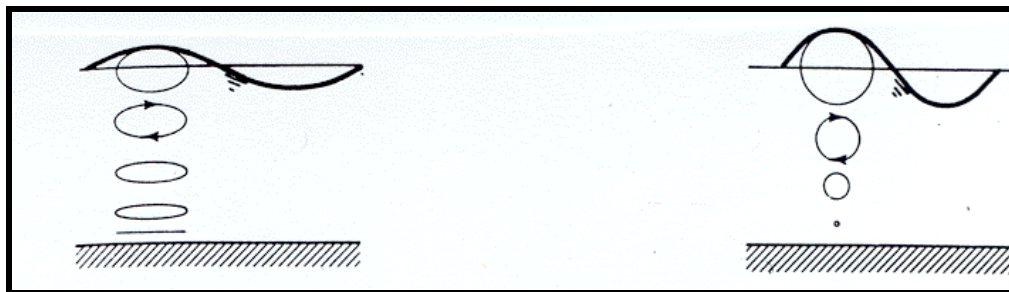

Figure 5-30. Shallow water and deep water wave orbits.

The relationship between a progressive wave and the particle motion it generates beneath the surface is well described by linear wave theory. Linear wave theory is used to derive the expression of the velocity potential (ϕ) as:

$$\phi = -\frac{Hg}{2\sigma}\frac{\cosh k\,(h+z)}{\cosh\,(k\,h)}\cos\left(k\,x\right)\sin\left(\sigma\,t\right)$$ (5.1)

where H is the wave height; σ is the wave frequency; k is the wave number; h is the still water depth; z is the point of interest in the water column (positive upwards from still water); x is the horizontal point of interest along the wave, g is the gravitational constant, and t is the temporal point of interest. The resulting horizontal and vertical velocities under the wave are given by:

$$u_{orbit} = \frac{-\partial\phi}{\partial x} = \frac{H}{2}\sigma\frac{\cosh k(h+z)}{\sinh\left(kh\right)}\cos\left(k\,x - \sigma\,t\right)$$ (5.2)

$$w_{orbit} = \frac{-\partial\phi}{\partial z} = \frac{H}{2}\sigma\frac{\sinh k(h+z)}{\sinh\left(kh\right)}\sin\left(k\,x - \sigma\,t\right)$$ (5.3)

Equations (5.2) and (5.3) reveal that the velocity at the bottom (z = -h) consists only of the u_{orbit} component, while w_{orbit} is zero. Thus, at the seabed, the motion of the water particles is purely horizontal (assuming the water cannot penetrate the seabed). This allows the reduction of the velocity at the bottom to:

$$U_B = \frac{H}{2}\frac{\sigma}{\sinh\left(k\,h\right)}$$ (5.4)

The horizontal motion, as the seabed oscillates positively (under a crest) and negatively (under a trough), depends on the spatial and temporal position of the wave (Figure 5-31). Therefore, the absolute maximum bottom currents induced by the wave occur at the crest and/or the trough of the passing wave.
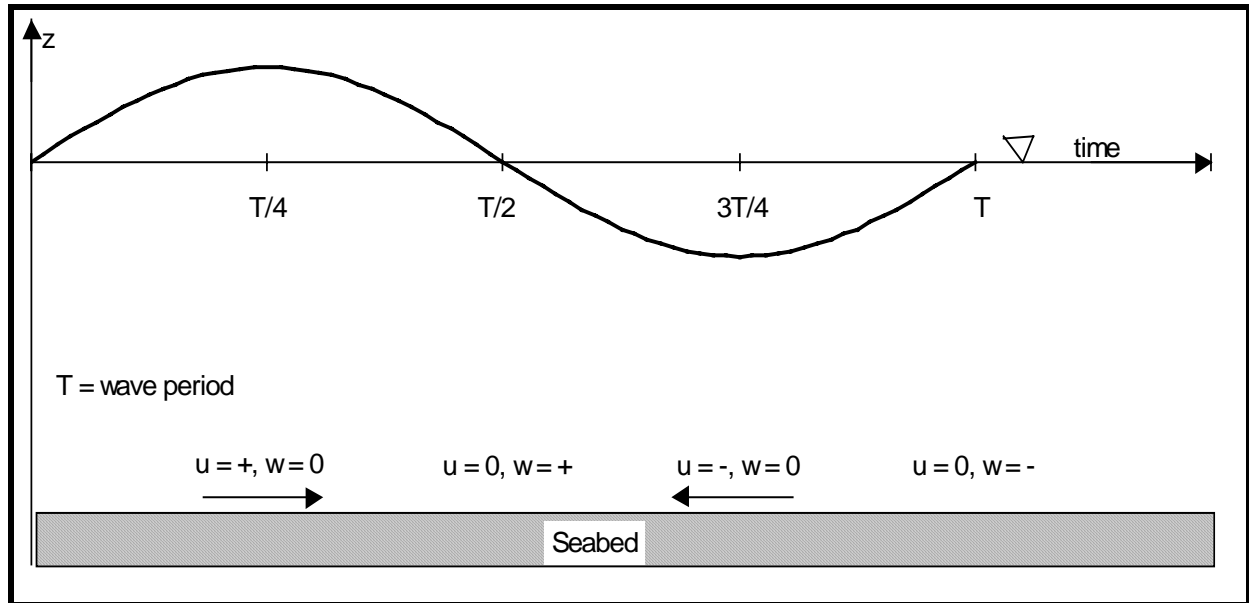

Figure 5-31. Schematic of wave-induced bottom velocities.

Applying linear wave theory, coupled with the wave model results at the dredged borrow areas, wave-generated bottom currents can be determined. Wave height, wave period, wave

direction, and water depth are extracted from the wave model at each of the designated borrow areas (and for each season/event scenario) and used to calculate the maximum bottom horizontal orbital velocity at the seafloor for each grid point within the selected domain. Wave-induced bottom velocities can then be combined with ambient currents and utilized to determine sediment initiation and potential transport at the offshore borrow sites.

The wave-induced bottom velocity is a key factor contributing to the initiation and transport of sediment. Although for purely sinusoidal motion, no net sediment transport is caused by the orbital motions, shearing velocities created at the seabed by the waves are a primary contributor to the initialization of sediment into the water column (Fredsoe and Deigaard, 1992).

5.1.5 Wave-Induced Longshore Currents

In addition to orbital velocities generated beneath a propagating wave, longshore currents are generated in the nearshore zone (generally landward of the breaker line) by waves approaching obliquely to the coast. This longshore current is the primary advective force generating littoral drift along the beach. Several models have been developed that take simplified information from monochromatic wave models to develop empirical or semi-empirical relationships between calculated wave information and longshore sediment transport rate. However, the use of REF/DIF S allowed development of a sediment transport model based on spectral wave parameters. As part of the output, REF/DIF S calculates radiation stress values (S_{xx}, S_{xy}, and S_{yy}) at each model grid cell for the entire spectra. Therefore, a single set for radiation stress values at each grid cell provides the basis of sediment transport analyses. The methodology requires a two-part procedure: wave-induced currents were developed following the work of Ebersole and Dalrymple (1980), and the cross-shore distribution of currents was utilized to generate local longshore sediment transport rates based on the work of Bodge (1986).

The governing equations of the wave-induced current model are the depth-averaged continuity equation and the depth-averaged x and y direction momentum equations. All of these equations are developed by integrating the standard form of the equations over the depth of the water column and then time averaging the results. Previous work incorporating this methodology includes Birkemeier and Dalrymple (1976), Ebersole and Dalrymple (1979), Yan (1987), Winer (1988), and Ramsey (1991).

Due to the inherent complexities of wave-induced current formation in the surf zone, certain assumptions are required in the derivation of governing equations for the wave-induced current model. A primary simplification is that the flow field may be represented in two dimensions by depth and time averaging the equations. Therefore, the vertical variation in the velocity profile is lost. The advantage of depth averaging the equations is to reduce the complicated three-dimensional problem to a more tractable two-dimensional one. However, some details of the flow field may be missed by only considering horizontal flow.

5.1.5.1 Governing Equations

The form of the continuity equation used in this model assumes that the water density is constant and can be represented by:

$$\frac{\partial \bar{\eta}}{\partial t} + \frac{\partial}{\partial x}(UD) + \frac{\partial}{\partial y}(VD) = 0 \tag{5.5}$$

where

    U = the x component of the mean current
    V = the y component of the mean current

$\overline{\eta}$ = the mean water surface elevation

D = the total water depth $(h + \overline{\eta})$

h = the local still water depth

The continuity equation represents the conservation of mass per unit surface area under the assumption that the water density does not change with depth or time. Although seasonal temperature variations may affect water density, the influence of density variability on wave-induced current velocities within the surf zone can be considered negligible.

The horizontal depth-averaged momentum equations were originally derived by Phillips (1969) and for the purpose of the wave-induced current model take the form:

$$\frac{\partial}{\partial t}(UD) + \frac{\partial}{\partial x}(U^2 D) + \frac{\partial}{\partial y}(UVD) = -gD\frac{\partial \overline{\eta}}{\partial x} - \frac{D}{\rho}\frac{\partial \overline{\tau\iota}}{\partial y}$$
$$-\frac{1}{\rho}\frac{\partial S_{xy}}{\partial y} - \frac{1}{\rho}\frac{\partial S_{xx}}{\partial x} + \frac{1}{\rho}\tau_{sx} - \frac{1}{\rho}\tau_{bx}$$

(5.6)

and

$$\frac{\partial}{\partial t}(VD) + \frac{\partial}{\partial x}(UVD) + \frac{\partial}{\partial y}(V^2 D) = -gD\frac{\partial \overline{\eta}}{\partial x} - \frac{D}{\rho}\frac{\partial \overline{\tau\iota}}{\partial x}$$
$$-\frac{1}{\rho}\frac{\partial S_{xy}}{\partial x} - \frac{1}{\rho}\frac{\partial S_{yy}}{\partial y} + \frac{1}{\rho}\tau_{sy} - \frac{1}{\rho}\tau_{by}$$

(5.7)

for the *x* and *y* direction, respectively, where

U = *x* component of mean current
V = *y* component of mean current
$\overline{\eta}$ = mean water surface elevation
D = total water depth
ρ = water density
$\tau\iota$ = lateral stress due to turbulent mixing
τ_{bx} = *x* component of bottom shear stress
τ_{by} = *y* component of bottom shear stress
τ_{sx} = *x* component of surface shear stress
τ_{sy} = *y* component of surface shear stress.

Many of the terms in the depth-averaged momentum equations require certain empirical guidelines to compute their values. The theory governing bottom friction and lateral mixing are not completely understood and, therefore, need empirical formulations or scaling arguments to estimate their values.

First, the bottom shear stress typically is based on some type of drag coefficient and can be expressed as:

$$\tau_{bi} = \rho f \overline{u_{ti}|u_t|}$$

(5.8)

where u_t is composed of the mean current and the wave orbital velocity, u_{ti} is its component form (either in the *x* or *y* direction), and the overbar indicates time averaging over one wave period. The

empirical friction factor is represented by *f*. The magnitude of the total velocity, expressed as $\left|u_t\right|$, is equal to $\sqrt{u^2+v^2}$ where the *u* and *v* velocity components are

$$u = U + u_{xw} = U + u_w \cos\theta \tag{5.9}$$

$$v = V + u_{yw} = V + u_w \sin\theta \tag{5.10}$$

U and *V* are the mean current speeds defined previously. The wave orbital velocities in the *x* and *y* direction are u_{xw} and u_{yw}, respectively, where $u_w = \sqrt{u_{xw}^2 + u_{yw}^2}$. The total velocity can then be expressed as

$$\left|u_t\right| = \sqrt{U^2 = V^2 = u_w^2 = 2Uu_w \cos\theta = 2Vu_w \sin\theta} \tag{5.11}$$

The wave orbital velocity exhibits oscillatory behavior which may be expressed as

$$u_w = u_{max} \cos\sigma t \tag{5.12}$$

where u_{max} is the maximum orbital velocity at the bottom which can be written as

$$u_{max} = \frac{\sigma|a|}{\sinh kh} \tag{5.13}$$

For numerical efficiency, a simplified model that includes wave orbital velocities and a strong current assumption may be formulated as

$$\tau_{bi} = pf\left|u_t'\right|U_i \tag{5.14}$$

where

$$\left|u_t'\right| = \sqrt{U^2 + V^2} + u_{max} \tag{5.15}$$

This equation implies that there is no interaction between the wave orbital velocity and the mean current velocity. The equations for *x* and *y* components may be expressed as

$$\tau_{bx} = pf\left|u_t'\right|U \tag{5.16}$$

and

$$\tau_{by} = pf\left|u_t'\right|V \tag{5.17}$$

This simplification allows calculation of bottom shear stresses without the computational demands of full integral equations. Increasing the friction factor may offset any differences between this approach and the more complete integral equations. The selection of a proper value for the friction factor is very important in modeling currents and will be discussed in Section 5.1.5.3.

5.1.5.2 Lateral Mixing

Longshore currents vary with distance offshore, where strongest currents typically are found near the wave break point. If the wave-induced current model did not include cross-shore mixing, the predicted longshore velocity profile would change abruptly to zero at the breaker line as shown in Figure 5-32. To simulate the effect of turbulent mixing in the surf zone, some type of cross-shore mixing within the velocity profile is required. In addition, longshore mixing may be required if morphologic controls (e.g. shore perpendicular channels or shoals in the surf zone) or groins create rip currents. Since this application of the wave-induced current model for the Alabama coast

involves a sandy coast with no major shore protection structures, the focus of lateral mixing only involves the cross-shore direction.

Harris et al. (1963) were the first to conduct field and laboratory studies to measure the intensity of mixing within the surf-zone. Their work involved releasing known amounts of tracer in the nearshore region and calculating the strength of mixing based on measured concentration of the tracer at a later time. Qualitative results indicated that the tracer dispersed rapidly in the on/offshore direction and that, in the absence of rip currents, cross-shore mixing was confined mainly to the surf zone. In addition, they noted that mixing in the longshore direction was largely due to advection of the dye by the longshore current.
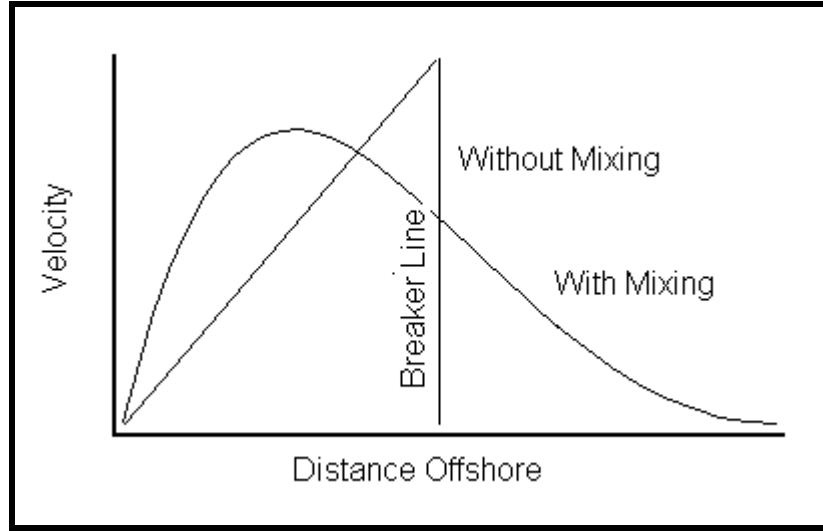

Figure 5-32. Schematic longshore velocity profiles with and without cross-shore mixing (the abrupt reduction in velocity for the without mixing case occurs at the breaker line).

Longuet-Higgins (1970) used the two depth integrated equations of motion which assumed that the turbulent fluctuation term, $\overline{-\rho u'v'}$, is independent of depth to derive a different equation for cross-shore mixing. Another major assumption required in the derivation was that the momentum transfer due to turbulent fluctuations may be represented as a product of the mixing length coefficients (ε_χ, ε_y) and derivatives of the mean current. In equation form, this can be expressed as

$$\tau_t = -\rho\left(\varepsilon_y\frac{\partial U}{\partial y} + \varepsilon_x\frac{\partial V}{\partial x}\right) \tag{5.18}$$

Longuet-Higgins made additional assumptions regarding horizontal mixing in the surf-zone based on the horizontal eddy viscosity coefficient, ε_χ. Since the turbulent eddies responsible for lateral mixing must be smaller than the distance from an arbitrary point to the shoreline, it follows that ε_χ must tend to zero as the shoreline is approached. However, the decrease in ε_χ, between the breakerline and the shoreline is not necessarily linear. The approach adopted by Longuet-Higgins was to assume that ε_χ is proportional to the offshore distance, x, multiplied by a typical shallow water wave celerity, $\sqrt{gh}$. When the bottom slope is uniform, a simple equation governs the longshore current profile. Although beach profiles in nature are not uniform, the simplified approach provides a reasonable method for determining an appropriate mixing coefficient. Expressing the cross-shore mixing coefficient as

165

$$\varepsilon_x = Nx\sqrt{gh} \tag{5.19}$$

and using a number of scaling arguments for the variables, the probable limits for the constant N were found to be $0 < N < 0.016$.

This equation or some slight modification has become the standard formula for calculating mixing in longshore current models. Seaward of the plunge line, ε_χ is kept at the maximum value. Since there is little turbulence seaward of the plunge line, the high value of the mixing coefficient ensures that there is a reasonable amount of lateral mixing in the cross-shore direction. For the spectral wave model, much of the cross-shore mixing is represented by gradual breaking of waves, where longer wave components break further from shore. This representation of a wave breaking envelope tends to distribute longshore currents in a manner similar to the with mixing case shown in Figure 5-32. Therefore, significant redistribution of longshore currents using the above methodology was not necessary, and values for the cross-shore mixing coefficient were minimized.

5.1.5.3 Model Verification

Because the primary purpose for calculating the cross-shore distribution of the longshore current was to calculate the littoral drift rate, model validation to field experiments was required to gauge computational accuracy. The model was verified using the field data sets of Kraus and Sasaki (1979) and Thornton and Guza (1989). These data represented a broad range of field conditions, with wave periods ranging from 4.1 to 12.8 sec. Kraus and Larson (1991) used both data sets to verify the one-dimensional longshore current model, NMLONG. Unfortunately, these field test cases provide only cross-shore variation in the longshore current. No two-dimensional field data sets were found for model verification. Several laboratory experiments have been performed to evaluate two-dimensional wave-induced current fields, including currents near groins (Winer, 1988) and shore parallel breakwaters (Ramsey, 1991).

For the field cases modeled, radiation stresses were calculated based on the results of a monochromatic wave refraction model designed to estimate wave heights and directions within the nearshore region. Since this wave model over-simplified nearshore wave conditions, limited wave-induced current model verification was anticipated. However, results of the current model compared favorably with both data sets. In addition, the modeled longshore current distribution was similar to those predicted by the NMLONG model.

Kraus and Sasaki (1979) measured the longshore current profile along seven transects on a sandy beach facing the Sea of Japan. Current measurements were made simultaneously along each transect by divers positioned at 5 m intervals. The current was measured by timing the migration of neutrally buoyant floats located at about mid-depth. An average current velocity was computed based on three successive measurements along each transect. Field observations during the field experiment indicated the waves arrived as clean swell, with a significant wave height of 1.0 m, a period of 4.1 sec, and a angle at breaking of 9 degrees relative to the shoreline.

A comparison of field experiment results and wave-induced current model output used in this study is shown in Figure 5-33. Due to the relatively steep waves, two significant peaks of longshore current velocity were computed by the model: one peak just landward of the observed breaker line (about 40 m offshore) and one peak adjacent to the shoreline. This increase in current strength near the swash zone is typical of steep wave conditions (Bodge, 1986). The results from two different model runs are shown, with the friction factor ranging between 0.0025 and 0.0030. Both the magnitude and offshore position of the maximum longshore current compare well with field data. In addition, the modeled prediction of current strengths seaward of the breaker line closely matched the data. However, the modeled current magnitude was under-predicted relative to field measurements.
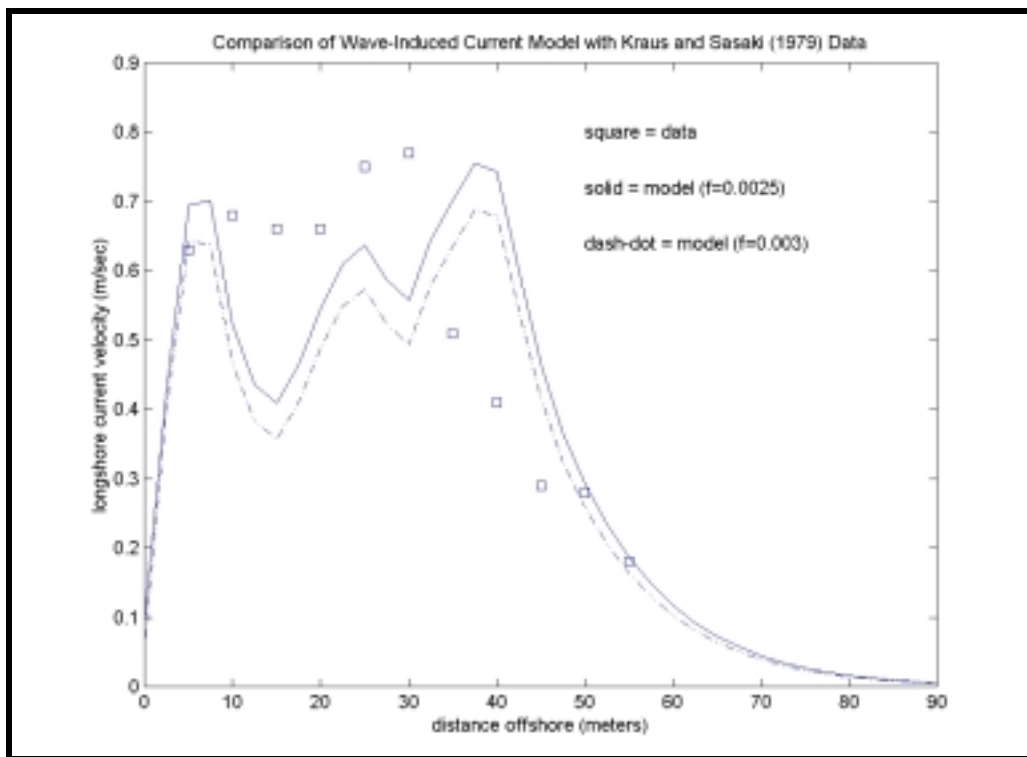
Figure 5-33. Comparison of model and observed longshore current velocities from field measurements taken by Kraus and Sasaki (1979).

To further verify the applicability of the wave-induced current model, wave and longshore current data from Thornton and Guza (1989) were utilized. The data were collected at Leadbetter Beach, California at a location where nearshore contours were relatively straight and parallel. Although four cases were presented in the initial work, only the February 5th Case was used for comparison with the wave model. Wave conditions for this case were a root-mean-square wave height of 0.45 m, a wave period of 12.8 sec, and an angle at breaking of 8.4 degrees relative to the shoreline.

A comparison of field data and wave-induced current model output is shown in Figure 5-34. The results from three different model runs are shown, with the friction factor ranging between values of 0.002 and 0.004. This range of friction values is similar to those employed by Kraus and Larson (1991). The magnitude of the maximum longshore current compares well with field data; however, the model predicted the location of the peak current much closer to the shoreline than the data indicated. In this case, use of a monochromatic wave model to generate radiation stresses for the wave-induced current model effectively eliminated cross-shore mixing associated with various spectral components.
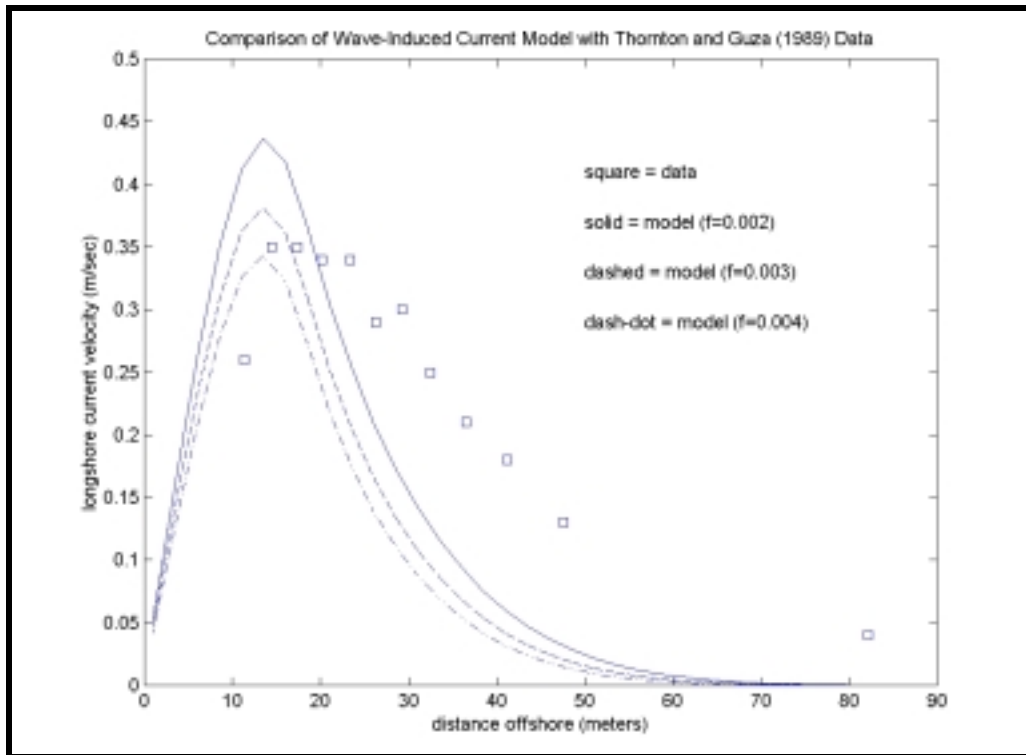
Figure 5-34. Comparison of modeled to observed longshore current velocities from field measurements taken by Thornton and Guza (1989).

5.1.5.4 Wave-Induced Currents Along the Alabama Coast

Model verification provided confidence that the wave-induced current model could be used to effectively evaluate longshore currents as the basis for littoral drift prediction. A sensitivity analysis was performed to determine appropriate values for the friction coefficient. Based on the verification runs, as well as previous work by Ramsey (1991), the appropriate value of *f* was determined to be 0.003. This value was utilized for all model runs associated with the Alabama study.

Because the results of the wave-induced current model are merely an intermediary step in the calculation of longshore sediment transport, only sample results from the current model are presented in this report. The wave-induced current model was run for the Dauphin Island and Morgan Peninsula wave modeling grids, for each spectral wave condition (total of five), and for both existing conditions and post-dredging scenarios. This required a total of 20 model runs. The results of one run (the existing conditions at Morgan Peninsula for the spring wave conditions) are described in more detail below. This example provides an overview of typical wave-induced current predictions associated with the modeling effort.

First, radiation stress in the longshore direction across a shore perpendicular transect is denoted as S_{xy}. Although the combined effects of the other two radiation stress components (S_{xy}, S_{xy}) are important to the two-dimensional current regime, S_{xy} provides the primary driving force for longshore currents. As waves reach the break point, it is the variation in S_{xy} across the surf zone that induces longshore current motion. Therefore, Figure 5-35 illustrates the longshore and cross-shore distribution of S_{xy}, indicating regions of longshore energy focus. As expected, areas of higher S_{xy} values have higher maximum current velocities.
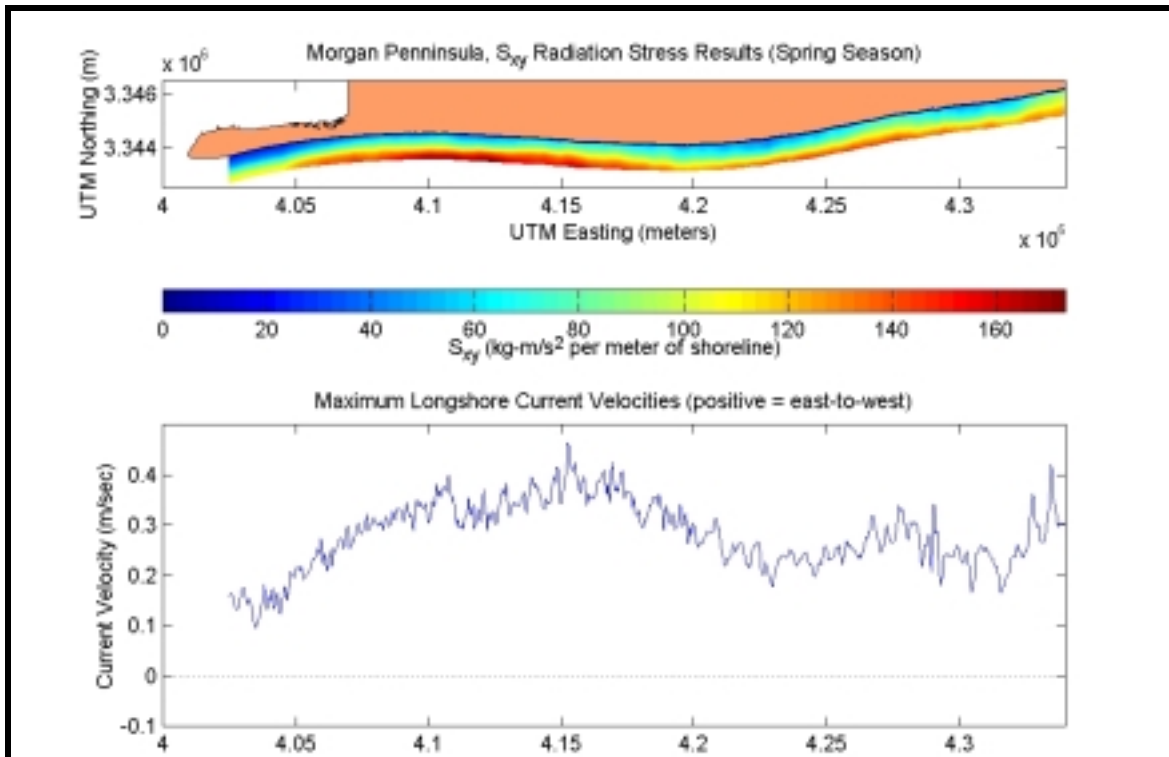
168

Figure 5-35. S_{xy} radiation stress and maximum longshore current velocities predicted by the wave-induced current model for the Morgan Peninsula during the spring season.

Cross-shore variability of the longshore current also can impact the volume of longshore sediment transport. Areas with relatively wide surf zones may exhibit low maximum longshore current velocities; however, currents exist over a larger area on these beaches and if the currents are strong enough to mobilize sediment, longshore transport rates can be higher than beaches with higher maximum currents. Along much of the Morgan Peninsula, beach slope is consistent and steep; therefore, the maximum current strengths shown on Figure 5-35 directly reflect the transport trends along this stretch of beach. Figure 5-36 provides several longshore current profiles indicating the variability of currents along the Morgan Peninsula shoreline. Although there is some variability in profile shape along the Morgan Peninsula shoreline, longshore current velocities become negligible within 60 m of the shoreline at all locations. The surf zone width appears to be slightly wider near the eastern end of the project area, likely due to larger wave heights in this region. For the Spring season, maximum longshore current speeds vary by more than 50%, ranging from approximately 0.1 to 0.4 meters per second. Although not a direct link, the longshore variation in maximum current is an indication of longshore sediment transport trends. Typically, areas with greater wave-induced current velocities will have a higher longshore sediment transport potential. A detailed analysis of longshore sediment transport potential is provided in Section 5.2.2.

Because the wave-induced current analysis was an intermediary step between wave transformation modeling and longshore sediment transport modeling, detailed results for each seasonal or extremal cases have not been provided. As described above, variations in longshore currents were similar to trends depicted in nearshore sediment transport modeling described in Section 5.2.2.
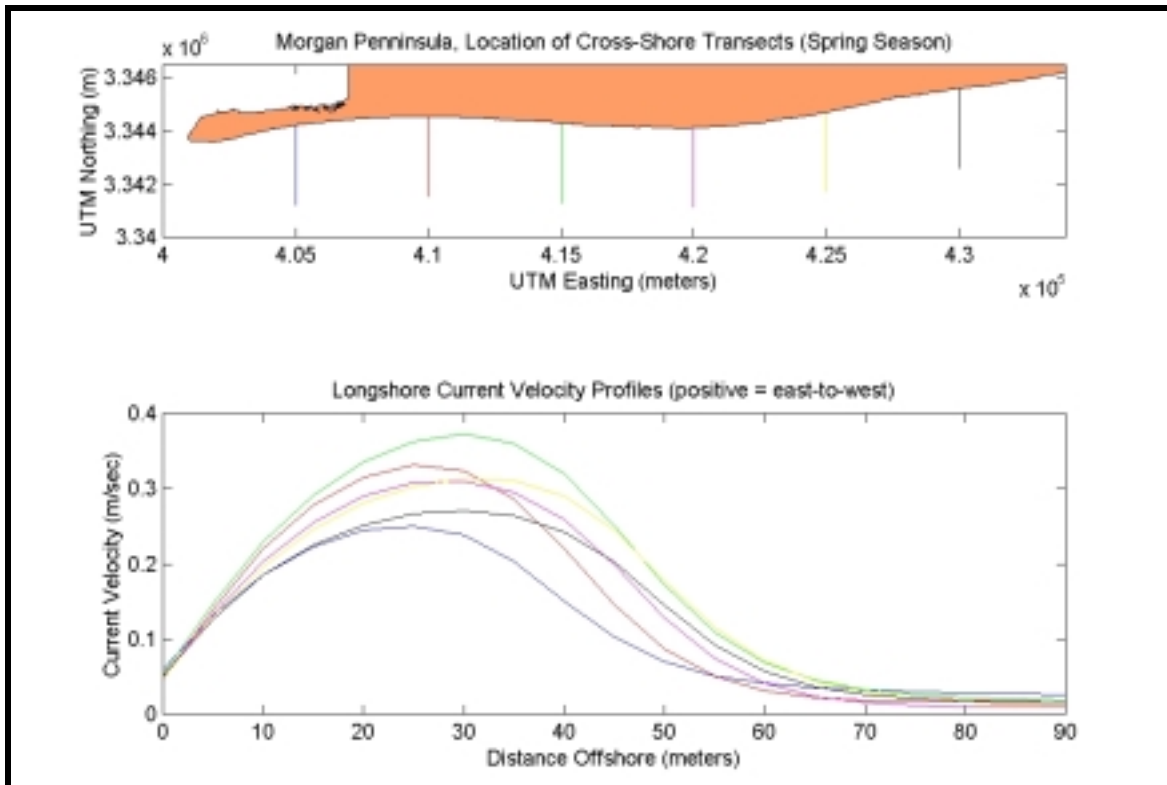
Figure 5-36. Longshore current profiles along selected transects at Morgan Peninsula (colored transects in the top sub-plot correspond to like colored profiles in the bottom sub-plot).

5.2 SEDIMENT TRANSPORT MODELING

5.2.1 Sediment Transport at Borrow Sites

Potential sand mining activities at offshore borrow areas may lead to changes in sediment transport mechanics occurring at or near proposed offshore dredging locations. The purpose of this section is to identify the approximate quantity and direction of sediment transport at potential borrow sites and estimate the duration for infilling of borrow areas. Spectral wave model results, along with historical and measured current observations, were employed for the analysis of sand transport at borrow sites. This section examines the interaction of wave-induced bottom orbital velocities and ambient currents, the initiation of sediment motion at potential borrow areas, and the relative magnitude and direction of sediment transport.

5.2.1.1 Initiation of Sediment Motion Under Combined Wave and Current Action

Assuming purely oscillatory wave motion (linear theory) without currents results in no net sediment transport at offshore borrow areas. Even if sediment is lifted from a non-sloping seafloor into the water column, the amount of sediment transported forward (in the direction of wave propagation) during half of the cycle will equal the amount being transported backwards during the other half of the cycle under linear waves. In order to cause a net difference in sediment transport, additional physical phenomena are required. These include:

- bottom slopes on the seafloor
- tidal and/or wind-driven currents
- wave asymmetry (non-linearity)
- wave-induced mass transport

170

In areas outside the surfzone, it is critical to account for wave and current interactions inside the bottom boundary layer when evaluating potential sediment transport. Introducing coastal currents to wave motions adds difficulty in estimating shear, dissipation, and sediment transport dynamics. A number of approaches have been developed by Lundgren (1972), Bakker (1974), Smith (1977), and Bakker and van Doorn (1978) to attempt to solve this problem.

Only Madsen and Grant (1976, 1977), Grant and Madsen (1978, 1979) and Tanaka and Shuto (1981), considered current and wave interaction situations, where the current and wave have an arbitrary angle with each other. Tanaka and Shuto used a one-layer eddy viscosity approach, which most likely over simplified the problem. Madsen and Grant (1976, 1977), and Grant and Madsen (1978, 1979) derived sediment transport relationships for predicting net sediment transport rates in the presence of second order effects such as bottom slope, wave asymmetry, coastal currents, and mass transport currents. They concluded that only cases involving small amplitude wave theory and a steady current are understood to a level that it is reasonable to evaluate resulting sediment transport rates with any degree of confidence. Fortunately, this is the situation for offshore Alabama, including the potential offshore borrow areas.

Before sediment can be transported, it must be moved from the seabed by combined wave and current motion. When sufficient stress is applied to the bed, sediment may begin to move. Typically, a mild steady flow over a bed of cohesionless grains will not result in sediment transport (Fredsoe and Deigaard, 1992). However, when subjected to a large enough flow, the driving forces impacting sediment grains exceed the stabilizing forces, and sediment will begin to move.

Through dimensional analysis, Shields (1936) derived an expression that identifies the point where bed stress equals bed resistance. The threshold of particle motion is based on a ratio between the driving forces (drag and lifting forces) and stabilizing forces (frictional forces) as seen in Figure 5-37. The Shields parameter (Ψ) results from equating the driving and stabilizing forces. For a flat bed:

$$\psi = \frac{\tau_b}{(s-1)\,\rho g\,d_{50}}$$ (5.20)

where
τ_b = maximum bottom shear stress
ρ = density of the sea water
s = relative density (equals 2.65 for natural sediment)
g = acceleration due to gravity
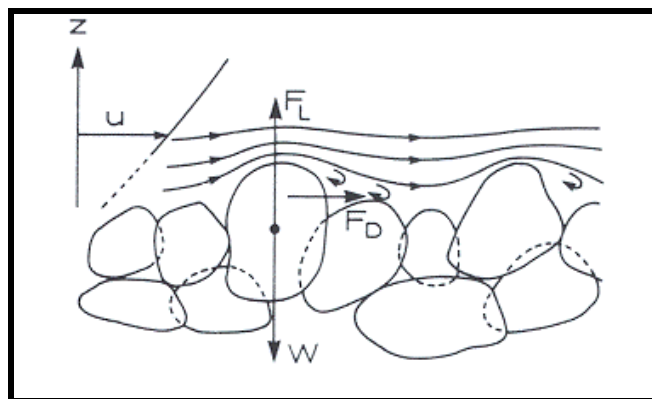d_{50} = grain diameter which corresponds to 50% by weight finer

Figure 5-37. Forces acting on grains resting on the seabed (Fredsoe and Deigaard, 1992). F_L = lifting force, F_D = drag force, and W = grain weight.

The shear stress at the bed, τ_b, is given by Madsen and Grant (1976) and Raudkivi (1990) as:

$$\tau_b = \frac{1}{2}\rho f_{cw}|u_{cw}|u_{cw} \tag{5.21}$$

where f_{cw} is the combined wave/current friction factor and u_{cw} is the combined wave/current reference velocity.

In this study, u_{cw} includes the effects of waves and a steady current. A combination of the two creates a more realistic representation of maximum bottom velocity and bed shear stress. Proper combination of wave-induced and ambient currents requires an accurate representation of flow dynamics located directly at the seabed. In most cases, it is difficult to measure ambient current magnitude and direction directly at the seafloor. In the present study, historical current observations were measured a certain distance from the bottom. For example, current data used to derive the current field at Sand Resource Area 4 were sampled at a distance of 1.2 m above the sea floor.

The combined wave/current reference velocity, u_{cw}, is a function of the wave-induced bottom orbital velocity (Equation 5.4) and the apparent current velocity at the bottom, U_a, as given by:

$$u_{cw} = \left(U_b \cos \omega t + U_a \cos \phi_a, U_a \sin \phi_a\right) \tag{5.22}$$

where, U_b = wave-induced bottom velocity
U_a = apparent ambient current bottom velocity
ϕ_a = the angle between the apparent current and wave-induced current (Figure 5-38)
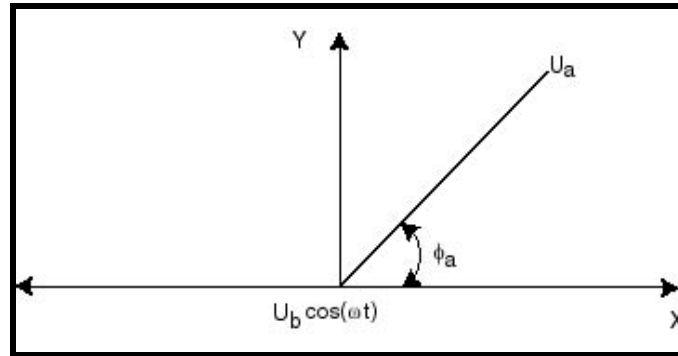

Figure 5-38. Illustration indicating the angle between the apparent bottom current and wave-induced bottom current (Grant and Madsen, 1979).

Because current observations were not measured at the bottom, they must be translated to the seafloor based on the application of a current profile through the bottom boundary layer. In order to determine the appropriate vertical current profile, the thickness of the bottom wave/current boundary layer (δ_w) must be determined and compared to the observed current location within the water column. A significant amount of work has been completed relative to the wave/current bottom boundary layer (Kajiura, 1964; Kajiura, 1968; Kamphuis, 1975; Knight, 1978; Bakker and van Doorn, 1978; Grant and Madsen, 1979; Trowbridge and Madsen, 1984). In addition, Trowbridge and Agrawal (1995) collected field data within the bottom boundary layer. Jonsson (1980) presents an equation for the thickness of the wave boundary layer in oscillatory rough turbulent flow, which is most common in nature, as:

$$\delta_w = \frac{2\kappa U_{*m}}{\omega} \tag{5.23}$$

κ = Von Karman's constant (0.4)

U_{*m} = the maximum current velocity at the seabed

$\omega = 2\pi/T$

If observed currents were measured outside of the bottom boundary layer ($z > \delta_w$), which is usually the case in field measurements, a logarithmic current profile is assumed, as:

$$U_c = \frac{U_{*c}}{\kappa} \ln\left(\frac{30z}{k_{bc}}\right) \tag{5.24}$$

where U_{*c} = the critical bottom velocity

z = height above the bed

U_c = the magnitude of the measured current

k_{bc} = the apparent bed roughness

The apparent bed roughness presented in Equation 5.24 is defined as:

$$k_{bc} = k_b\left(60\kappa \frac{U_{*m}}{k_b\omega}\right)^{\beta} \tag{5.25}$$

where k_b is the roughness coefficient, which is assumed to be equivalent to d_{50} of the local sediment, and $\beta = 1 - (U_{*c}/U_{*m})$.

In the present study, the observed current was measured outside of the wave boundary layer at all of the measurement stations; therefore, Equation 5.24 was applied to translate the observed current data to the seabed for each of the borrow site regions (Areas 1, 2, 3, and 4).

Having defined the ambient current velocity at the bottom, the bottom shear stress resulting from combined wave/current interaction can be determined. Maximum bottom shear stress, $\tau_{b,max}$, due to the combined current and wave action can be determined from

$$\tau_{b,max} = \rho U_{*m}^2 = \frac{1}{2}\rho f_{cw} U_b^2\left(1 + 2\varepsilon \cos\phi_a\right) \tag{5.26}$$

where $\varepsilon = (U_a/U_b)$.

The combined wave/current friction factor, f_{cw}, is provided by Madsen and Grant (1976) as:

$$f_{cw} = \frac{U_c f_c + U_b f_w}{U_c + U_b} \tag{5.27}$$

where f_c and f_w are friction factors corresponding to ambient current flow and wave-induced flow, respectively. The wave friction factor was presented by Jonsson (1966a) and is a function of the wave Reynolds number and ($U_b/k_b\omega$).

$$f_w = f_w\left(\frac{U_b^2}{\nu\omega}, \frac{U_b}{k_b\omega}\right) \tag{5.28}$$

The wave friction factor can be determined using Jonsson's wave friction factor diagram (Jonsson, 1966a). In a similar manner, the current friction factor can be determined from the standard Darcy-Weisbach approach:

$$f_c = \frac{1}{4}f\left(\frac{U_m 4h}{\nu}, \frac{d_{50}}{4h}\right) \tag{5.29}$$

The maximum bottom shear stress under the combined wave/current interaction is then used to calculate the Shields parameter (Ψ_{max}) from Equation 5.20, recast as:

$$\Psi_{max} = \frac{U_{*m}^2}{g(s-1)d_{50}}$$ (5.30)

Once the Shields parameter (Ψ_{MAX}) has been calculated at points of interest, the resulting values can be compared to a critical Shields parameter (Ψ_{crit}) to determine if sediment initiation occurs at each point of interest. The critical Shields parameter may be determined using a modified Shields diagram developed for sediment transport in the coastal environment (Madsen and Grant, 1976, 1977).

In addition, modifications have been made to the critical Shields parameter to account for sloped bed forms, such as the sideslopes of the dredged area. If sand grains are placed on a bed with a transverse slope or longitudinal slope, it is either easier or more difficult to initiate movement based on the direction of current flow (Figure 5-39). In the transverse case, the flow direction is perpendicular to the slope, while in the longitudinal case, the flow travels parallel to the slope. Therefore, sediment is initiated more easily on a downward slope than an upward slope and the critical Shields parameter decreases or increases according to bathymetry. Equations (5.31) and (5.32) take into account the transversely and longitudinally sloped bed forms, respectively, and provide an adjusted Ψ_{crit}:

$$\Psi_{crit} = \Psi_{\substack{critical\ for \\ a\ flat\ bed}} \cos\beta \sqrt{1 - \frac{\tan^2\beta}{\tan^2\phi_s}}$$ (5.31)

$$\Psi_{crit} = \Psi_{\substack{critical\ for \\ a\ flat\ bed}} \cos\gamma \left[1 - \frac{\tan\gamma}{\tan\phi_s}\right]$$ (5.32)

where β = transverse bed slope, γ = longitudinal bed slope, and ϕ_s = angle of repose.
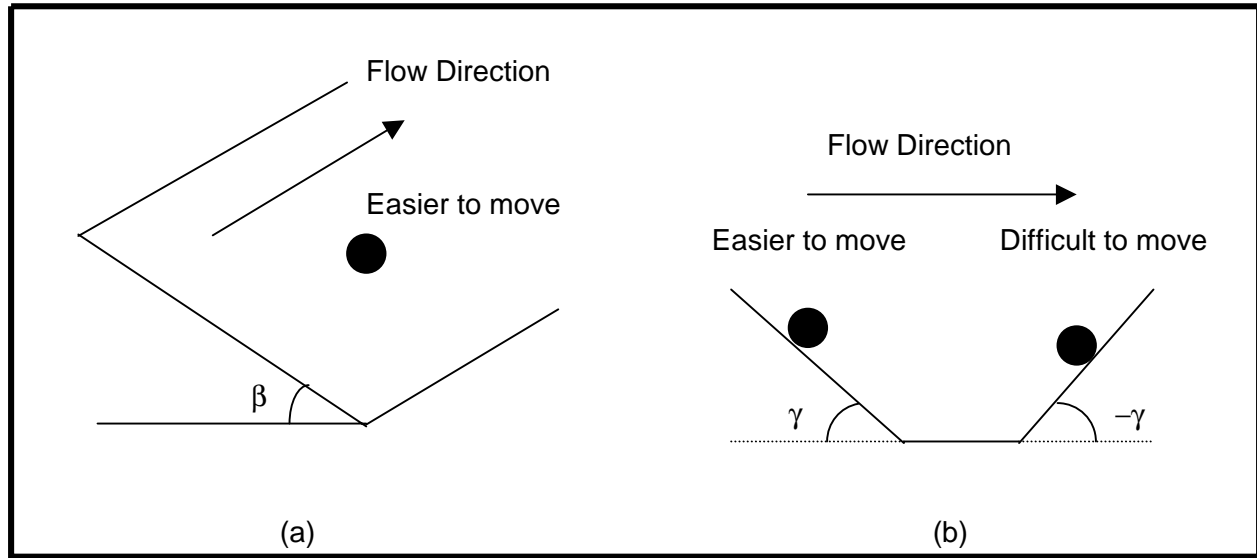

Figure 5-39. Illustration of a particle on a (a) transverse slope, and on a (b) longitudinal slope.

Finally, by comparing maximum and critical Shields parameters, sediment initiation can be determined at locations within and surrounding the offshore borrow areas. If Ψ_{max} exceeds Ψ_{crit}, then sediment will move. At each of the potential borrow locations, a subgrid encompassing the dredged region and surrounding area, was extracted from the reference modeling domain (Figures 5-40 and 5-41). At each point within the selected subgrid, the Shields parameter was determined and compared to the critical Shields parameter at that same grid point using wave modeling results for post-dredging scenario runs. In this manner, sediment initiation was determined at each point within the domain. The results of the sediment initiation analysis for each of the potential borrow sites (within Sand Resource Areas 1, 2, 3, and 4) are documented below.

5.2.1.2 Relative Magnitude and Direction of Transport

Sediment initiation provides valuable insight into sediment movement, but does not provide information as to how much sediment moves and in what direction is it traveling. Therefore, sediment transport rates and transport directions need to be calculated in and around the offshore borrow areas to assess overall sediment transport potential as well as provide insight into:

- approximate rates of sediment transport,
- estimates on borrow site infilling rates,
- seasonal fluctuations in sediment transport patterns, and
- impact of storm events on borrow site infilling.

This section presents the results of offshore sediment transport analyses at the potential borrow site locations following a large dredging episode. Sediment initiation and potential sediment transport rates were estimated in and around the dredged area.

Offshore sediment transport rates are based on analytical expressions developed by Madsen and Grant (1976). They involve:

1. determining the time-varying values of sediment transport in the northing (y) and easting (x) directions,
2. period-averaging these sediment transport component results, and
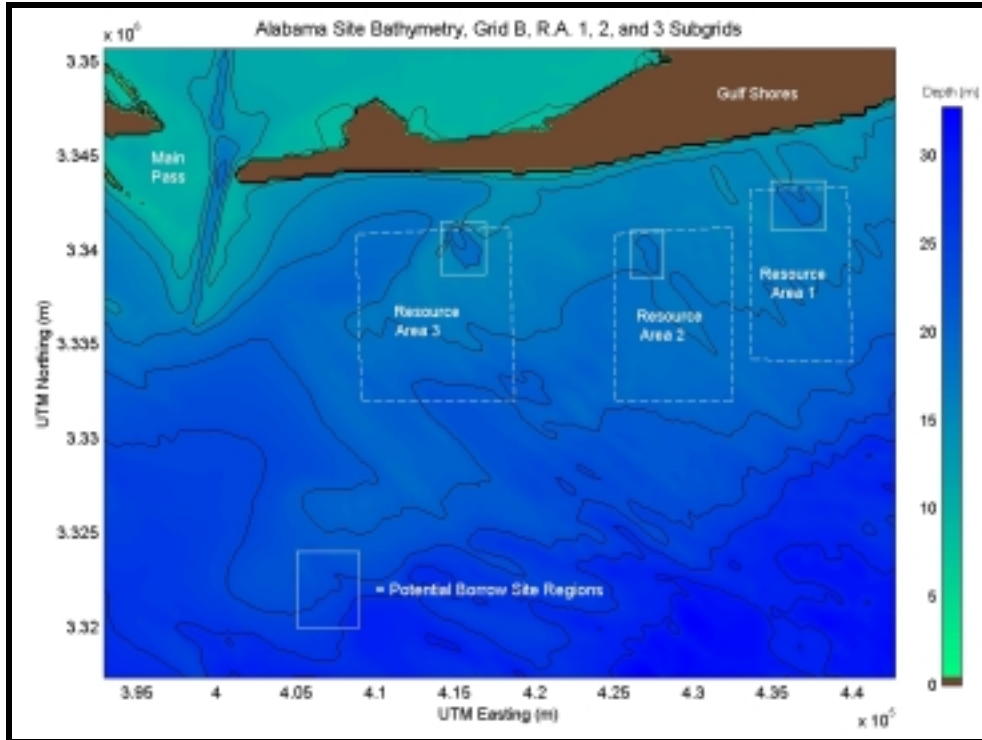3. calculating the net sediment transport magnitude and direction.

Figure 5-40. Location of the offshore subgrid regions within Sand Resource Areas 1, 2, and 3. These subgrids were used to determine potential sediment transport at the borrow areas following numerical dredging.
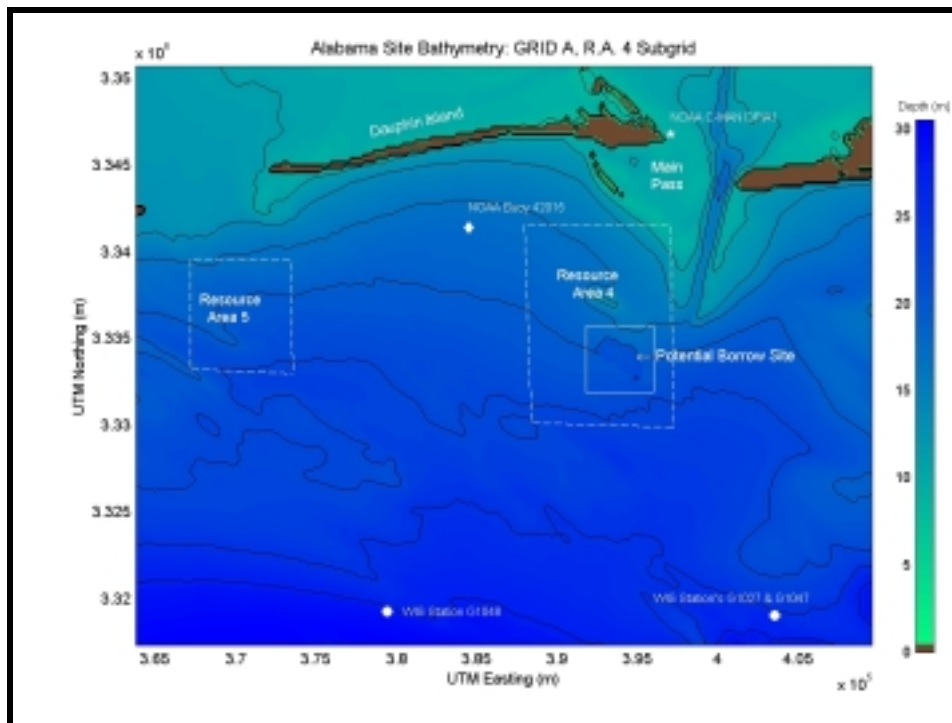

Figure 5-41. Location of the offshore subgrid region within Sand Resource Area 4. This subgrid was used to determine potential sediment transport at the borrow area following numerical dredging.

176

Determination of the instantaneous sediment transport rate is given by the following equations:

$$q(t)_{sediment, y} = 40 \, \omega_{fall} \, d_{50} \left[\frac{\frac{1}{2} f_{cw} \left(u(t)^2 + v(t)^2 \right)}{(s-1) \, g \, d_{50}} \right]^3 * \frac{v(t)}{\sqrt{u(t)^2 + v(t)^2}} \qquad (5.33)$$

$$q(t)_{sediment, x} = 40 \, \omega_{fall} \, d_{50} \left[\frac{\frac{1}{2} f_{cw} \left(u(t)^2 + v(t)^2 \right)}{(s-1) \, g \, d_{50}} \right]^3 * \frac{u(t)}{\sqrt{u(t)^2 + v(t)^2}} \qquad (5.34)$$

where $q(t)_{sediment, y}$ = sediment transport rate in northing direction
$q(t)_{sediment, x}$ = sediment transport rate in easting direction
$v(t)$ = time-dependent wave orbital bottom velocity and steady near bottom current in the northing direction
$u(t)$ = time-dependent wave orbital bottom velocity and steady near bottom current in the easting direction
ω_{fall} = sediment fall velocity

The above equations require information about sediment sizes at each of the four sand resource areas. Table 5-3 summarizes various sediment sizes that were needed to calculate sediment transport rates, as well as initiation. The values were obtained from grain size analyses performed on samples taken at each of the four sand resource areas.

Table 5-3. Sediment sizes at Sand Resource Areas 1 through 4.			
Resource Area	d_{10} (mm)	d_{50} (mm)	d_{90} (mm)
1	0.18	0.25	0.93
2	0.14	0.22	0.44
3	0.14	0.27	0.44
4	0.20	0.34	0.50

To determine the net sediment transport rate per wave cycle, sediment transport rates were period-averaged. The net period-averaged sediment transport rates in the northing $(\bar{q}(x,y))$ and easting $(\bar{q}(x,y))$ directions, respectively, are:

$$\bar{q}(x,y)_y = \frac{1}{T} \int_0^T q(t)_y \, dt \qquad (5.35)$$

$$\bar{q}(x,y)_x = \frac{1}{T} \int_0^T q(t)_x \, dt \qquad (5.36)$$

The northing and easting components can be combined by determining the sediment transport magnitude $(\bar{q}(x,y))$ defined as:

$$\bar{q}(x,y) = \sqrt{\left[\bar{q}(x,y)_y \right]^2 + \left[\bar{q}(x,y)_x \right]^2} \qquad (5.37)$$

177

In addition to magnitude, the net direction can be calculated based on the sediment transport components. Results of the analyses were used to visualize the rate of sediment movement and the direction of transport.

Four potential sand borrow sites were investigated to determine: 1) sediment transport rate estimates into and around the dredged areas, 2) indications of sediment supply areas, and 3) approximate infilling rates. Seasonal and extreme (50-yr storm) results are presented and discussed. In addition, a yearly average is interpolated from seasonal results, including the effects of a storm.

The results for Sand Resource Area 4 are discussed and presented within this section. The results for Sand Resource Areas 1, 2, and 3 are summarized in subsequent tables and Appendix C1. Figures 5-42 through 5-47 illustrate seasonal (winter, spring, summer, and fall) and extreme (50-yr storm) hydrodynamic and sediment transport results at the sand borrow site in Area 4. The figures include maximum wave-induced bottom velocities (upper left panel), steady near bottom currents (upper right panel), sediment initiation potential (lower left panel), and period-averaged sediment transport (lower right panel). For the upper left panel, solid lines indicate the depth contour of the numerically-dredged bathymetry, and the overlaid color map illustrates the magnitude of wave-induced bottom velocity (m/s). Red areas indicate regions of higher bottom velocity, while blue areas indicate lower velocities. Vectors indicate the direction and magnitude (length) of wave-induced bottom velocity at each grid point. The x-axis (easting) and the y-axis (northing) indicate the exact location on the subgrid within the sand resource area.

The upper right panel presents near bottom steady current results (m/s). Again, the bathymetry, including the dredged area, is illustrated with solid black lines while the color map shows the magnitude associated with the current. The vectors give the direction of the current in and around the borrow site.

Potential sediment initiation is presented in the lower left-hand panel. Bathymetry is shown as solid lines, while the color map illustrates the potential for sediment initiation. Red areas indicate regions of certain initiation while blue areas illustrate areas of minimal or no initiation.

Net sediment transport (m^3/day/cell width) and direction are shown in the lower right panel. This figure shows the direction of period-averaged transport (represented by vectors), and the color map provides a visual scale to determine the rate of transport per cell width (cell width = 200 m). Red areas indicate relatively high zones of transport, while blue areas indicate zones of no or minimal transport.

The winter season (Figures 5-42 and 5-43) is represented by two scenarios: a near bottom ambient current heading to the southeast, and a near bottom current heading to the northwest. During the winter season, historical current observations indicate that a near bottom current flows to the southeast 38% of the time and to the northwest 34% of the time (near Sand Resource Area 4). When coupled with the wave-induced bottom currents, it yields two different sediment transport patterns during the winter season. Ambient currents from the southeast initiate sediment north and northeast of Sand Resource Area 4 (Figure 5-42) in the shallower depths near the Mobile Outer Mound disposal site. The combined ambient and wave-induced current magnitude is high enough to move sediment in these areas, and the resulting sediment transport is in a southeasterly direction traversing across the dredged area. The pattern differs when compared to the northwest winter. Initiation occurs in similar areas, but transport is in the northwest direction and occurs throughout the northern section of the subgrid. Also, the sediment transport rates for the northwest winter scenario are slightly less than the southeast winter case.
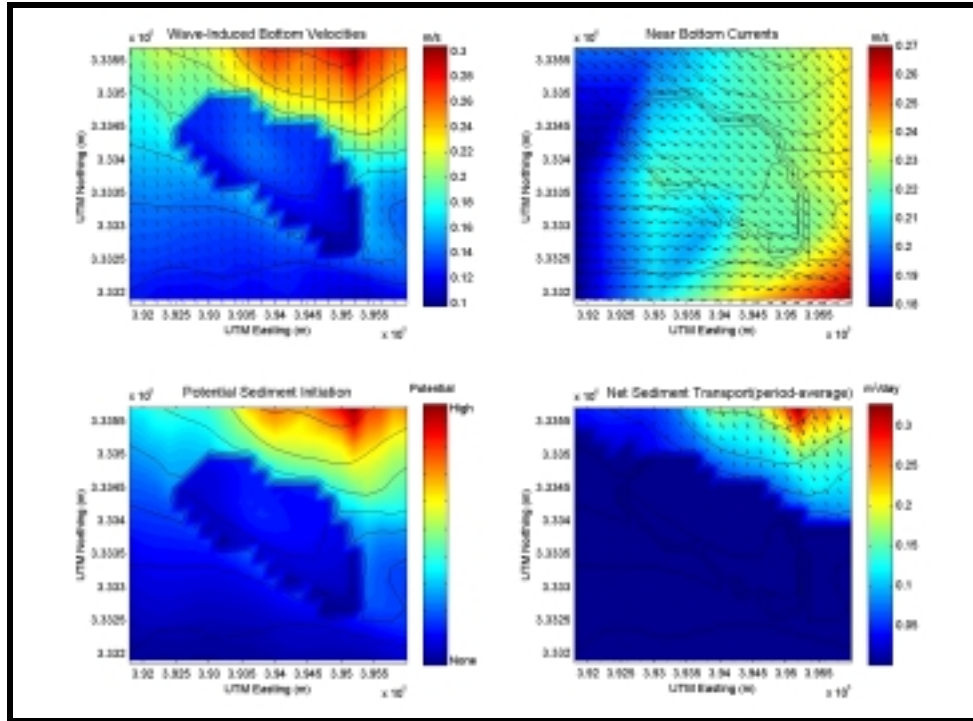
Figure 5-42. Southeast winter hydrodynamic and sediment transport results at Sand Resource Area 4. The solid black lines represent depth contours, and sediment transport results are based on 200-m cell widths.
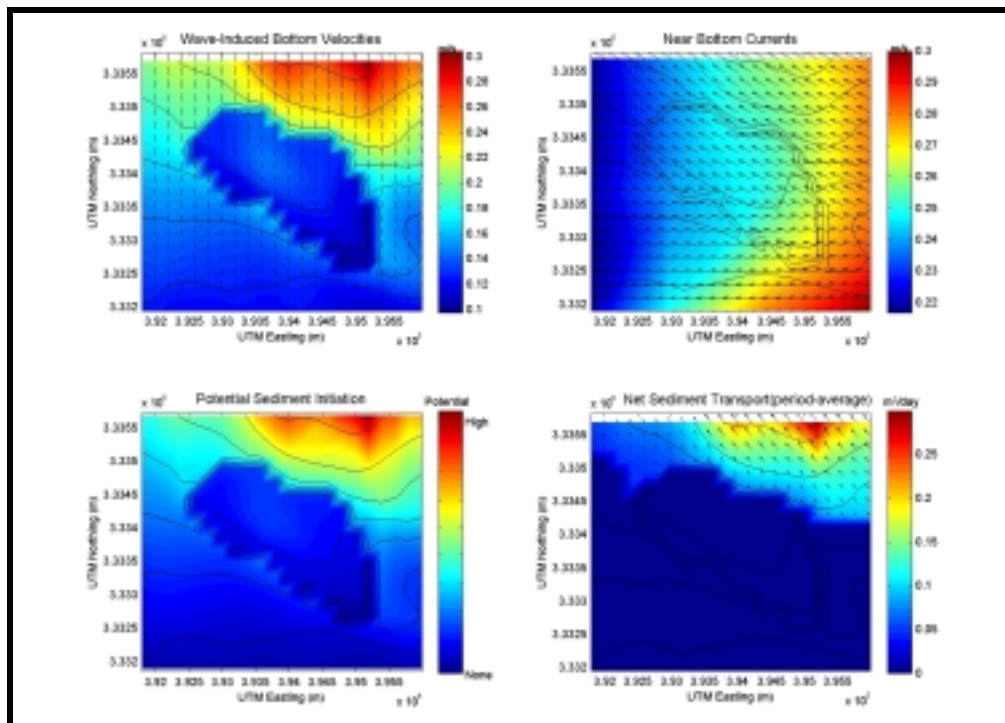

Figure 5-43. Northwest winter hydrodynamic and sediment transport results at Sand Resource Area 4. The solid black lines represent depth contours, and sediment transport results are based on 200-m cell widths.
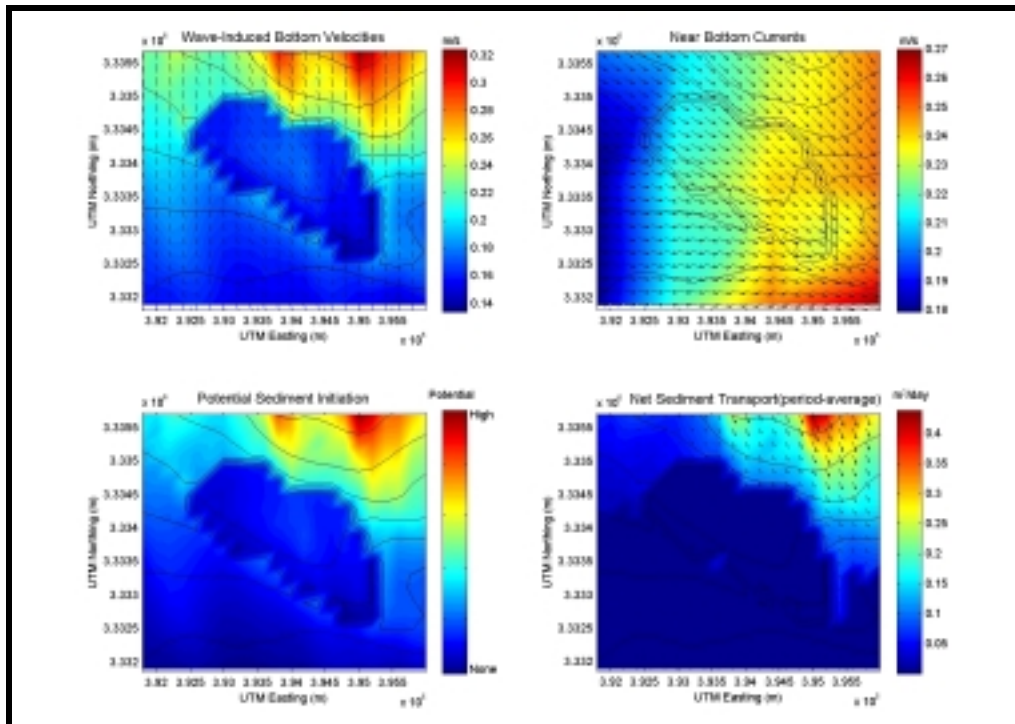
Figure 5-44. Spring hydrodynamic and sediment transport results at Sand Resource Area 4. The solid black lines represent depth contours, and sediment transport results are based on 200-m cell widths.
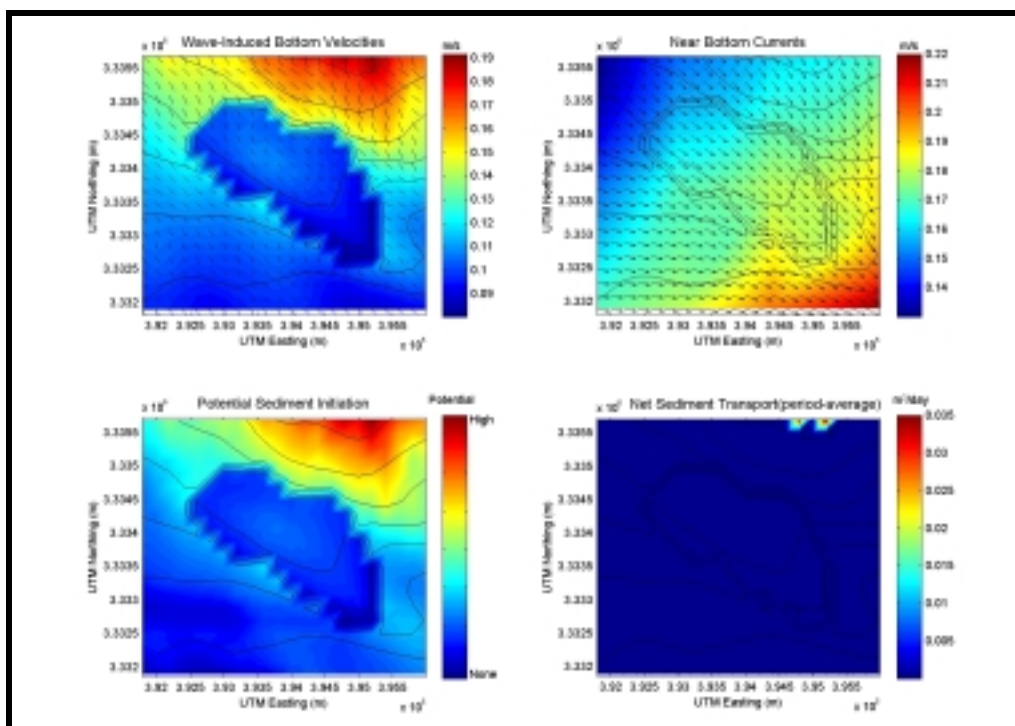

Figure 5-45. Summer hydrodynamic and sediment transport results at Sand Resource Area 4. Solid black lines represent depth contours, and sediment transport results are based on 200-m cell widths.
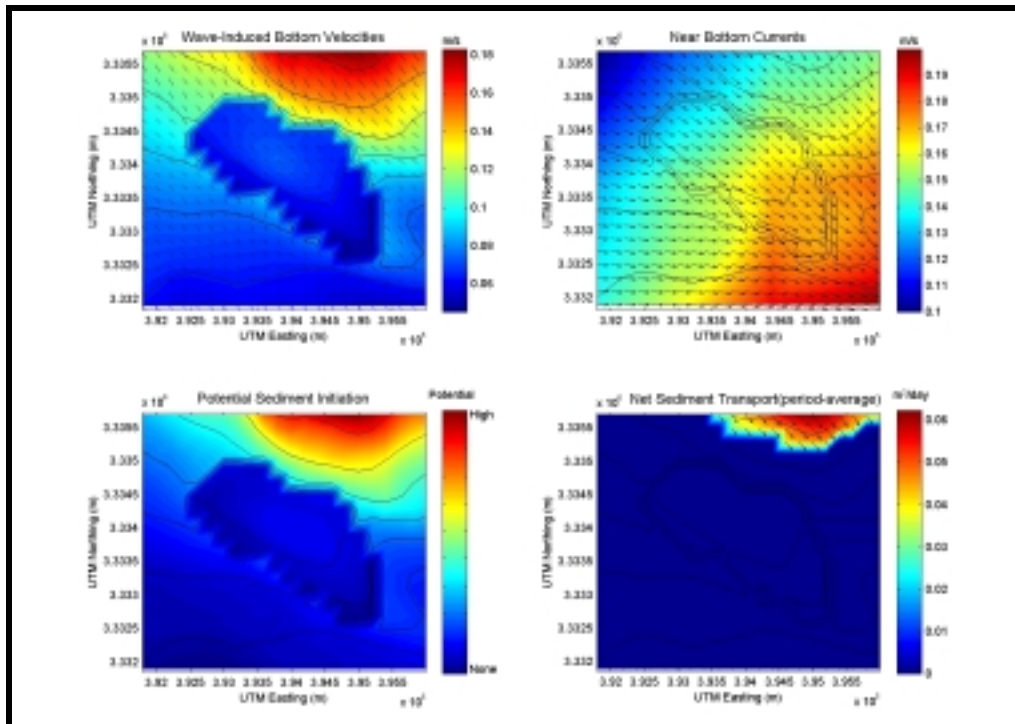
180

Figure 5-46. Fall hydrodynamic and sediment transport results at Sand Resource Area 4. Solid black lines represent depth contours, and sediment transport results are based on 200-m cell widths.
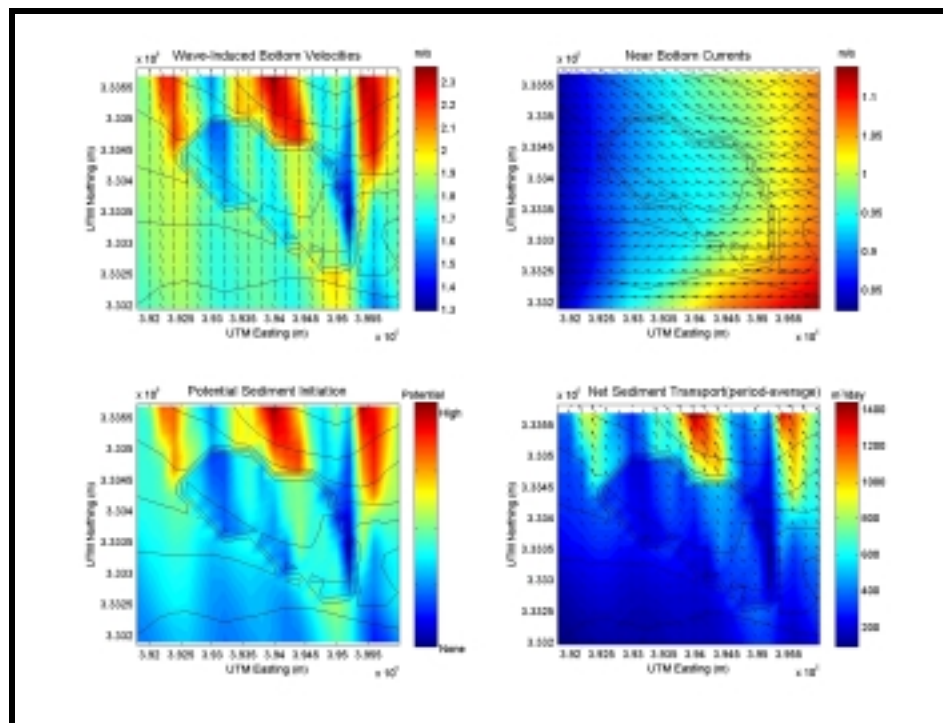

Figure 5-47. Extreme hydrodynamic and sediment transport results at Sand Resource Area 4. Solid black lines represent depth contours, and sediment transport results are based on 200-m cell widths.

During the spring (Figure 5-44), net sediment transport is similar to the southeast winter case. The spring season is comprised of relatively high wave-induced bottom currents and comparable near bottom currents. When combined, results initiate sediment over a larger area and increase the net transport rate slightly. Sediment is transported toward the east/southeast portion of the sand resource area.

Minimal transport occurs during the summer season. Summer wave heights are relatively small; therefore, the resulting wave-induced bottom velocities are small, allowing most of the sediment in and around the sand resource area to remain in place on the seafloor. Although a few cells indicate minimal transport (~ 0.035 m^3/day/cell width), it is practical to conclude that sediment transport does not occur at the potential borrow site in Resource Area 4 during typical summer conditions.

During the fall, sediment transport increases in limited areas adjacent to the borrow site; however, it is still of the same order as the summer season. Net sediment transport occurs in the northeast corner of the subgrid (in shallow depths near Mobile Outer Mound), and it is moved in a southeasterly direction.

Extreme (50-yr storm) conditions transport more sediment than any season. Concentrations of high initiation and transport (200 to 1400 m^3/day) are documented throughout the domain in the lower panels. Because maximum wave-induced orbital velocities and bottom currents are directed to the northwest, it follows that sediment transport occurs in the northwest direction.

All potential dredging scenarios for each of the selected borrow sites are summarized in the Table 5-4. The table includes information on the magnitude and direction of sediment transport into the sand resource areas, sand volume from the dredged area, and the approximate time to fill in the dredged site.

Table 5-4. Summary of seasonally-averaged sediment transport results using potential cumulative dredged sand volumes.				
Resource Area	Magnitude of Sediment Transport (m^3/day)	Direction of Sediment Transport (to)	Dredged Sediment Volume (x 10^6 m^3)	Time to Fill Dredged Area (yr)
1	117	NW	5.8	136
2	40	N	1.7	116
3	50	NE	4.7	257
4	37	SE	8.4	622

The analysis for infilling time assumes a constant rate of transport through each season and does not include the effects of modified bathymetry. For example, as the dredged region begins to fill, sediment transport dynamics and morphodynamics change. Therefore, sediment transport rates will fluctuate as the borrow site begins to fill. This dynamic, time-dependent process is not accounted for in the present analysis. In addition, our analysis does not include suspended sediment entering the local region. For example, a significant amount of fine material will enter the borrow site in Sand Resource Area 4 from Mobile Bay, significantly reducing the infilling time for that borrow area. Also, the two winter seasons are combined and weighted with other seasons to yield an average year. In spite of these assumptions, the analysis presented here does give an order of magnitude estimate of infilling times.

The magnitude of sediment transport can be interpreted as the rate during an average day. In addition, the third column presents the associated seasonally-averaged direction. The magnitudes and directions may fluctuate from day to day, but the magnitude and direction presented here are for an average year. Transport rates range from a minimum of 37 m^3/day to a high of

117 m^3/day. The fill time is determined by assuming a constant average infilling rate. The infilling times presented in Table 5-4 requires more than a century for all seasonal cases, likely due to the absence of storms in the analysis.

It is likely that dredged volumes will be smaller than the cumulative extraction scenarios utilized to investigate potential impacts. As such, Table 5-5 uses dredged sand volumes per beach replenishment event to compute the infilling time (see Section 7.1 for dredging volume details). These volumes were estimated based on quantities required to restore Alabama beaches after a major storm event. As expected, infilling times are drastically reduced. For Sand Resource Area 4, the time required to fill the sand borrow site is reduced by approximately a factor of 5.6.

Table 5-5. Summary of seasonally-averaged sediment transport results relative to sand dredging volumes per beach replenishment event.				
Resource Area	Magnitude of Sediment Transport (m^3/day)	Direction of Sediment Transport (to)	Dredged Sediment Volume (x 10^6 m^3)	Time to Fill Dredge Area (yr)
1	117	NW	.75	18
2	40	N	.75	51
3	50	NE	.75	41
4	37	SE	.50	111

5.2.2 Nearshore Sediment Transport Modeling

Nearshore sediment transport is a complex process that depends on waves, wind, and tidal action to affect coastal change. Although infrequent storm events represent the most significant erosion process, it is long-term variations in wave climate (combination of storm and normal conditions) that govern beach planform. Wave action constantly moves sand in the longshore direction due to wave-induced currents created by breaking waves. Waves incident from the east will tend to cause littoral drift to be directed to the west. Although wind and tides also govern sediment transport, the quantity of sand moved by these forcing mechanisms is minor when compared with wave-induced movement.

To adequately evaluate sediment transport along the Alabama coastline, a methodology incorporating wave orbital velocities needed to suspend sediment and mean wave-induced currents to advect sediment alongshore was employed. Grant (1943) first investigated the combined effect of orbital velocities and longshore currents on sediment transport processes. Over the past three decades, numerous researchers have developed methodologies for evaluating longshore transport rates based on calculations of the longshore current (e.g. Komar and Inman [1970], Thornton [1968], Grant and Madsen [1978], Sawaragi and Deguchi [1978], and Bodge [1986]). Due to the inherent complexities of surf zone dynamics caused by turbulent flow and energy dissipation, none of the methods provide perfect agreement with field data. However, utilizing reasonable assumptions, as well as a longshore sediment transport analysis technique based on sound scientific principles, a quantitative estimate of wave-induced transport can be determined.

To date, expressions for evaluating the distribution of longshore sediment transport across the surf zone have assumed that sediment is mobilized by (a) energy dissipation from breaking waves, (b) bottom shear stress induced by the peak horizontal orbital velocities alone, or (c) combined peak orbital velocities and the mean longshore current (Bodge, 1989). Mobilized sediment is then advected by the mean longshore current. Therefore, the distribution of longshore currents across the surf zone provides the driving force needed to predict local longshore transport

rates. Based on the review provided by Bodge (1989), most investigators have relied on the expression for longshore current on a planar beach developed by Longuet-Higgins (1970).

The existing models indicate that longshore sediment transport is largest between the breaker line and approximately midway across the surf zone, and that the transport rate tends to zero at the shoreline and outside the breaker line. Most models do not account for the often-significant longshore transport that occurs in the swash zone. Field data have indicated that significant sediment transport may occur in the swash zone; about 10% to 30% of the total transport occurs seaward of the breaker line, and greater transport is often associated with shallower depths such as bars. Overall, there is large variability in the shape of the transport distribution profile (Bodge, 1989). Although existing models have limitations, many of these models have been used successfully to evaluate the general characteristics of the longshore transport distribution.

5.2.2.1 Model Development

Stresses exerted by waves vary in the cross-shore direction, typically decreasing from the breaker line to the shoreline. However, this decrease may not occur in a uniform manner due to the presence of bars and troughs. The longshore current also has a characteristic profile, and because sand transport is the result of combined waves and currents, its distribution will be related to the distribution of waves and currents. Using data from field and laboratory experiments, Bodge and Dean (1987) tested five existing cross-shore distribution relationships. They provided a rating system for each relationship, ranging from fair to poor based on comparisons with measurements. Bodge and Dean (1987) also proposed a relationship for the cross-shore distribution of longshore sediment transport which assumed that sediment is mobilized in proportion to the local rate of wave energy dissipation per unit volume and transported alongshore by the mean current. In equation form, this expression is

$$q_x(y) = k_q \frac{1}{d} \frac{\partial}{\partial x} (EC_g) V \qquad (5.38)$$

where $q_x(y)$ is the local longshore transport per unit width offshore, y represents the cross-shore coordinate, k_q is a dimensional normalizing constant, d is the local water depth in the surf zone (including wave-induced setup), E represents the local wave energy density, C_g is the local wave group celerity, and V_t is the local mean longshore current speed. The above expression can be expanded by assuming shallow water wave conditions, small angles of wave incidence, and a nonlinear value for the wave group celerity ($C_g = (g(H+d))^{1/2}$) as:

$$q_x(y) = k_q \frac{1}{8} \rho g \frac{H}{\sqrt{H+d}} \left[2\frac{dH}{dy} + \frac{H}{2(H+d)} \frac{d}{dy}(H+d) \right] V \qquad (5.39)$$

in which H is the local wave height in the surf zone. This shallow water equation represents conditions landward of the breakpoint. Seaward of the breakpoint, transport is assumed to be negligible since no energy dissipation occurs. This simplification could underestimate the transport rate by between 10% and 30%, since field measurements have indicated that this amount of transport occurs seaward of the breaker line. However, the REF/DIF S wave model employed in this study used a spectral wave breaking model. By employing this type of wave breaking model, no definitive breakpoint exists and a small amount of transport will occur in the region where some of the high period spectral components break. Therefore, sediment transport occurs seaward of the standard definition of the breakpoint. Energy dissipation, as well as the associated transport, within this offshore region was assumed to characterize transport seaward of the breakpoint. The distribution of $q_x(y)$ was integrated across the nearshore zone to compute longshore transport rates for each cross-shore profile.

5.2.2.2 Sediment Transport Along the Alabama Coast

The REF/DIF S wave and wave-induced current models provided needed information for the littoral drift evaluation. Longshore currents were derived from the wave-induced current model, and wave parameters (wave height and water depth) were derived from wave modeling results. Because the purpose of the sediment transport modeling task was to determine impacts of offshore sand mining on the nearshore region, a sensitivity analysis of the empirical constants utilized in the transport equation was not required. Instead, the k_q value was determined from the bathymetric change analysis. Based on maximum annual transport rates of between 100,000 and 200,000 m^3/yr, the k_q value was set and remained constant for all model runs. By comparing existing sediment transport potential rates to variations in the rates resulting from the various dredging scenarios, the relative impact of dredging on nearshore transport processes were quantitatively evaluated.

Similar to the wave-induced current model, the longshore sediment transport model was run for the Dauphin Island and Morgan Peninsula wave modeling grids, for each spectral wave condition (total of five) under existing conditions and post-dredging scenarios. This required a total of 20 model runs. Results from all model runs are included in Appendix C2. As an example, the results of one run (the existing conditions at Morgan Peninsula for spring wave conditions) are described in more detail below. This example provides an overview of typical wave-induced sediment transport predictions associated with the modeling effort.

The S_{xy} radiation stress component provided the primary driving force for wave-induced currents and longshore sediment transport. Radiation stress values were generated from REF/DIF S modeling; therefore, results of the wave-induced current and longshore sediment transport models was dependent on the numerical evaluation of the nearshore wave climate. Figure 5-48 illustrates the longshore and cross-shore distribution of S_{xy}, indicating regions of wave energy focus. As expected, areas of higher S_{xy} values have higher longshore sediment transport rates. Because all sediment transport is directed east-to-west, the general decrease in sediment transport rate from UTM Easting coordinate 415,000 m to approximately 403,000 m would indicate a tendency toward accretion. The opposite is also true, where the increase in sediment transport rate from UTM Easting coordinate 423,000 m to approximately 415,000 m would be indicative of a shoreline segment experiencing erosion.

Morgan Peninsula and Dauphin Island sediment transport modeling results indicated a large variation in transport magnitude; however, the overall tendency along both shorelines was an east-to-west littoral drift. Over the entire study area, the only exception to this transport trend was the region at the eastern terminus of Dauphin Island. In this region, wave protection afforded by Pelican Island and the numerous offshore shoals caused a reversal in net transport direction. However, the magnitude of this west-to-east transport is low due to wave energy dissipation on the shoal system.

For the Morgan Peninsula, sediment transport rates generally increased from west-to-east for seasonal model runs. Due to specific regions of wave focusing associated with seasonal wave characteristics, some areas of increased sediment transport potential existed along the shoreline. For example, sediment transport calculations for the spring and winter season indicated relatively high transport rates at UTM Easting coordinate 415,000 m (Figure 5-48). Along the Dauphin Island shoreline, greater seasonal variability in transport rates was evident (Appendix C2). Again, results from the spring and winter model runs indicated similar results, due to similar wave spectra characteristics. For both seasons, the transport rate generally increased from east-to-west. The mild wave climate in the summer season indicated sediment transport potential at a lower magnitude than other seasons. In addition, a reversal in transport direction was predicted at UTM Easting coordinate 382,000 m (Figure 5-49). The broad spectral spreading characteristics of the fall season indicated highest transport rates near the middle portion of Dauphin Island (between
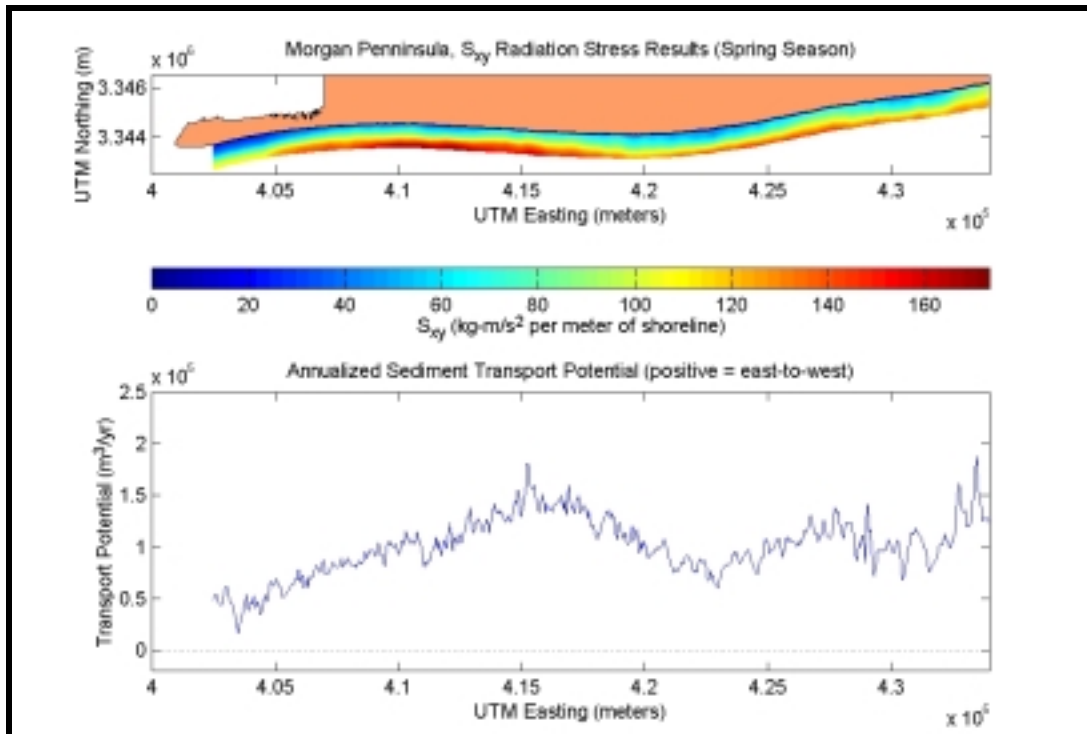
Figure 5-48. S_{xy} radiation stress values and annualized sediment transport potential for the spring season at Morgan Peninsula.
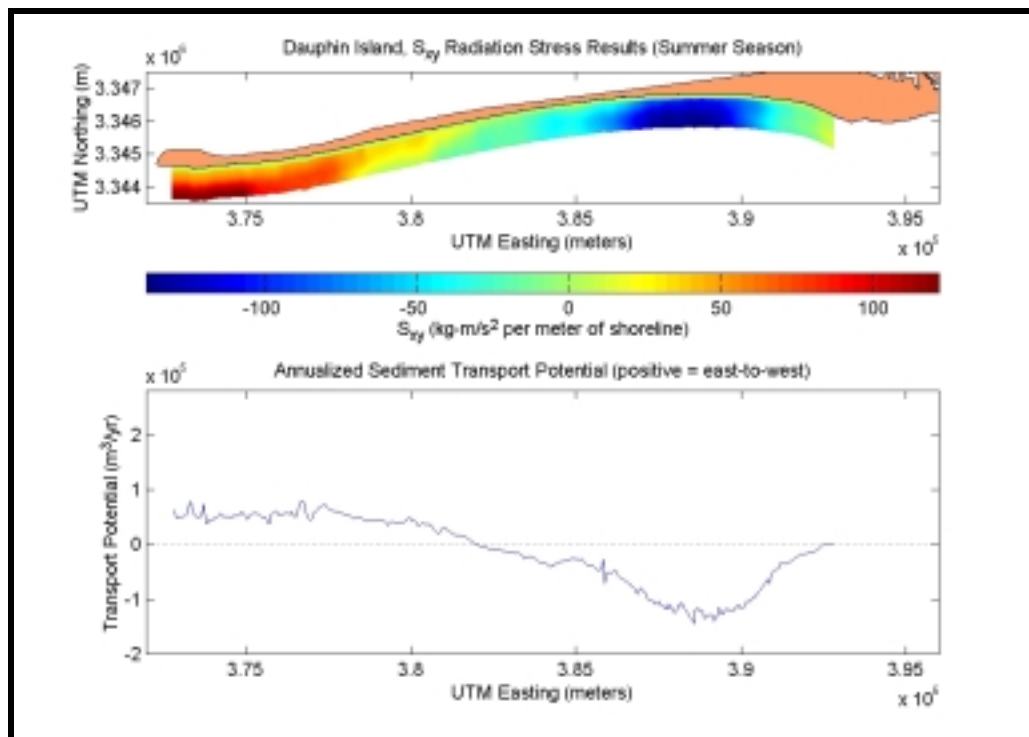

Figure 5-49. S_{xy} radiation stress and annualized sediment transport potential for existing conditions at Dauphin Island during the Summer season.

UTM Easting coordinates 380,000 and 385,000 m. Because transport rates predicted for the spring and winter seasons were significantly greater than the other two seasons, these seasons tended to dominate the long-term sediment transport trends along Dauphin Island.

Similar to the wave modeling results, the sediment transport rates calculated for the 50-year event illustrated significant longshore variability. Along Dauphin Island, the relative magnitude of transport was similar to the seasonal trend, where the transport rate was lowest adjacent to the Mobile Bay entrance and generally increased in magnitude from east-to-west. Along Morgan Peninsula, the transport rate was highest near the eastern end of the modeled region.

In addition to providing net sediment transport rates, the transport model provided the cross-shore distribution of longshore sediment transport across the surf zone. Figure 5-50 illustrates this cross-shore distribution in relation to the cross-shore distribution of the mean longshore current at three selected transects. Based on the results of the sediment transport model, peak current velocities occur landward of the peak sediment transport. Since most wave models predict rapid energy dissipation at the breaker line, and the sediment transport equation used strongly depends on the wave energy dissipation rate, the highest sediment transport rate can be expected relatively close to the break point. Field and laboratory data collected by Bodge and Dean (1987) indicate that peak transport rates often occur near the breakpoint. The current distribution predicted by the longshore current model also corresponds to other model approaches, where the maximum currents occur in the seaward half of the surf zone.

5.2.2.3 Nearshore Sediment Transport Versus Historical Shoreline Change

As a simplistic measure of the longshore sediment transport model's applicability to the Alabama shoreline, an attempt was made to compare accretion/erosion potential predicted by the model to shoreline change results. The accretion/erosion potential was determined through calculation of sediment transport change normalized to the maximum computed change. In this manner, the relative magnitude of erosion and accretion could be evaluated for the entire shoreline segment. Because the calculation of accretion/erosion potential was dependent on the slope of the net sediment transport curve, smoothing of this curve was performed to determine general transport trends. Shoreline change for the entire time period (1847/67 to 1978/81) was plotted for comparison purposes. The results of this analysis are shown in Figures 5-51 and 5-52 for Morgan Peninsula and Dauphin Island, respectively.

Figure 5-51 illustrates large variability in accretion/erosion trends predicted by the sediment transport model, as well as the variability of observed shoreline change. Due to this high variability, it is difficult to determine obvious trends for either the normalized transport change or the observed shoreline change. Erosion indicated by shoreline change results between UTM Easting coordinates 418,000 and 423,000 m, as well as between 427,000 and 431,000 m, was predicted by the sediment transport model. However, some other regions of observed shoreline change did not correspond to model predictions. For example, the model predicted a general tendency toward shoreline accretion between UTM Easting coordinates 404,000 and 415,000 m (immediately east of the Mobile Bay entrance). However, shoreline change indicated that the long-term trend of accretion only extended to approximately UTM Easting coordinate 408,000 m. The relatively stable region between 415,000 and 427,000 m (low annual shoreline change rates) was adequately predicted by the modeled sediment transport trends in this region.

Although many of the trends indicated by the observed shoreline change and the computed accretion/erosion potential were predicted well, several shoreline reaches indicated opposite trends, where the observed and computed accretion/erosion contradicted each other. Direct comparisons of measured shoreline change and computed sediment transport have several sources of potential error and variability. First, the modeled change in longshore transport represents sediment moving
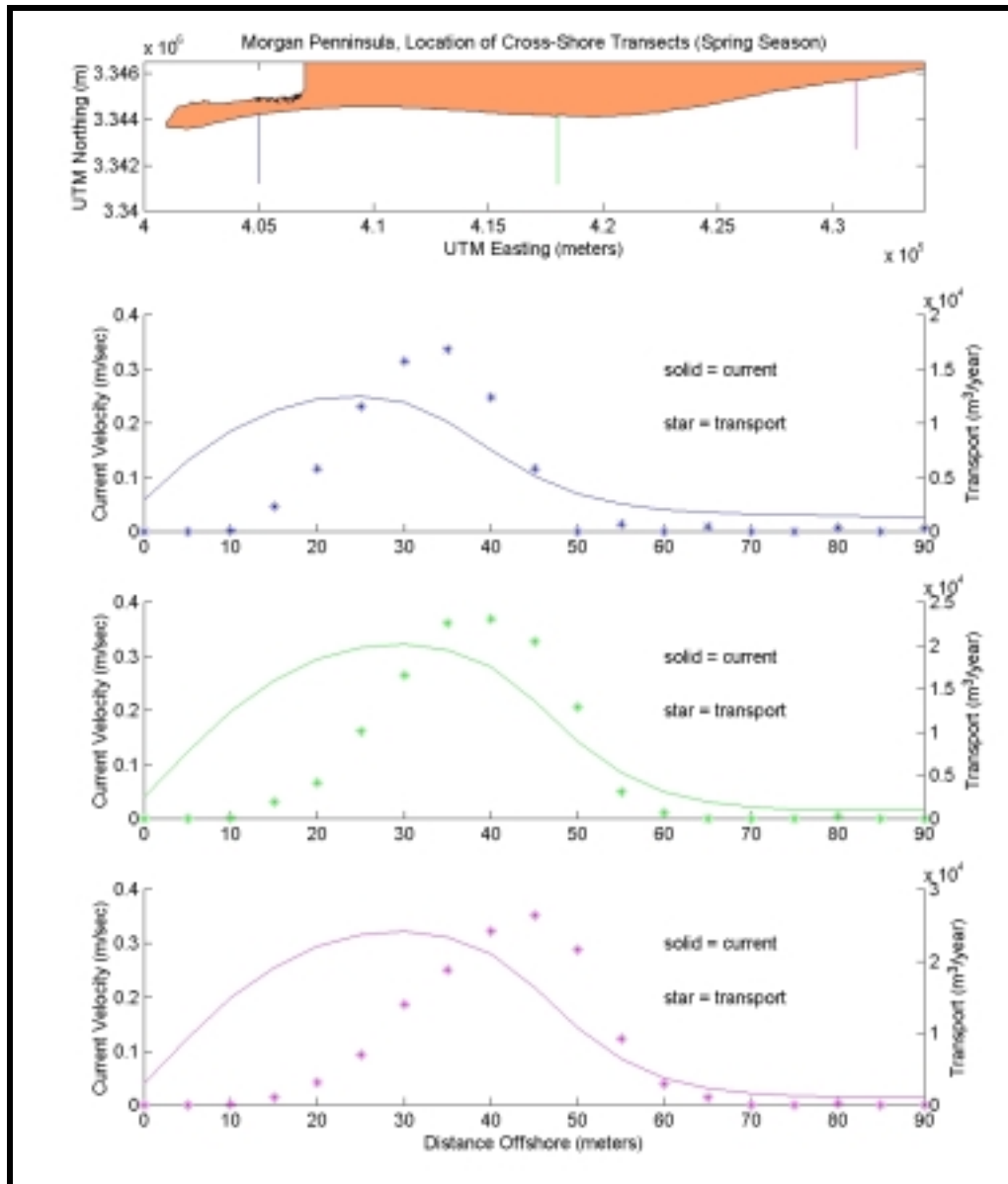
Figure 5-50. Cross-shore distribution of longshore current and sediment transport for three selected transects (spring season at Morgan Peninsula).
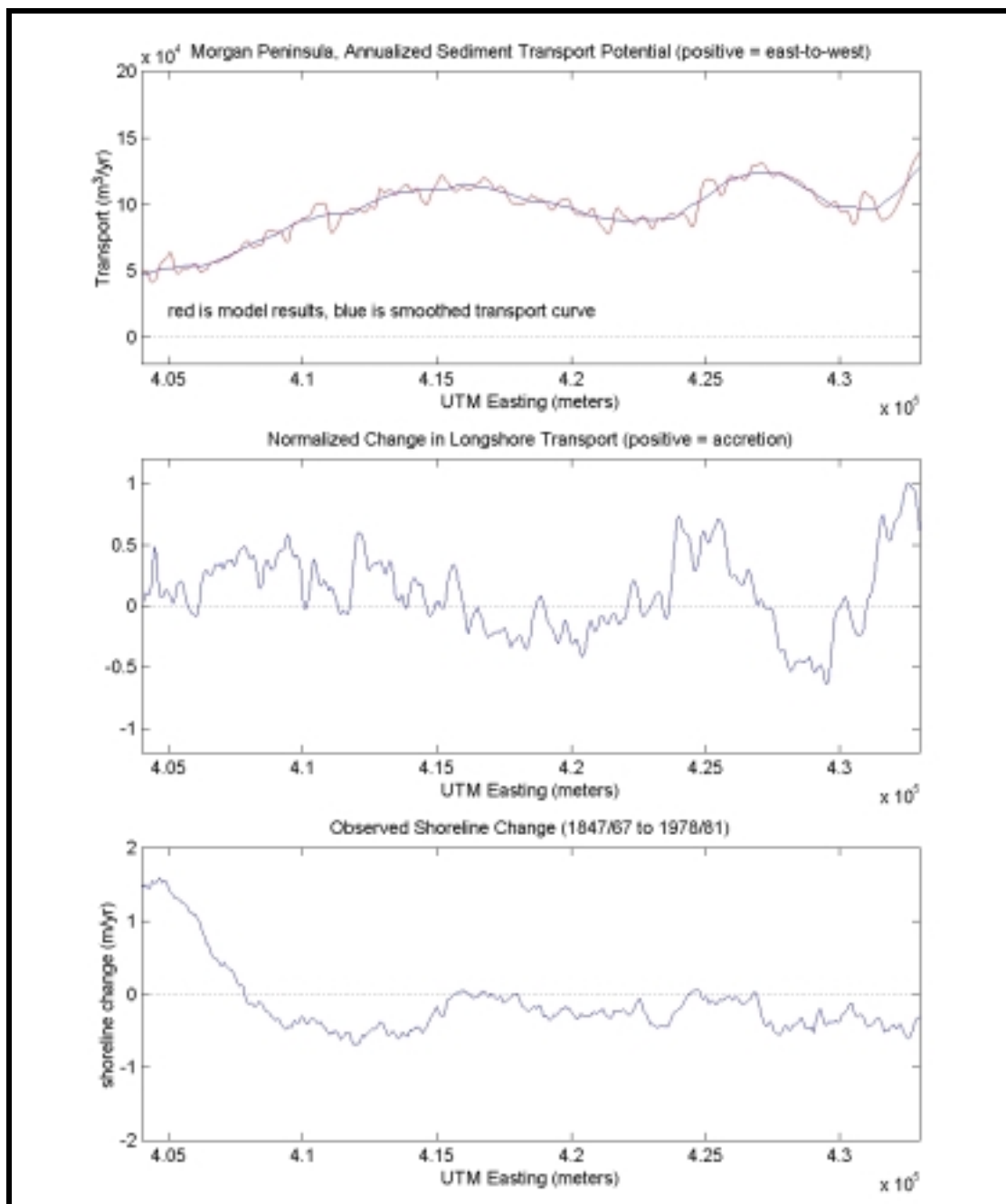
Figure 5-51. Annual longshore sediment transport potential, normalized change in longshore transport (modeled accretion/erosion potential), and observed shoreline change between 1847/67 and 1978/81 for the Morgan Peninsula.
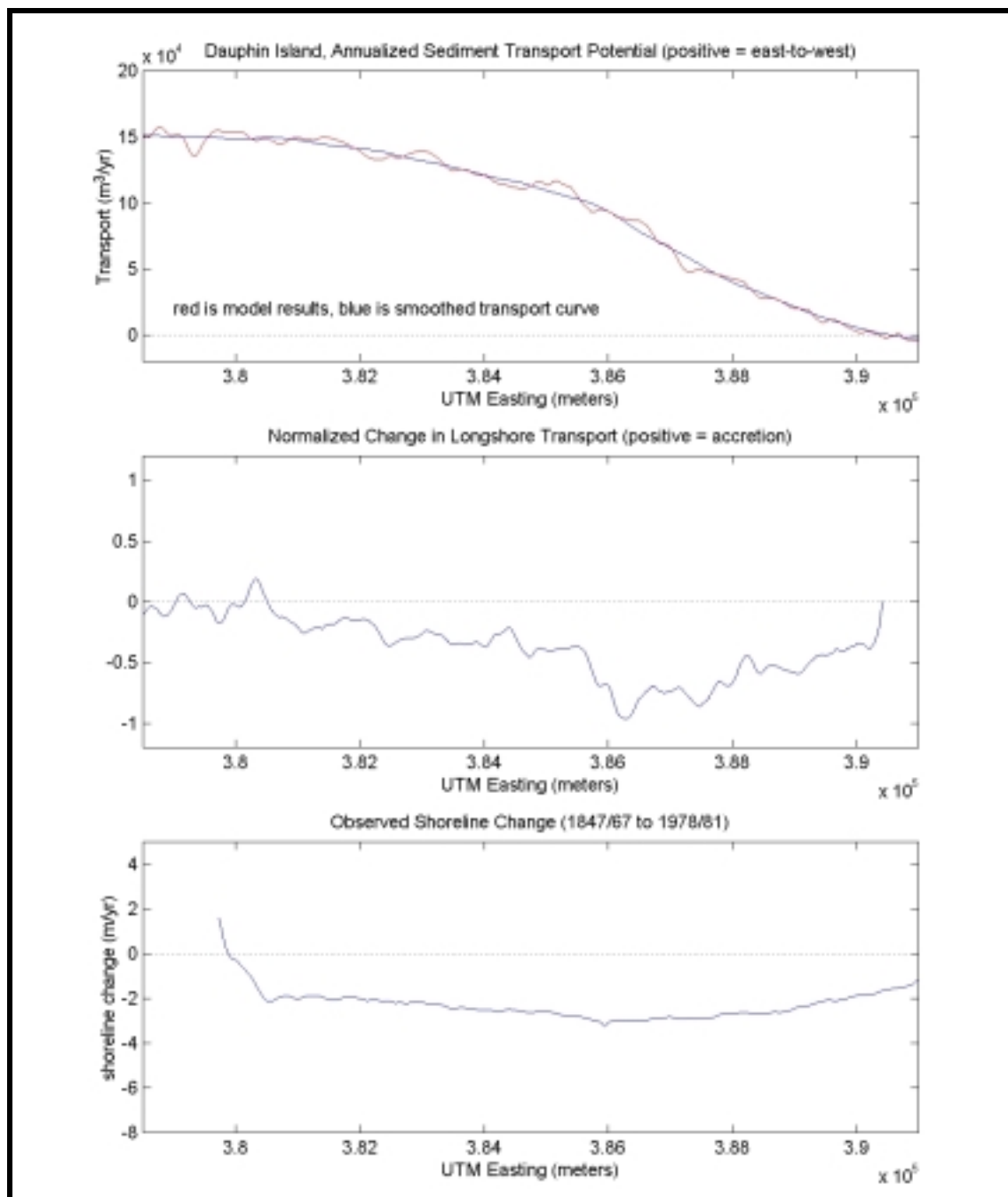
Figure 5-52. Annual longshore sediment transport potential, normalized change in longshore transport (modeled accretion/erosion potential), and observed shoreline change between 1847/67 and 1978/81 for Dauphin Island.

throughout the surf zone and shoreline change merely indicates migration of a single line. For example, the bathymetric change analysis indicated accretion in the nearshore area (surf zone) at the western end of the Morgan Peninsula. Therefore, observations of bathymetric change are in direct conflict with shoreline change results, indicating that shoreline change alone may not be a valid indicator of coastal change.

Sediment transport modeling also assumes an infinite sediment source. If erosion potential is high along a certain stretch of shoreline, the model assumes that this volume is available for transport. However, natural beaches typically are in a state of constant adjustment toward equilibrium based on current environmental conditions (waves, tides, winds, etc.). Therefore, the shoreline may not be able to provide the sand volume required by wave conditions, a sediment deficit is created downdrift, and the beach does not behave exactly as the model predicts. Typically, sediment transport models are appropriate for use on sandy coasts like Dauphin Island and the Morgan Peninsula because they can accurately predict long-term trends in these areas.

Figure 5-52 illustrates accretion/erosion potential and observed shoreline change at Dauphin Island. Due to wave sheltering provided by Pelican Island and the numerous offshore shoals, there is a marked decrease in transport rates between the central portion of the Island and its eastern terminus. Because net direction of transport is from east-to-west, the increase in modeled transport rates from the east end of Dauphin Island to the center of the Island creates an erosional trend. This result compares well with observed shoreline change between 1847/67 and 1978/81, where the peak observed erosion, as well as the peak computed erosion, occur at approximately the same location (UTM Easting coordinate 386,000 m). Along the western portion of the Island, the modeled longshore transport rate decreases, indicating a tendency toward lower erosion rates and/or a stable shoreline. This result also agrees with the observed shoreline change, where the high annual shoreline erosion rate (approximately 2 m per year) becomes negligible at UTM Easting coordinate 380,000 m.

Although similar potential errors exist for comparing observed shoreline change with computed accretion/erosion tendency, the results for Dauphin Island compare favorably for the entire shoreline. The larger magnitude of observed shoreline change for Dauphin Island made general trends more obvious than trends observed along the Morgan Peninsula. In addition, bathymetric contours offshore of Dauphin Island were predominantly shore parallel, unlike the shore-oblique sand ridges offshore of Morgan Peninsula. This more simplistic bathymetry facilitated more accurate modeling of the nearshore wave field; therefore, prediction of erosion/accretion trends also was more accurate.